UNIVERSITÀ DEGLI STUDI DI PARMA
DIPARTIMENTO DI INGEGNERIA DELL'INFORMAZIONE

Dottorato di Ricerca in Tecnologie dell'Informazione
XX Ciclo

Massimiliano Salsi

ON SEMICONDUCTOR OPTICAL AMPLIFIERS AND OPTICAL COHERENT DETECTION

Dissertazione presentata per il conseguimento
del titolo di Dottore di Ricerca

Gennaio 2008

Alla mia famiglia

Contents

Foreword

Optical telecommunication systems are the backbone of the information technology evolution we live everyday. When this work began video contents on the internet where only part of prototype transmissions while today they represent a normal part of everyday life web surfing. Heavy contents demands for high bandwith and this is the driver of the telecommunication industry, that shares with the computer industry the exponential grow rate. This means that engineers and researchers should be always working in order to supply the market with more powerfull devices. Sometimes it is possible to increase the spectral efficiency through an upgrade but sometimes there are insurmountable bottlenecks. Most of the times there are no really new inventions, there are just new solutions born by an innovative usage of available technologies. This is the reason why we believed in a technology that seemed abandoned by the present optical industry, which are the Semiconductor Optical Amplifiers (SOA). It is true that these devices are not the best optical amplifiers and cannot compete with the Erbium doped ones. But there are aspects of the SOA technology that are proper of these devices only: integrability, small footprint and the possibility to write optical structures like Bragg gratings directly in the waveguide. The second technology considered in this work is the optical coherent detection, which is another "old" technology investigated again after the evolution of digital signal processors (DSP). More DSP power allows for a phase unlocked local oscillator so that it is now possible to get over the problems that 20 years ago made the optical coherent detector unprofitable.

In Chapter 1 the SOAs are studied by numerical and experimental investigation. A simple and fast single state variable model is proposed and experimentally validated. The model is then improved in order to take into account nonlinear effects.

In Chapter 2 a more complex SOA structure, the one of Linear Optical

Amplifiers (LOA), is investigated. An experimental comparison shows that LOA do not bring real advantages in a 10 Gbit/s transmission system.

In Chapter 3 the optical coherent detector aided by digital signal processing is introduced and an experimental investigation shows the fascinating capabilities of this technique. All the linear impairments that affect today's optical systems can be easily compensated.

In Chapter 4 the tolerance to nonlinear effects of the optical coherent detector is commented after an experimental investigation and some numerical simulations. This is an innovative research that evaluates the profitability of this technology as a possible upgrade for actual ultra-long haul optical transmission systems.

Acknowledgements

I would like to thank my advisor, Prof. Alberto Bononi, for his valuable guidance and for having always been an example to follow. Most of the experimental works of this thesis have been done in the laboratories of Alcatel-Lucent, in Nozay (France). I would like to thank the team of Dr. Sébastien Bigo for the support and the precious collaboration. In particular, Dr. Charlet, Dr. Renaudier and, Dr. Bertran Pardo have been generous and stimulating colleagues. The support they gave to me during my period abroad has been priceless.

January 18, 2008

Chapter 1

Semiconductor Optical Amplifiers

Semiconductor optical amplifiers (SOA) are becoming key devices for future optical networks. A wealth of applications and functions use SOAs. For example, optical switching and wavelength conversion can be accomplished using cross-gain modulation (XGM), four-wave mixing (FWM), or cross-phase modulation (XPM) [1, 2]. Signal reshaping and noise cleaning of on-off keying (OOK) signals is also feasible using saturated SOAs [3], with particularly effective application in spectrum sliced wavelength division multiplexing (WDM) [4] and incoherent optical code division multiple access [5]. In this chapter we are interested in analysing the response of SOAs to optical signals whether they belong to a WDM link or to an optical packet based metropolitan area network. There are specific cases where ultrafast intraband phenomena such as carrier heating (CH) and spectral hole burning (SHB) (see e.g. [6, 7]) can be neglected, and only carrier induced gain dynamics need to be considered, as was done in several SOA models developed in the past. But in this chapter we will present a model that is able to take into account these effects without loosing in simplicity, which is its strong point.

Past models can be divided into two broad categories: 1) space-resolved, numerically intensive models, which take into account facet reflectivity as well as forward and backward propagating signals and amplified spontaneous emission (ASE), and offer good fit to experimental data [8, 9]; and 2) analytical, simplified models with coarser fit to experimental data, but developed to facilitate conceptual understanding and performance analysis [10–12]. For the purpose of carrying out extensive Monte-Carlo simulations for statistical signal analysis and bit-error rate (BER) estimation, the accurate space-resolved models are ruled out because of their prohibitively long simulation times. However, a simplified model with more satisfactory fit to experimental results would be highly desirable. Most simplified models can be derived from the work of Agrawal *et al.* [11]. Here, under suitable assumptions, the authors managed to reduce the coupled propagation and rate equations into a single ordinary differential equation (ODE) for the integrated gain (eq. (3.4) in [11]). The simplicity of the solution is due to the fact that waveguide scattering losses and ASE were neglected. ASE has an important effect on the spatial distribution of the carrier density and saturation, and it may significantly affect the SOA steady-state and dynamic response [13,14]. Scattering losses also have an impact on the dynamic response of the SOA [2]. Moreover, Agrawal's model was originally cast for single wavelength channel amplification, although it can be extended to multi-wavelength operation by assuming that the channels are spaced apart far enough to neglect four wave mixing beating in the co-propagating case [2]. Saleh [15] arrived independently at the same model as Agrawal (eq. (4a) in [15] coincides with eq. (3.4) in [11]), and then introduced further simplifying approximations to get to a very simple block diagram of the single-channel SOA, which was exploited for a mathematically elegant stochastic performance analysis of single-channel saturated SOAs [16]. The loss of accuracy due to Saleh's extra approximations with respect to Agrawal's model was quantified in [17]. Saleh's model was later extended to cope with injection current modulation, scattering losses and ASE [12]. Also Agrawal's model was extended to include ASE [18]. In both [12] and [18] ASE was added phenomenologically at the output of the SOA, and did not influence the gain dynamics, thereby limiting the application to very small saturation levels.

In this chapter a novel state-variable SOA dynamic model, which represents the most important contribution of this work, will be presented. This model is an extension of Agrawal's model as provided in [2], with the inclusion of approximations for scattering loss and ASE to better fit the experimental results. In such a model, the SOA dynamics are reduced to the solution of a single ODE for the single state variable of the system, proportional to the integrated carrier density [2], which for WDM operation is a more appropriate variable than the integrated gain used in [11]. Once the state variable dynamics are found, the dynamics of all output WDM channels are also obtained. The state variable is called here the *reservoir*, since it plays the same role as the reservoir of excited erbium ions in an erbium-doped fibre amplifier (EDFA) [19], [20].

The first model presented treats the intensity of the electrical field, but the field phase can be indirectly obtained since it is a deterministic function of the reservoir [11]. Considering the intraband effects as in [7], we will extend the reservoir model in order to make it manage electrical field and all the fast intraband nonlinear effects responsible for four-wave mixing. As already mentioned, the basic reservoir model requires the (co-propagating) WDM channels to have minimum channel spacing in excess of a few tens of GHz, in order to neglect the carrier-induced FWM fields generated in the SOA. This should not be a problem for channels allocated on the ITU grid with 50 GHz spacing or more. Nevertheless, with the possibility to include ultrafast effects like carrier heating (CH) and spectral hole burning (SHB) the numerical results will take into account all the possible FWM sources and will give better results at any possible channel spacing. It is worth mentioning that state-variable amplifier models are very important simulation tools that enable the reliable power propagation of WDM signals in optical networks with complex topologies, and therefore the present reservoir SOA model provides a new entry, besides the already known models for EDFAs [19], [21] and for Raman amplifiers [22].

The chapter is organised as follows.

In section 1.1 the Connelly [9] model for SOA is introduced, and the most important parameters in SOA modeling will be discussed. The Connelly model was selected because it derives the SOA local gain from quantum mechanical principles, without the assumption of linear dependence on carrier density made in [8], [23].

In section 1.2 the SOA reservoir model is derived, first without ASE, and then including ASE, resolved over a large number of wavelength bins.

In section 1.3 nonlinear effects in SOA will be studied and an analytical formula to calculate four-wave mixing caused by intraband ultrafast phenomena will be presented.

In section 1.4 an interesting application of the reservoir theory is shown. Through linearisation of the reservoir model some linear filters are derived, in order to show the impact of different frequency components on the integrated gain of the SOA.

1.1 Basic theory

The wideband model for a bulk SOA proposed in [9] is based on the numerical solution of the coupled equations for carrier-density rate and photon flux propagation for both forward and backward signals and spectral components of ASE. At a specified time t and position z in the SOA, the propagation equation of the photon flux $Q_k^{\pm}$ [photons/s] of the k^{th} forward (+) or backward (−) signal is:

$$\frac{dQ_k^{\pm}(z,t)}{dz} = \{\pm[\Gamma g_k(N) - \alpha(N)]\} Q_k^{\pm}(z,t) \tag{1.1}$$

where Γ is the fundamental mode confinement factor, g_k the material gain coefficient at the optical frequency ν_k of the k^{th} signal, α the material loss coefficient, and both are functions of the carrier density $N(z,t)$. The power of the propagating signal is related to its photon flux as $P_k^{\pm} = h\nu_k Q_k^{\pm}$ [W], being h Planck's constant. The ASE photon flux on each ASE wavelength channel obeys a similar propagation equation:

$$\frac{dQ_j^{\pm}(z,t)}{dz} = \pm[\Gamma g_j(N) - \alpha(N)] Q_j^{\pm}(z,t) + R_{sp,j} \tag{1.2}$$

where $R_{sp,j}(N)$ is the spontaneous emission rate coupled into the ASE channel at frequency ν_j.

The carrier density at coordinate z evolves as [9] :

$$\begin{aligned}\frac{dN(z,t)}{dt} &= \frac{I}{qdLW} - R(N(z,t)) - \\ &- \frac{\Gamma}{dW}\left\{\sum_{k=1}^{n_{sig}} g_k(N)\left(Q_k^{+}(z,t) + Q_k^{-}(z,t)\right)\right\} \\ &- \frac{2\Gamma}{dW}\left\{\sum_{j=1}^{n_{\mathrm{ASE}}} g_j(N)K_j\left(Q_j^{+}(z,t) + Q_j^{-}(z,t)\right)\right\}\end{aligned} \tag{1.3}$$

where: I is the bias current; q the electron charge; d, L, W the active region thickness, length, and width, respectively; $R(N)$ the recombination rate; n_{sig} the number of WDM signals; n_{ASE} the number of spectral components of the ASE; and K_j is an ASE multiplying factor which equals 1 for zero facets reflectivity [9]. A factor 2 in (1.3) accounts for two ASE polarisations. Note

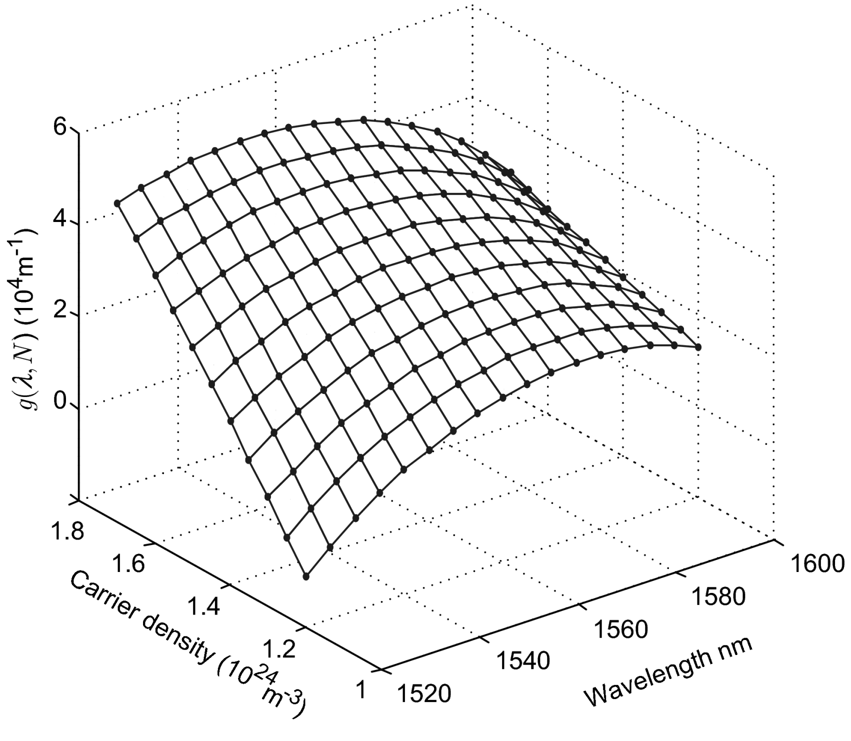

Figure 1.1: Gain coefficient $g(\lambda, N)$ versus wavelength and carrier density calculated from ([9], eq. (14)).

that (1.3) contains an important approximation: it is the sum of the signals and ASE powers (fluxes), instead of – more correctly – the power of the sum of the signals and ASE fields, that depletes the carrier density N. Therefore equation (1.3) neglects the carrier density pulsations due to beating among WDM channels that generate FWM and XPM in SOAs ([7]).

The material gain $g_k(N) \equiv g(\nu_k, N)$ is calculated as in ([9], eq. (14)). Fig. 1.1 plots the material gain versus N and wavelength $\lambda_k = c/\nu_k$ (c being the speed of light in vacuum) using the SOA parameters proposed by Connelly.

The time-varying solution of the coupled differential equations (1.1)-(1.3) is based on the assumption that the carrier density remains constant during a time step, and is achieved by first performing a spatial integration with carrier density fixed during each time step, followed by a time integration. Steady-state solutions are used as an initial condition for the subsequent time evolution. The Connelly model also neglects ultrafast phenomena such as CH and SHB.

In [24] a dynamic Connelly model has been proposed and the extraction of reservoir model linewidth dependent parameters from the Connelly gain profile is shown. This procedure is based on the linearisation of the gain profile shown in 1.1. This gain surface is linearised with respect to the carrier density, independently for each discrete wavelength. It is linearized applying the LMS method over a selected range of carrier density.

1.2 Reservoir model

We now derive the reservoir model for a travelling-wave SOA (zero facets reflectivity) fed by WDM signals neglecting ASE terms. The carrier density update equation (1.3) becomes:

$$\frac{\partial N(z,t)}{\partial t} = \frac{I}{qV} - \frac{N(z,t)}{\tau_r} - \frac{\Gamma}{A}\sum_{j\in S} g(N,\nu_j)Q_j(z,t) \tag{1.4}$$

where A and $V = AL$ are the active waveguide area and volume, respectively. The propagation equation (1.1) becomes for $k \in S = \{1,\ldots,n_{sig}\}$:

$$\frac{\partial Q_k(z,t)}{\partial z} = u_k\left\{\Gamma\sigma_k^g\left[N(z,t) - N_{0,k}\right] - \alpha\right\}Q_k(z,t) \tag{1.5}$$

where we introduced the propagation direction variable u_k which equals $+1$ for forward signals, and -1 for backward signals and the gain is now a linear approximation of the material gain $g(\nu, N))$ given by Connelly:

$$g(\nu,N) = p^1N(z,t)^1 + p^0N(z,t)^0 = p^1N(z,t)^1 + p^0 = \sigma_k^g(N - N_{0,k}) \tag{1.6}$$

where σ_k^g $[m^2]$ and N_{0k} $[m^{-3}]$ are wavelength dependent fitting coefficients. The formal solution of the propagation equation is obtained by multiplying both sides by u_k, dividing them by Q_k, and integrating both sides in dz from $z = 0$ to $z = L$ to get for every signal $Q_k^{out} = Q_k^{in}\exp(G_k - \alpha L)$, where the gain is

$$G_k(r) - \alpha L = \int_0^L \left\{\Gamma\sigma_k^g\left[N(z,t) - N_{0,k}\right] - \alpha\right\} \tag{1.7}$$

independently of the signal propagation direction. Now define the SOA *reservoir* as:

$$r(t) \triangleq A \int_0^L N(z,t)dz \tag{1.8}$$

which physically represents the total number of carriers in the SOA available for conversion into signal photons by the stimulated emission process. Since we have approximated both the recombination rate and the material gain as linear functions of N [11]:

$$\begin{array}{rcl} R(N) & \cong & N/\tau \\ g_k(N) & \cong & \sigma_k^g(N - N_{0,k}) \end{array} \tag{1.9}$$

where τ is the fluorescence time, then one obtains from (1.7):

$$G_k(r) - \alpha L = B_k r(t) - A_k - \alpha L \tag{1.10}$$

where

$$\begin{cases} A_k = \Gamma \sigma_k^g N_{0,k} L = -\Gamma p^0 L \\ B_k = \frac{\Gamma}{A} \sigma_k^g \end{cases} \tag{1.11}$$

are two dimensionless parameters. Also, one can multiply both sides of the second equation in (1.4) by A and integrate in dz to obtain

$$\dot{r} = -\frac{r}{\tau_r} + \frac{I}{q} - \sum_{j \in S} \int_0^L \left(\Gamma g(N, \nu_j) Q_j(z,t) \right) dz \tag{1.12}$$

$$\dot{r} = -\frac{r}{\tau_r} + \frac{I}{q} - \sum_{j \in S} \int_0^L \left(\frac{\partial Q}{\partial z} + \alpha Q(z,t) \right) dz \tag{1.13}$$

Now, for the calculation of the term $\int_0^L Q(z,t)dt$, we will use the approximation

$$Q(z,t) \simeq Q(0,t) e^{(G(r) - \alpha L) \frac{z}{L}} \tag{1.14}$$

so that substitution into (1.12) gives the following calculations:

$$\dot{r} = -\frac{r}{\tau_r} + \frac{I}{q} - \sum_{j \in S} \left\{ \left[Q_j^{out}(t) - Q_j^{in}(t) \right] + \alpha \int_0^L Q(0,t) e^{(G_j(r) - \alpha L) \frac{z}{L}} dz \right\}$$

$$\dot{r} = -\frac{r}{\tau_r} + \frac{I}{q} - \sum_{j \in S} \left\{ \left(e^{G_j(r) - \alpha L} - 1 \right) Q_j^{in}(t) + \alpha L Q^{in}(t) \frac{e^{G_j(r) - \alpha L} - 1}{G_j(r) - \alpha L} \right\}$$

$$\dot{r} = -\frac{r}{\tau_r} + \frac{I}{q} - \sum_{j \in S} \left\{ \left(e^{G_j(r) - \alpha L} - 1 \right) \left(1 + \frac{\alpha L}{G_j(r) - \alpha L} \right) Q_j^{in}(t) \right\}$$

which finally yield:

$$\dot{r} = -\frac{r}{\tau_r} + \frac{I}{q} - \sum_{j \in S} \left\{ \left(e^{G_j(r) - \alpha L} - 1 \right) \left(\frac{G_j(r)}{G_j(r) - \alpha L} \right) Q_j^{in}(t) \right\} \tag{1.15}$$

which is the *reservoir dynamic equation.* Note that it is quite similar to the EDFA reservoir equation [19].

There is a difference indeed between the reservoir model for the EDFAs and the one for the SOAs. In the first case it is easy to calculate the maximum value for the reservoir state variable. Hence one can normalise all the reservoir equations to this value, called the *relative inversion.* In the SOA, an absolute maximum value for the reservoir does not exist: it increases with injected current up to carrier saturation following this relation:

$$r_{max} = \frac{I \tau_r}{e} \tag{1.16}$$

which has been calculated at steady-state under the assumption that all the input fluxes are zero.

As in [11], one can easily show that, once the reservoir $r(t)$ is known, the cumulated phase of the k-th propagating signal at the output of the SOA can be obtained as

$$\phi_k^{out}(t) = -\frac{1}{2} \beta \frac{\Gamma \sigma_k^g}{A} (r(t) - N_{0k} V) \tag{1.17}$$

where β is the *linewidth enhancement factor.* Therefore it is possible to correctly take into account chirp-related distortions induced by dispersive optical components that follow the SOA.

1.2.1 Model with ASE

In order to include ASE in the model the whole spectrum is divided into N_{ASE} ASE channels with central frequency ν_k and with spacing $\Delta\nu$. Starting from the propagation equation for ASE (1.2) we write the general solution:

$$Q_k^{ASE}(z) = e^{\int_0^z \left\{\Gamma\sigma_k^g\left[N(z',t)-N_{0,k}\right]-\alpha\right\}dz'} \int_0^z \frac{R_{sp,k}(N(s))}{e^{\int_0^s \left\{\Gamma\sigma_k^g\left[N(z',t)-N_{0,k}\right]-\alpha\right\}dz'}}ds \tag{1.18}$$

Under the approximation that the carrier density is equal to its mean value, $N = \bar{N} = r/V$, one can derive:

$$Q_k^{ASE}(z) \simeq \frac{R_{sp,j}(\bar{N})}{\Gamma\sigma_k^g\left[\bar{N}-N_{0,k}\right]-\alpha}\left(e^{\left\{\Gamma\sigma_k^g\left[\bar{N}-N_{0,k}\right]-\alpha\right\}z}-1\right) \tag{1.19}$$

In the previous section we showed that the dynamic reservoir equation is derived from the integration of the carrier density equation (1.3) along the z direction; now that ASE is included this integration implies the solution of the following integral:

$$4\int_0^L \Gamma\sigma_k^g\left[N(z',t)-N_{0,k}\right]Q_k^{ASE}(z)dz \tag{1.20}$$

The first step is appling the substitution using the propagation equation for the ASE term:

$$\begin{aligned}&4\int_0^L \Gamma\sigma_k^g\left[N(z',t)-N_{0,k}\right]Q_k^{ASE}(z)dz = \\ &= 4\int_0^L R_{sp,j}(\bar{N})\frac{\Gamma\sigma_k^g\left[N(z',t)-N_{0,k}\right]}{\Gamma\sigma_k^g\left[\bar{N}-N_{0,k}\right]-\alpha}\left(e^{\left\{\Gamma\sigma_k^g\left[\bar{N}-N_{0,k}\right]-\alpha\right\}z}-1\right)dz\end{aligned} \tag{1.21}$$

which, under the same approximation used for equation (1.19), becomes

$$\begin{aligned}&4R_{sp,j}(\bar{N})\frac{\Gamma\sigma_k^g\left[\bar{N}-N_{0,k}\right]}{\Gamma\sigma_k^g\left[\bar{N}-N_{0,k}\right]-\alpha}\int_0^L\left(e^{\left\{\Gamma\sigma_k^g\left[\bar{N}-N_{0,k}\right]-\alpha\right\}z}-1\right)dz = \\ &\qquad = 4R_{sp,j}(\bar{N})\left(\frac{\sigma_k^g\left[\bar{N}-N_{0,k}\right]}{\sigma_k^g\left[\bar{N}-N_{0,k}\right]-\frac{\alpha}{\Gamma}}\right) \\ &\qquad\qquad \frac{e^{\left\{\Gamma\sigma_k^g\left[\bar{N}-N_{0,k}\right]-\alpha\right\}L}-1-\left\{\Gamma\sigma_k^g\left[\bar{N}-N_{0,k}\right]-\alpha\right\}L}{\left\{\Gamma\sigma_k^g\left[\bar{N}-N_{0,k}\right]-\alpha\right\}}\end{aligned}$$

Now, let's introduce a new term, $n_{sp,k}$, which is the spontaneous emission factor for the k-th frequency of ASE, calculated as the ratio between the emission gain coefficient $g'(\nu, N)$ and the material gain coefficient $g(\nu, N)$:

$$n_{sp,k} = \frac{g'(\nu, N)}{g(\nu, N)} = \frac{\Gamma\gamma_k^g \left[\bar{N} - N_{1,k}\right]}{\Gamma\sigma_k^g \left[\bar{N} - N_{0,k}\right]} = \frac{F_k r - E_k}{B_k r - A_k} \tag{1.22}$$

where the terms E_k and F_k are adimensional parameters similar to the ones of equation (1.11)

$$\begin{cases} E_k = \Gamma\gamma_k^g N_{1,k} L \\ F_k = \frac{\Gamma}{A}\gamma_k^g \end{cases} \tag{1.23}$$

that are calculated through the linearization of the emission gain coefficient $g'(\nu, N)$.

Now from equation (40) in [9] and from the previous linearisation we have:

$$\Delta\nu\, n_{sp,k} = \frac{R_{sp,j}(\bar{N})}{\Gamma\sigma_k^g \left[\bar{N} - N_{0,k}\right] - \alpha} \tag{1.24}$$

Using this last equation and the relations (1.10), (1.11), and (1.23) the integral of equation (1.21) becomes:

$$4\Delta\nu\, n_{sp,k} \left(\frac{G_k(r)}{G_k(r) - \alpha L}\right) \left[e^{G_k(r) - \alpha L} - 1 - (G_k(r) - \alpha L)\right] \tag{1.25}$$

So the reservoir equation including ASE terms can be written as:

$$\begin{aligned} \dot{r} \;=\; & -\frac{r}{\tau_r} + \frac{I}{q} - \sum_{j \in S} \left\{ \left(e^{G_j(r) - \alpha L} - 1\right) \left(\frac{G_j(r)}{G_j(r) - \alpha L}\right) Q_j^{in}(t) \right\} \\ & -4\Delta\nu \sum_{k \in ASE} n_{sp,k}(r) \left(\frac{G_k(r)}{G_k(r) - \alpha L}\right) \left[e^{G_k(r) - \alpha L} - 1 - (G_k(r) - \alpha L)\right] \end{aligned} \tag{1.26}$$

and the ASE fluxes at the output of the device can be calculated as:

$$Q_k^{ASE}(L) = \Delta\nu \frac{F_k r - E_k}{B_k r - A_k} \left(e^{G_k(r) - \alpha L} - 1\right) \tag{1.27}$$

where this relation works for the single polarisation case.

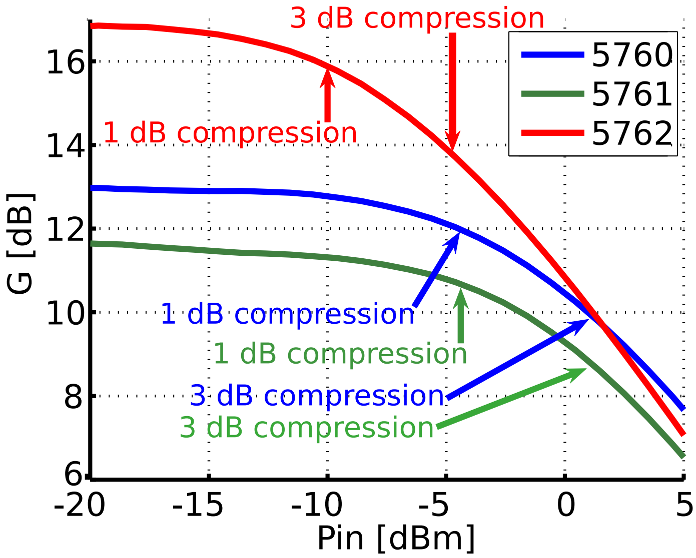

Figure 1.2: Alphion SOA gain saturation curves. Experimental results with a single CW channel centered at 1550 nm. Bias current I=250 mA.

1.2.2 Experimental results

Today there are few companies that still sell SOA devices. The companies we contacted in order to buy some SOA for an experimental validation of this model are *Kamelian Ltd.*, *CIP*, and *Alphion Corporation*. We choose to buy three SOA from *Alphion Corporation*: the model number of these SOA is 5760, 5761 and 5762. Their gain saturation curve is reported in Fig. 1.2 along with arrows that indicate their saturation point at 1 and 3 dB. We will see in this section how the reservoir model can be used to fit the dynamical behaviour of the Alphion SOA number 5762 in a single channel transmission. This MQW SOA has a gain shape that differs from the bulk SOA gain profile proposed by Connelly [9]. In order to fit the experimental results we had to look for the correct parameter values by trial and error. The best fitting parameters are reported in table 1.1. With these values we fitted the gain saturation experimental curve represented in Fig. 1.3. After this, one of the curves taken in the transmission experiment described in detail in section 2.4 was fitted. The selected curve is the one of the single channel case. The experimental results and the fitted theoretical curve are reported in Fig. 1.4, where good

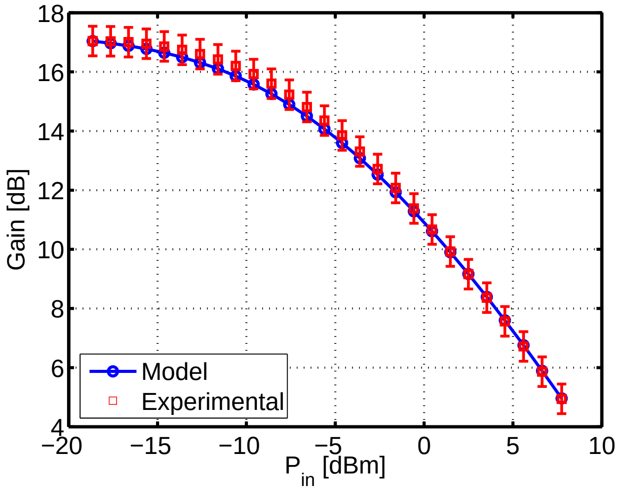

Figure 1.3: SOA5762 gain saturation curve. Experimental points and numerical fitting

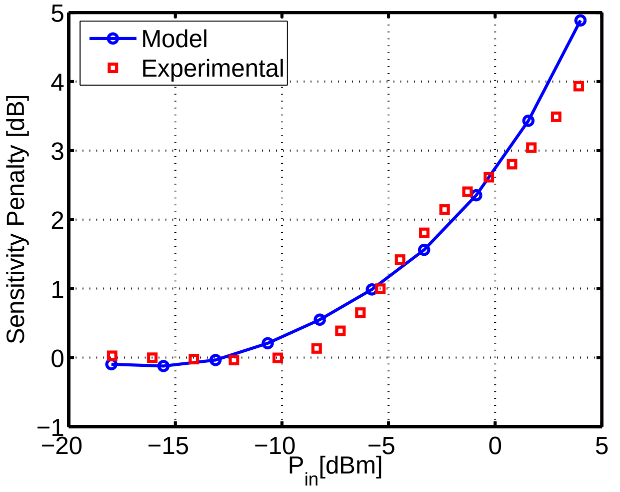

Figure 1.4: Penalty of a single channel transmission at 10 Gbit/s through SOA 5762. Experimental points and numerical fitting.

Parameter	Value	Parameter	Value
Length	300 μm	Overlap Factor, Γ	0.5
Carrier lifetime, τ	372 ps	Current, I	250 mA
Area	0.77 μm^2	Loss, α	6000 m$^-1$
Gain Parameter, A	9.28	Gain Parameter, B	3.36E-8

Table 1.1: Reservoir model parameters used to fit experimental results on Alphion SOA 5762.

match is observed, with a discrepancy of less than 0.5 dB for penalties up to 4 dB.

1.3 Nonlinear effects

In this section the nonlinear effects of the SOA will be analysed starting from what is present in the literature. The starting point is the article from Agrawal and Habbab [25] where a general theory for four-wave mixing (FWM) in case of multichannel transmission is developed. In this case the only *mechanism* responsible for FWM is the carrier density pulsation but the article is interesting because it lays the foundations for the theory. The nonlinear effects in SOAs have been studied mainly because many wavelength conversion devices are based on cross-pahse modulation (XPM), cross-gain modulation (XGM) or FWM. Unfortunately this is not our main interest but in an article like the one of Mecozzi [7] there is a basic theory that is very useful since it includes all the intraband *mechanisms* responsible for the ultrafast phenomena: spectral hole burning (SHB) and carrier heating (CH). The comprehension of this very complex subject is not sufficient since we want to find a simple way to include FWM in the reservoir model. All the models consider the CW case and do not take into account bit modulations, pattern effects and so on. Blumenthal [26] proposed an approach able to take these aspects into account and we will try to verify and improve his method.

1.3.1 WDM signals: carrier density pulsations

As a first step we will see how a WDM multiplex behaves inside an SOA. If all the channel lasers are equally spaced then the lowpass equivalent of the

WDM electrical field is:

$$\mathbf{E}(x,y,z,t) = \hat{i}U(x,y)\sum_{f\in\mathcal{S}} E_f(t)\exp(-j\omega_f t) \tag{1.28}$$

where $U(x,y)$ is the transverse field distribution supported by the SOA cavity geometry , $\hat{i}$ is the polarisation vector of the electric field, and in the sum there are all the single electric fields with their own frequency $\omega_f = \omega_0 + f\Omega$, where $f \in [-N_C, N_C]$ is integer and $\Omega = 2\pi\Delta f$ is channel spacing. The central channel, $f = 0$, has N_C channels both on its right and on its left. Considering ω_0 as the central pulsation we can write the low-pass equivalent of the electrical field with respect to the central pulsation as:

$$E(z,t) \triangleq \sum_{f=-N_C}^{N_C} E_f(z)\exp(-jf\Omega t) \tag{1.29}$$

Now we propose a different form of the carrier density equation (1.3). Like in [11] and [25], here we consider the square modulus of the total field instead of the sum of the powers of all the channels:

$$\frac{\partial N(z,t)}{\partial t} = \frac{I}{qV} - \frac{N}{\tau_S} - \frac{1}{A}\underbrace{\Gamma\sigma_g(N-N_0)}_{g(N)\ [m^{-1}]}\frac{|E|^2}{h\nu_0} \tag{1.30}$$

where N is the carrier density (in m^{-3}), I is the SOA driving current, q is the electron charge, V is the volume of the active cavity, τ_S is the carrier lifetime, A is transverse area, Γ is the confinement factor, σ_g is the gain, and $\nu_0 = \omega_0/(2\pi)$ is the central frequency of the WDM. In this case the gain is considered constant for all the channels.

By intraband dynamics we refer to processes that affect the shape of the carrier distribution in energy space, but not the corresponding total carrier density. From the work of Uskov *et al.* [27], we learn that the efficiency of FWM due to carrier density pulsation (CDP) drops for frequency detuning exceeding 10 GHz while intraband mechanisms have small relaxation times, impling that the bandwidth of intraband contributions can be very large. Basically there are two different kinds of intraband dynamics that can generate four-wave mixing: *spectral-hole burning* (SHB) is due to carrier-carrier scattering and *carrier heating* (CH) is due to the relaxation to the lattice temperature of "hot" carriers by the emission of optical phonons.

The propagation equation for the electrical field, neglecting the group velocity dispersion, is:

$$\frac{\partial E(z,t)}{\partial z} = \left(\frac{g-\gamma_{sc}}{2} - jk_{nl}\right) E(z,t) \tag{1.31}$$

where the gain, considering all the ultrafast effects, can be written as:

$$\begin{aligned} g &= g(N)\left[1-\varepsilon_{SHB}\left(h_{SHB}\otimes|E(z,t)|^2\right)\right] \\ &\quad -g_{CH}\varepsilon_{CH}\left(h_{CH}\otimes|E(z,t)|^2\right) \end{aligned} \tag{1.32}$$

where $\otimes$ denotes temporal convolution, and the wavenumber is:

$$\begin{aligned} k_{nl} &= \frac{1}{2}\left\{g(N)\left[\beta-\beta_{SHB}\varepsilon_{SHB}\left(h_{SHB}\otimes|E(z,t)|^2\right)\right]\right. \\ &\quad \left. -g_{CH}\varepsilon_{CH}\beta_{CH}\left(h_{CH}\otimes|E(z,t)|^2\right)\right\} \end{aligned} \tag{1.33}$$

where α are the scattering losses, ε_{SHB} and ε_{CH} are the efficiency of SHB and CH, β and β_{CH} are the *linewidth enhancement factor* and its extension to CH, and g_{CH} is a gain term.

Impulse responses $h_x(t)$ are normalised to one: $h_x(t)\otimes 1 = 1$. Their Fourier transmorfms are:

$$\left\{ \begin{array}{r} H_{SHB}(\omega) = \frac{1}{1-j\omega\tau_{SHB}} \\ H_{CH}(\omega) = \frac{H_{SHB}(\omega)}{1-j\omega\tau_{CH}} \end{array} \right. \tag{1.34}$$

where τ_{SHB} and τ_{CH} are their characteristic times.

In equations (1.30) the carrier density is stimulated by the square modulus of the electrical field. This means that in the case of a WDM field the beating between the signals will translate into beating in the carrier density. This effect, named *carrier density pulsation* (CDP) is responsible, together with SHB and CH, of the four-wave mixing in SOAs.

The power of the electrical field is:

$$\begin{aligned} P \triangleq |E|^2 &= \sum_{l\in\mathcal{S}}\sum_{n\in\mathcal{S}} E_n(z)E_l^*(z)\exp -j(n-l)\Omega t \\ &= \underbrace{\sum_{n\in\mathcal{S}}|E_n(z)|^2}_{} + \underbrace{\sum_{l,n\in\mathcal{S},\ l\neq n}\ \sum E_n(z)E_l^*(z)\exp -j(n-l)\Omega t}_{} \\ &= \qquad \overline{P} \qquad + \qquad \Delta P(z,t) \end{aligned} \tag{1.35}$$

where $\overline{P} = \sum_{n\in\mathcal{S}} P_n(z)$ is the constant part of the power and coincides with the sum of the powers of the WDM signals. Because of the beating terms in the power, which force the carrier density in equation (1.30), the solution of the carrier density will be in the form: $N(z,t) = \overline{N} + \Delta N(z,t)$.

Since the integrated current is normally constant along z, we can neglect the dependence of the gain on z, and write:

$$g(N(t)) = a(N - N_0) = \underbrace{a(\overline{N} - N_0)}_{g(\overline{N})} + a\Delta N(t) \tag{1.36}$$

where $a = \Gamma\sigma_g$. Using this result in eq. (1.30) we get:

$$\frac{\partial(N + \Delta N)}{\partial t} = \frac{I}{qV} - \frac{\overline{N} + \Delta N}{\tau_S} - \frac{g(\overline{N}) + a\Delta N(t)}{Ah\nu_0}(\overline{P} + \Delta P(t)) \tag{1.37}$$

and for the time-independent terms (CW solution):

$$0 = \frac{I}{qV} - \frac{\overline{N}}{\tau_S} - \frac{g(\overline{N})}{Ah\nu_0}\overline{P} \tag{1.38}$$

From this equation, by writing the complete expression of the gain term (1.36), we obtain

$$\overline{N}\left(\frac{1}{\tau_S} + \frac{a\overline{P}}{Ah\nu_0}\right) = \frac{I}{qV} + \frac{aN_0}{Ah\nu_0}\overline{P} \tag{1.39}$$

and multiplying each side by τ_s:

$$\overline{N}\left(1 + \frac{a\tau_S}{Ah\nu_0}\overline{P}\right) = N_0\frac{\tau_S}{qVN_0}I + N_0\frac{a\tau_S}{Ah\nu_0}\overline{P}. \tag{1.40}$$

Defining the *transparency current* as:

$$I_0 \triangleq \frac{qVN_0}{\tau_S} \tag{1.41}$$

and the *saturation power* as:

$$P_S \triangleq \frac{Ah\nu_0}{a\tau_S} = \frac{Ah\nu_0}{\Gamma\sigma_g\tau_S} \tag{1.42}$$

then equation (1.38) can be written as

$$\overline{N} = N_0\frac{\frac{I}{I_0} + \frac{\overline{P}}{P_S}}{1 + \frac{\overline{P}}{P_S}} \tag{1.43}$$

or, equivalently

$$\overline{N} - N_0 = N_0 \frac{\frac{I}{I_0} - 1}{1 + \frac{\overline{P}}{P_S}} \tag{1.44}$$

If we define the small signal gain as:

$$g_0 \triangleq aN_0(\frac{I}{I_0} - 1) \tag{1.45}$$

in $[m^{-1}]$, equation (1.36) can be written as:

$$g(\overline{N}) = a(\overline{N} - N_0) = \frac{g_0}{1 + \frac{\overline{P}}{P_S}}. \tag{1.46}$$

The time varying part of equation (1.37), if we neglect the products between ΔN and ΔP, becomes:

$$\frac{\partial \Delta N}{\partial t} = -\frac{\Delta N}{\tau_S} - \frac{a\overline{P}}{Ah\nu_0}\Delta N(t) - \frac{g(\overline{N})\Delta P(t))}{Ah\nu_0} \tag{1.47}$$

where we have:

$$\Delta P(t) = \sum_{\substack{l,n \in \mathcal{S} \\ l \neq n}} \sum E_n(z) E_l^*(z) \exp -j(n-l)\Omega t = \sum_{\substack{q=-2N_C \\ q \neq 0}}^{2N_C} \Delta P_q \exp(-jq\Omega t) \tag{1.48}$$

in which we have defined:

$$\Delta P_q = \sum_{\substack{l,n \in \mathcal{S}, \\ l \neq n}} \sum_{n-l=q} E_n(z) E_l^*(z). \tag{1.49}$$

The summation index in equation (1.48) goes from $-2N_C$ to $2N_C$. Because of the linearity of the differential equation the solution will exist on the same range:

$$\Delta N(t) = \sum_{\substack{q=-2N_C \\ q \neq 0}}^{2N_C} \Delta N_q \exp(-jq\Omega t). \tag{1.50}$$

Each ΔN_q can be extracted from the differential equation when the stimulating term is $\Delta P_q \exp(-jq\Omega t)$:

$$\begin{aligned}\frac{\partial \Delta N_q \exp(-jq\Omega t)}{\partial t} &= -\Delta N_q \exp(-jq\Omega t)\left(\frac{1}{\tau_S} + \frac{a\overline{P}}{Ah\nu_0}\right) \\ &\quad - \frac{g(\overline{N})}{Ah\nu_0}\Delta P(t)\exp(-jq\Omega t) \end{aligned} \tag{1.51}$$

from which we obtain, after some manipulations:

$$\Delta N_q = -a(\overline{N} - N_0)\frac{\tau_S}{Ah\nu_0}\frac{\Delta P_q}{\left(1 + \frac{\overline{P}}{P_S} - jq\Omega\tau_S\right)}. \tag{1.52}$$

Using the definition (1.42) and the result (1.46) we obtain:

$$\Delta N_q = -\frac{1}{a}\left(\frac{g_0}{1 + \frac{\overline{P}}{P_S}}\right)\frac{1}{\left(1 + \frac{\overline{P}}{P_S} - jq\Omega\tau_S\right)}\frac{\Delta P_q}{P_S}. \tag{1.53}$$

Using equations (1.46), (1.49), and (1.53) in (1.36) we finally have the expression for the gain with carrier density pulsation:

$$g(N) = \frac{g_0}{1 + \frac{\overline{P}}{P_S}}\left[1 - \sum_{\substack{q=-2N_C \\ q\neq 0}}^{2N_C} \frac{\displaystyle\sum_{\substack{l\in\mathcal{S} \\ n-l=q}}\sum_{\substack{n\in\mathcal{S} \\ n\neq l}} E_n(z)E_l^*(z)}{P_S}\frac{\exp(-jq\Omega t)}{1 + \frac{\overline{P}}{P_S} - jq\Omega\tau_S}\right] \tag{1.54}$$

that is the main result of this section. This equation shows that the gain is modulated by the beating terms of the square modulus of the electrical field. This is the origin of carrier density pulsation. But there is more: in fact the equation contains a term which is a kind of filter. Each beat term has a frequency dependent coefficient. This means that the channel spacing is a fundamental parameter. If the channel spacing is much larger than the 3dB bandwidth of the CDP filter

$$H_{CDP}(\omega) \triangleq \frac{1}{1 + \frac{\overline{P}}{P_S} - j\omega\tau_S} \tag{1.55}$$

there will be no CDP at all. This bandwith depends on the carrier lifetime τ_s and on the saturation level of the amplifier $\frac{\overline{P}}{P_S}$. In a traditional SOA the bandwith of this filter is around 10 GHz. Since optical telecommunication systems work with spacings of at least 50 GHz on the ITU grid, then it is quite evident that this mechanism will not be the one responsible for four-wave mixing in SOAs in WDM environments.

1.3.2 Complete propagation equations

In the last section we were working under an approximation: we were neglecting the z dimension and we calculated all the results with the gain expression of equation (1.36). Now let's consider again the original equations for the gain (1.32) and wavenumber (1.33). First of all it should be noted that:

$$\begin{aligned} h \otimes |E|^2 = h \otimes P &= h \otimes \overline{P} + h \otimes \Delta P(t) = \overline{P} + h \otimes \Delta P(t) \\ &\overset{(1.48)}{=} \overline{P} + \sum_{\substack{q=-2N_C \\ q \neq 0}}^{2N_C} \Delta P_q H(q\Omega) \exp(-jq\Omega t). \end{aligned} \tag{1.56}$$

Now this relation is used together with equation (1.54) to rewrite gain (1.32) and wavenumber (1.33) as:

$$\begin{aligned} g = \frac{g_0}{1+\frac{\overline{P}}{P_S}} & \left[1 - \sum_{\substack{q=-2N_C \\ q \neq 0}}^{2N_C} \frac{\Delta P_q / P_S}{1 + \frac{\overline{P}}{P_S} - jq\Omega\tau_S} \exp(-jq\Omega t) \right] \\ & \left[1 - \varepsilon_{SHB}\overline{P} - \varepsilon_{SHB} \sum_{\substack{q'=-2N_C \\ q' \neq 0}}^{2N_C} \Delta P_{q'} H_{SHB}(q'\Omega) \exp(-jq'\Omega t) \right] \\ & - g_{CH}\varepsilon_{CH} \left[\overline{P} + \sum_{\substack{q=-2N_C \\ q \neq 0}}^{2N_C} \Delta P_q H_{CH}(q\Omega) \exp(-jq\Omega t) \right] \end{aligned} \tag{1.57}$$

$$
\begin{aligned}
2k_{nl} = {} & \frac{\beta g_0}{1+\frac{\overline{P}}{P_S}}\left[1-\sum_{\substack{q=-2N_C\\ q\neq 0}}^{2N_C}\frac{\Delta P_q/P_S}{1+\frac{\overline{P}}{P_S}-jq\Omega\tau_S}\exp(-jq\Omega t)\right] \\
& - g_{CH}\varepsilon_{CH}\beta_{CH}\left[\overline{P}+\sum_{\substack{q=-2N_C\\ q\neq 0}}^{2N_C}\Delta P_q H_{CH}(q\Omega)\exp(-jq\Omega t)\right]
\end{aligned}
\qquad (1.58)
$$

where the filter H_{CDP} is defined by (1.55) and the filters H_{CH} and H_{SHB} by (1.34). Now equations (1.57) and (1.58) can be summarised:

$$
\left\{
\begin{array}{l}
g = \frac{g_0}{1+\frac{\overline{P}}{P_S}}(1-\varepsilon_{SH}\overline{P}) - g_{CH}\varepsilon_{CH}\overline{P} + \\
-\sum_{q\neq 0}\Delta P_q \left\{ \frac{g_0}{1+\frac{\overline{P}}{P_S}}[\varepsilon_{SHB}H_{SHB}(q\Omega)+\dfrac{H_{CDP}(q\Omega)}{P_S}] + \right. \\
\left. g_{CH}\varepsilon_{CH}H_{CH}(q\Omega)\right\}\exp(-jq\Omega t) \\
\\
2k_{nl} = \frac{\beta g_0}{1+\frac{\overline{P}}{P_S}} - g_{CH}\varepsilon_{CH}\beta_{CH}\overline{P} + \\
\sum_{q\neq 0}\Delta P_q\left[\frac{\beta g_0}{1+\frac{\overline{P}}{P_S}}\frac{1}{P_S}H_C(q\Omega)+\beta_{CH}g_{CH}\varepsilon_{CH}H_{CH}(q\Omega)\right] \\
\exp(-jq\Omega t)
\end{array}
\right.
\qquad (1.59)
$$

where all the products between beating terms of gain and power have been neglected as in [7].

The new form of propagation equation, using this last result, will be:

$$
\begin{aligned}
& \sum_{f\in\mathcal{F}}\left(\frac{dE_f(z)}{dz}\right)\exp(-jf\Omega t) = \\
& \qquad\qquad \left(\frac{g-\alpha-j2k_{nl}}{2}\right)\sum_m E_m(z)\exp(-jm\Omega t)
\end{aligned}
\qquad (1.60)
$$

where the set $\mathcal{F}$ includes all the input signals and all the FWM generated contributions. A single tone of this equation, using the equations in (1.59), will become

$$\frac{\partial E_f(z)}{\partial z} = \frac{1}{2}\left[-\alpha + \frac{g_0}{1+\frac{\overline{P}}{P_S}}(1 - j\beta - \varepsilon_{SHB}\overline{P}) - g_{CH}\varepsilon_{CH}\overline{P}(1-\beta_{CH})\right] E_f + \\ - \sum_{\substack{m,q \text{ t.c. } m+q=f \\ q\neq 0}} E_m \Delta P_q k_q \quad (1.61)$$

where the new parameter k_q is defined as:

$$k_q = \frac{1}{2}\frac{g_0}{1+\frac{\overline{P}}{P_S}}\left[\frac{1}{P_S}H_{CDP}(q\Omega)(1-j\beta) + \varepsilon_{SHB}H_{SHB}(q\Omega)\right] + \\ g_{CH}\varepsilon_{CH}H_{CH}(q\Omega)(1-j\beta_{CH}) \quad (1.62)$$

In equation (1.61) the sum is related to all the fields different from the one on the left-hand side. The equation could look more proper if we define another parameter that contains all the gain terms that multiply the field E_f:

$$\frac{\partial E_f}{\partial z} = aE_f \quad - \sum_{\substack{m,q \text{ t.c. } m+q=f \\ q\neq 0}} E_m \Delta P_q k_q \quad (1.63)$$

where

$$a = \frac{1}{2}\left[-\alpha + \frac{g_0}{1+\frac{\overline{P}}{P_S}}(1 - j\beta - \varepsilon_{SHB}\overline{P}) - g_{CH}\varepsilon_{CH}\overline{P}(1-\beta_{CH})\right] \quad (1.64)$$

Now, to better understand who is responsible for the nonlinear effects in SOAs, we can use equation (1.49) and write:

$$\frac{\partial E_f}{\partial z} = a_f E_f - \sum_{\substack{n\neq l,\, m\neq l \\ m+n-l=f}} \sum E_m E_n E_l^* k_{n-l} \quad (1.65)$$

where we have defined:

$$a_f = \frac{1}{2}\left[-\alpha + \frac{g_0}{1+\frac{\overline{P}}{P_S}}(1 - j\beta - \varepsilon_{SHB}\overline{P}) - g_{CH}\varepsilon_{CH}\overline{P}(1-\beta_{CH})\right] - \\ \sum_{\substack{s\in\mathcal{S} \\ s\neq f}} P_S k_{f-s} \quad (1.66)$$

This definition can be expanded in order to separate all the different nonlinear effects (self and cross effects):

$$a_f = \frac{1}{2}[-\alpha + \frac{g_0}{1+\frac{\overline{P}}{P_S}}(1-j\beta)] - \frac{1}{2}[\frac{g_0}{1+\frac{\overline{P}}{P_S}}\varepsilon_{SH} + g_{CH}\varepsilon_{CH}(1-j\beta)]P_f$$
$$-\frac{1}{2}\left\{\sum_{\substack{j\in\mathcal{S}\\ j\neq f}} P_j\left[\frac{g_0}{1+\frac{\overline{P}}{P_S}}(\frac{1-j\beta}{P_S}H_{CDP}((f-j)\Omega) + \varepsilon_{SHB}(1+H_{SHB}((f-j)\Omega)))\right.\right.$$
$$\left.\left. + g_{CH}(1-j\beta_{CH})\varepsilon_{CH}(1+H_{CH}((f-j)\Omega)\right]\right\} \quad (1.67)$$

This last equation, together with equation (1.62), completes the main result of this section which is equation (1.65). This last equation is a very interesting result because it is almost identical to the one used to study four-wave mixing in fibres. The important difference is the dependence of the coefficient k_q on the difference of two indexes only, while in fibre FWM the coefficient depends on all the tree indexes under the sum sign. This is the equation that needs to be solved in order to know the electrical field in presence of nonlinear effects in SOAs.

Solution in linear regime

When an amplifier works far from the saturation point, the following approximations hold: $\varepsilon_{CH}\overline{P} \ll 1$, $\varepsilon_{SHB}\overline{P} \ll 1$, and$\frac{\overline{P}}{P_S} \ll 1$. So, for every $f \in \mathcal{S}$, one has:

$$a_f \simeq a = \frac{1}{2}[-\alpha + g_0(1-j\beta)] \quad (1.68)$$

and

$$k_q \simeq \frac{1}{2}\left\{g_0\left[\frac{1-j\beta}{P_S}H_{CDP}(q\Omega) + \varepsilon_{SHB}H_{SHB}(q\Omega)\right]\right.$$
$$\left. + g_{CH}\varepsilon_{CH}(1-j\beta_{CH})H_{CH}(q\Omega)\right\}. \quad (1.69)$$

In this particular case, the solution of equation (1.65) is:

$$E_f(z) = e^{aL}E_f(0) + E_{FWM,f}(L) = e^{aL}\left(E_f(0) + E_{FWM,f}(0)\right) \quad (1.70)$$

where

$$E_{FWM,f}(L) = -\sum_{\substack{n\neq l,\, m\neq l\\ m+n-l=f}} \sum E_m E_n E_l^* k_{n-l} e^{aL} \int_0^L e^{(a+a^*)s} ds \tag{1.71}$$

If we assume that the small-signal gain $G_{dB}^0 \gg 1$ and we approximate

$$a + a^* = -\alpha + g_0 = \frac{G_{dB}^0}{4.34L} \tag{1.72}$$

we have, like [28],

$$E_{FWM,f}(L) = -\sum_{\substack{n\neq l,\, m\neq l\\ m+n-l=f}} \sum E_m(L) E_n(L) E_l^*(L) c_{n-l} \tag{1.73}$$

where

$$c_{n-l} \triangleq \frac{4.34L}{G_{dB}^0} k_{n-l} = \frac{G_{dB}^0 - 1}{lnG_{dB}^0} \tag{1.74}$$

If we consider, like Mecozzi [7], that $g_{CH} = g_0$ we can write the final expression for the four-wave mixing coefficients in the non saturated case as:

$$c_q = \frac{(G_{dB}^0 - 1)}{\ln G_{dB}^0} \frac{g_0 L}{2} \left[\frac{1 - j\beta}{P_S} H_{CDP}(q\Omega) + \right. \\ \left. \varepsilon_{SHB} H_{SHB}(q\Omega) + \varepsilon_{CH}(1 - j\beta_{CH}) H_{CH}(q\Omega) \right]. \tag{1.75}$$

Solution with saturated amplifier

The solution of equation (1.65) in a general case is a hard problem to face. The most challanging obstacle in the solution of the equation is the presence of the integral of the parameter a_f. Now, through some approximations, we will show a way to get rid of that term. If we assume that the FWM effects are negligible then $k_q \equiv 0$. In this case the propagation equation becomes

$$\frac{\partial E_f}{\partial z} = aE_f \tag{1.76}$$

where

$$a_f \equiv a = \frac{1}{2} \left\{ -\alpha + \frac{g_0 \left[(1 - j\beta) - \varepsilon_{SHB} \overline{P} \right]}{1 + \frac{\overline{P}}{P_S}} - g_{CH} \varepsilon_{CH} \overline{P} (1 - j\beta_{CH}) \right\}. \tag{1.77}$$

By working with the complex conjugate of the progation equation we get:

$$\frac{\partial P_f}{\partial z} = \frac{\partial |E_f|^2}{\partial z} = E_f \frac{\partial E_f^*}{\partial z} + E_f^* \frac{\partial E_f}{\partial z} = a^* P_f + a P_f = 2\Re(a) P_f \tag{1.78}$$

where $\Re(a)$ is the real part of a. The presence of $\overline{P}$ in the a term of the differential equation suggests to sum the differential equation for each signal in order to obtain the equation:

$$\frac{\partial \overline{P}}{\partial z} = 2\Re(a)\overline{P} = \left[-\alpha + \frac{g_0}{1 + \frac{\overline{P}}{P_S}} (1 - \varepsilon_{SHB}\overline{P}) - g_{CH}\varepsilon_{CH}\overline{P} \right] \overline{P}. \tag{1.79}$$

In the approximation that $\varepsilon_{CH}\overline{P} \ll 1$, and $\varepsilon_{SHB}\overline{P} \ll 1$, we obtain this new equation for the average power:

$$\frac{\partial \overline{P}}{\partial z} = (-\alpha + \frac{g_0}{1 + \overline{P}/P_S} \overline{P}) \tag{1.80}$$

that is an approximation valid when the FWM pumps are not depleted. As a last step we write:

$$\begin{aligned} \ln G(L) \triangleq \ln \frac{\overline{P}(L)}{\overline{P}} = \int_0^L (-\alpha + \frac{g_0}{1 + \overline{P}/P_S}) dz = \\ = -\alpha L + \int_0^L \frac{g_0}{1 + \overline{P}/P_S} dz. \end{aligned} \tag{1.81}$$

This equation will help to solve the original problem.

Equation (1.65) is an ordinary differential equation of the type:

$$\frac{\partial x_f}{\partial z} = a_f(z) x_f + b(z) \tag{1.82}$$

and its solution is:

$$x_f(z) = \underbrace{\exp\left(\int_0^L a_f(s) ds \right) x_f(0)}_{\hat{x}_f(z)} + \underbrace{\int_0^L \exp\left(\int a_f(u) du \right) b(s) ds}_{x_{FWM,f}(z)} \tag{1.83}$$

where $a_f(z)$ is defined by equation (1.67) and

$$b(z) = - \sum_{\substack{n \neq l,\, m \neq l \\ m+n-l=f}} \sum E_m E_n E_l^* k_{n-l} \tag{1.84}$$

The autonomous term of the differential equation $\hat{x}_f(z)$ depends on the solution of the following integral:

$$\int_0^L a(z)dz = \frac{1}{2}\left[\int_0^L \left(-\alpha + \frac{g_0}{1+\overline{P}/P_S}\right)dz - i\beta\int_0^L \frac{g_0}{1+\overline{P}/P_S}dz\right] \tag{1.85}$$

that, thanks to the approximation provided by equation (1.81), gives the solution:

$$\hat{x}_f(L) = x_f(0)G(L)^{\frac{1-i\beta}{2}}e^{-i\frac{\beta}{2}\alpha L} \tag{1.86}$$

To solve the forced term of the differential equation $x_{FWM,f}(z)$ it is necessary to calculate a further integral, derived like integral (1.81) from equation (1.80) :

$$\ln\frac{G(L)}{G(s)} = \int_s^L (-\alpha + \frac{g_0}{1+\overline{P}/P_S}) = -\alpha(L-s) + \int_s^L \frac{g_0}{1+\overline{P}/P_S}dz \tag{1.87}$$

Once this equivalence is known, we can write:

$$\begin{aligned} x_{FWM,f}(L) = &\int_0^L \left(\frac{G(L)}{G(s)}\right)^{\frac{1-i\beta}{2}} e^{-i\frac{\beta}{2}\alpha(L-s)} \\ &\Bigg[-\sum_{\substack{n\neq l,\, m\neq l \\ m+n-l=f}}\sum E_m(0)E_n(0)E_l^*(0)\left(G(s)^{\frac{1-i\beta}{2}}\right)^2 \\ &\qquad G(s)^{\frac{1+i\beta}{2}}e^{-i\frac{\beta}{2}\alpha s}k_{n-l}(s)\Bigg]ds \end{aligned} \tag{1.88}$$

$$= -G(L)^{\frac{1-i\beta}{2}}e^{-i\frac{\beta}{2}\alpha L}\sum\sum_{\substack{n\neq l,\, m\neq l \\ m+n-l=f}} E_m(0)E_n(0)E_l^*(0)\int_0^L G(s)k_{n-l}(s)ds \tag{1.89}$$

The total solution of the differential equation (1.83) can now be written as:

$$x_f(L) = G(L)^{\frac{1-i\beta}{2}}e^{-i\frac{\beta}{2}\alpha L}\left(x_f(0) - \sum\sum_{\substack{n\neq l,\, m\neq l \\ m+n-l=f}} E_m(0)E_n(0)E_l^*(0)c_{n-l}\right) \tag{1.90}$$

where

$$c_q = \int_0^L G(s) k_q(s) ds. \tag{1.91}$$

Now, going back to the time varing electrical field and using this input-output solution, we can write the expression of the output field as:

$$E_{f,\mathrm{OUT}} = G_L(t)^{\frac{1-i\beta}{2}} e^{-i\frac{\beta}{2}\alpha L} \left[E_{f,\mathrm{IN}}(t) + E_{\mathrm{FWM,IN}}(t) \right] \tag{1.92}$$

where

$$E_{\mathrm{FWM,IN}}(t) = -\sum_{\substack{n\neq l,\, m\neq l \\ m+n-l=f}}\sum E_{m,\mathrm{IN}}(t) E_{n,\mathrm{IN}}(t) E^*_{l,\mathrm{IN}}(t) c_{n-l}. \tag{1.93}$$

In order to calculate this solution the integral in equation (1.91) should be solved. The solution of the integral, calculated with the tools explained in the appendix A, is:

$$\begin{aligned} c_q = \frac{1-i\beta}{2\overline{P}} \left\{ \frac{1}{1-iq\Omega\tau_s\xi} \left[\ln\left(\frac{1+\overline{P}/P_S G_L - iq\Omega\tau_s}{1+\overline{P}/P_S - iq\Omega\tau_s} \right) + \xi \ln\frac{G_0}{G_L} \right] \right\} + \\ \frac{P_S \varepsilon_{SH} H_{SH}(q\Omega)}{2\overline{P}} \ln\frac{G_0}{G_L} + \\ g_{CH} \frac{1-i\beta_{CH}}{2} \frac{P_S \varepsilon_{CH} H_{CH}(q\Omega)}{\overline{P}} \frac{1}{g_0\xi} \left[\ln\frac{G_0}{G_L} - (G_L - 1)\frac{\overline{P}}{P_S} \right] \end{aligned} \tag{1.94}$$

where $\ln G_0 = (g_0 - \alpha)L$ is the non-saturated gain and $\xi = \alpha/g_0$.

1.3.3 Penalty evaluation

From a numerical point of view the coefficients that can be calculated as per equation (1.94) are sufficient to extend the reservoir model with four-wave mixing. In fact FWM terms can be added after the calculation of $G(r(t))$ as per equation (1.92). Nevertheless, it would be usefull to derive an analitical rule for the *sensitivity penalty* (SP). Consdiering that the FWM mechanisms are much faster than the bit-pattern we may extend the rules derived in the previous section for CW signals to modulated signals. Let's consider an on-off keying (OOK) modulated signal; we consider that it will be sufficient to calculate the variance of the FWM additive term σ_{FWM} when a "one" is received. When the *relative intensity noise* (RIN) of the FWM term is a

Gaussian Random Variable the SP can be calculated from σ_{FWM}. We now work with modulated signals. For each signal E_s with $s \in \mathcal{S}$ we have:

$$E_s(0) = \sqrt{P_P} b_s(t) e^{j\varphi_s} \tag{1.95}$$

where P_p is the peak power, $b_s(t)$ is the bit pattern function of time and φ_s is a uniform random variable $\mathcal{U}([-\pi;\pi])$. The photocurrent generated by this field on the photorecevier will be:

$$\begin{aligned} I = R|E_f(L)|^2 = RG^0_{dB}P_P & \left| 1 + \frac{E_{FWM,f}(0)}{\sqrt{P_P}} e^{-j\varphi_f} \right|^2 \\ \simeq RG^0_{dB}P_P & \left(1 + \underbrace{2\Re\left\{ \frac{E_{FWM,f}(0)}{\sqrt{P_P}} e^{-j\varphi_f} \right\}}_{RIN} \right) \end{aligned} \tag{1.96}$$

where R is the responsivity, and the term to isolate is:

$$\begin{aligned} \mathrm{RIN} = -2\Re \Bigg\{ & \sum_{\substack{n\neq l,\, m\neq l \\ m+n-l=f}} \sum c_{n-l} \sqrt{P_P} b_m(t) e^{j\varphi_m} \\ & \sqrt{P_P} b_n(t) e^{j\varphi_n} \sqrt{P_P} b_l(t) e^{-j\varphi_l} \frac{e^{-j\varphi_f}}{\sqrt{P_P}} \Bigg\} \end{aligned} \tag{1.97}$$

If we define $\Psi_{mnl} \triangleq \varphi_m + \varphi_n - \varphi_l - \varphi_f$ equation (1.97) becomes:

$$\mathrm{RIN} = -2P_P \sum_{\substack{n\neq l,\, m\neq l \\ m+n-l=f}} \sum \underbrace{b_m(t) b_n(t) b_l(t)}_{B_{mnl}(t)} \Re\left\{ c_{n-l} e^{j\Psi_{mnl}} \right\} \tag{1.98}$$

All the RIN random variables can be grouped to a single term by defining:

$$V_{mnl} \triangleq B_{mnl}(t) e^{j\Psi_{mnl}} \tag{1.99}$$

It can be shown that V_{mnl} and $V_{m'n'l'}$ are incorrelated if one of the three indexes is different, except when m and n are swapped.

For the sake of simplicity let's consider the central channel of the WDM comb, the one represented by $f = 0$. All the points of the space of the indexes (m, n, l) involved in the sum are the ones that solve the equation

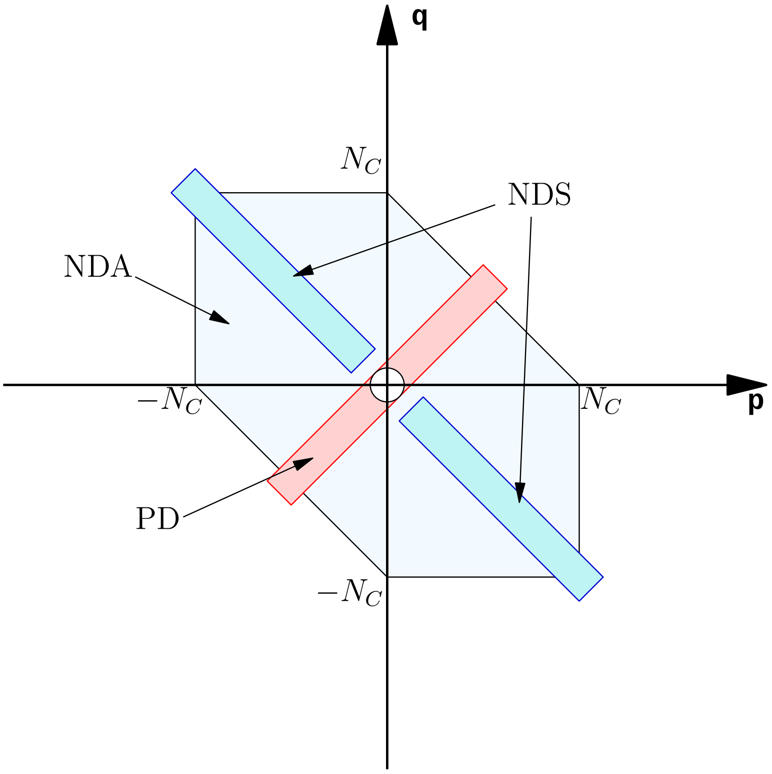

Figure 1.5: Graphic representation of domain D on the (p, q) plane.

$m + n - l = f = 0$. For this reason it is more practical to apply a change of indexes:

$$\begin{cases} m - l = p \\ n - l = q \end{cases} \tag{1.100}$$

where these two new indexes have always the domain $[-N_C; N_C]$ and have to satisfy the relation $q, p \neq 0$. Using p and q it is now possible to draw on the (p, q) plane the domain D involved in the summation term. This domain is represented in Fig. 1.5.

When the condition $m = n \Rightarrow p = q$ is verified we have the so called partially degenerate (PD) terms. These terms are generating FWM through the combination $E_m^2 E_l^*$. When the condition $l = 0 \Rightarrow p = -q$ is verified we have the so called symmetric non-degenerate (SND) terms. These terms are generating FWM through the combination $E_m E_{-m} E_0^*$. PD terms have this property: $B_{mnl}(t) = b_m^2(t) b_l(t) = b_m(t) b_l(t)$, the bit pattern depends only on two bits. The same is true for NDS terms where $B_{mnl} = b_m(t) b_{-m}(t)$ when $b_f(t) = 1$. The domain D can be divided into three areas: PD, NDS and non-degenerate asymmetric (NDA). So equation (1.98) can be written as:

$$\text{RIN} = -2P_P \Re \left\{ \sum_{(p,q)\in D} c_q V_{pq} \right\} \tag{1.101}$$

where $V_{pq} = V_{mnl}$. At this point it is easy to notice that domain D is symmetric around the line $p = q$ so that it is possible to fold it into a new domain D_1 obtaining:

$$\text{RIN} = -2P_P \Re \left\{ \sum_{(p,q)\in \text{PD}} |c_q| V_{qq} + \sum_{(p,q)\in \text{ND}} |c_q + c_p| V_{pq} \right\} \tag{1.102}$$

where $V_{qq} = B_{qq} e^{j\Phi_{qq}} = b_{q+l}(t) b_l(t) e^{j\Phi_{qq}}$ where Φ_{qq} is a uniform random variable and $V_{pq} = B_{pq}(t) e^{j\Phi_{pq}} = b_{p+l}(t) b_{q+l}(t) b_l(t) e^{j\Phi_{pq}}$ where Φ_{pq} is still a uniform random variable. So, equation (1.102) becomes:

$$\text{RIN} = -2P_P \left[\sum_{(p,q)\in \text{PD}} |c_q| B_{qq} \cos \Phi_{qq} + \sum_{(p,q)\in \text{ND}} |c_q + c_p| B_{pq} \cos \Phi_{pq} \right] \tag{1.103}$$

From this equation we derive:

$$\begin{aligned} \sigma_{FWM}^2 &= \text{VAR[RIN]} = \\ & 4P_P^2 \left[\sum_{(p,q)\in \text{PD}} |c_q|^2 E(B_{qq}^2) \frac{1}{2} + \sum_{(p,q)\in \text{ND}} |c_q + c_p|^2 E(B_{pq}^2) \frac{1}{2} \right] \end{aligned} \tag{1.104}$$

From [29] we have these two important results:

$$E[B_{qq}^2] = \frac{1}{4} \eta_{II} \tag{1.105}$$

$$E[B_{pq}^2] = \begin{cases} \frac{1}{8}\eta_I & \text{for NDA terms} \\ \frac{1}{4}\eta_{II} & \text{for NDS terms} \end{cases} \tag{1.106}$$

where the value of η depends on the bit pattern temporal alignment:

$$\begin{cases} \eta_I = \eta_{II} = 1 & \text{bit-aligned channels} \\ \eta_I = 49/80 \quad \text{and} \quad \eta_{II} = 17/24 & \text{asynchronous channels.} \end{cases} \tag{1.107}$$

Hence

$$\sigma^2_{FWM} = 2P_P^2 \left[\frac{1}{4}\eta_{II} \sum_{(p,q)\in \mathrm{PD}} |c_q|^2 + \frac{1}{4}\eta_{II} \sum_{(p,q)\in \mathrm{NDS}} |c_q + c_p|^2 + \right.$$
$$\left. \frac{1}{8}\eta_I \sum_{(p,q)\in \mathrm{NDA}} |c_q + c_p|^2 \right] \tag{1.108}$$

Thanks to geometric considerations on domain D_1 we can write:

$$\sum_{(p,q)\in \mathrm{PD}} |c_q|^2 = \sum_{\substack{q=-\left\lfloor \frac{N_C}{2} \right\rfloor \\ q\neq 0}}^{\left\lfloor \frac{N_C}{2} \right\rfloor} |c_q|^2 \tag{1.109}$$

$$\sum_{(p,q)\in \mathrm{NDS}} |c_q + c_p|^2 = \sum_{p=1}^{N_C} |c_p + c_{-p}|^2 \tag{1.110}$$

$$\begin{aligned} \sum_{(p,q)\in \mathrm{NDA}} |c_q + c_p|^2 = & \sum_{k=-(N_C-1)}^{-1} \sum_{p=-k+1}^{\left\lfloor \frac{N_C-k}{2} \right\rfloor} |c_p + c_{p+k}|^2 + \\ & + \sum_{k=-(N_C-1)}^{-1} \sum_{p=-\left\lfloor \frac{N_C+k}{2} \right\rfloor}^{-1} |c_p + c_{p+k}|^2 \\ & + \sum_{p=1}^{N_C} \sum_{q=1}^{N_C} |c_p + c_q|^2 \\ & - \sum_{p=1}^{N_C} |c_p + c_{-p}|^2 \end{aligned} \tag{1.111}$$

Using these results in equation (1.108), where equation (1.75) is used for c_q and the definitions (1.34) and (1.55) for the filters $H_x(\Omega)$ it is possible to calculate

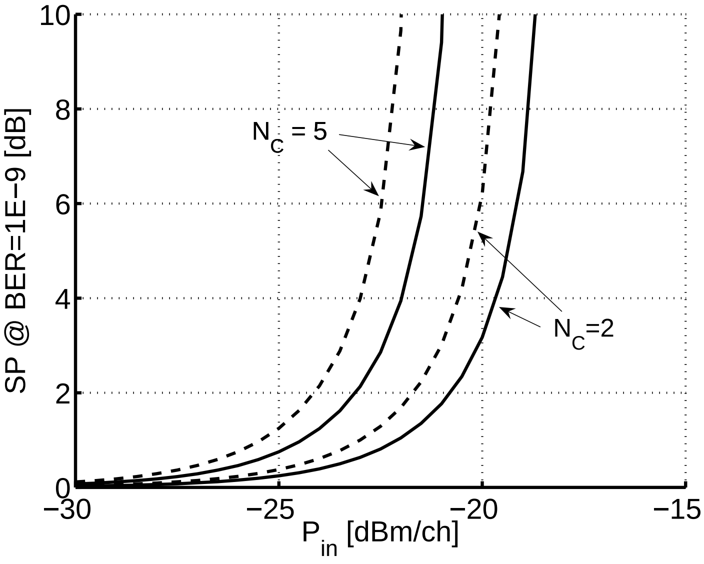

Figure 1.6: SP versus input power per channel. Dashed curves are calculated with synchronous patterns while solid curves refer to asynchrounous patterns. The two curves on the right-hand side are calculated with $N_C = 2$, while the ones on the left with $N_C = 5$.

the variance σ_{FWM}. When we have this FWM variance it is possible, using equation (2) in [30] to calculate the sensitivity penalty

$$\mathrm{SP} = -20\log_{10}\left[\frac{\sqrt{er}}{\sqrt{er}-1}\sqrt{1-\frac{er}{er-1}\sigma^2_{FWM}Q^2}-\frac{1}{\sqrt{er}-1}\right] \qquad (1.112)$$

In this equation, Q is the value of the Q-factor where the penalty is calculated; i.e. it is $Q = 6$ for an error rate of 10^{-9}; er is the *extinction ratio* of the Mach-Zehnder modulator.

Numerical results

In order to verify the impact of FWM we tested the equations derived in the previous section using the same parameters set adopted by [7] that are also reported in table 1.2.

Parameter	Value	Parameter	Value	Parameter	Value
$g_{CH} \equiv g_0$	$115\ cm^{-1}$	$\varepsilon_{SHB} P_S$	0.1	τ_S	$250\ ps$
α	$10\ cm^{-1}$	$\varepsilon_{CH} P_S$	0.025	τ_{SHB}	$750\ fs$
L	$500\ \mu m$	β	4	τ_{CH}	$150\ fs$
P_S	$10\ mW$	β_{CH}	2	Γ	0.2

Table 1.2: Parameters used for the numerical results of this section.

The first test, reported in Fig. 1.6, shows the impact of the number of channels on the SP when the channel spacing is $\Delta f = 100$ GHz. The curves represent the SP versus the input power per channel: the solid curves are calculated with the values for the η constants for the asynchronous bit patterns while the dashed curves for the synchronous case. In this figure there are two pairs of curves, the two curves on the right are results with $N_C = 2$, while the two on the left for $N_C = 5$. There is a difference of 4 dB in total input power and a difference of 3 dB of penalty so we can state that for a given saturation it is better to have more channels. Moreover, synchronous bits are a worst case for FWM, as was already clear from the value of the η parameters.

Since we control the equations of FWM variance we can choose to turn-on just one mechanism at a time. In Fig. 1.7 there are the curves for all the FWM mechanisms taken one at a time. These curves represent the FWM variance when only that particular mechanism is enabled. The solid line represents the variance given by the three mechanism all together. It's interesting to see that the total variance is different from the sum of the single variances.

1.4 Reservoir Filter

The reservoir dynamic equation for SOA (1.15) is a nonlinear equation. In the small signal approximation, this equation can be linearised and it will be possible to evaluate the impact of a small perturbation of the input fluxes on the reservoir. In fact working at small signals means that the quantities involved in the equation will be considered as the sum of a steady-state value, which biases the amplifier, and an additive small perturbation. In this kind of analysis the perturbation is so small that all the nonlinear functions will be approximated with the first term of their Taylor series. The reservoir can be written as $r(t) = r_{SS} + \Delta r(t)$ and the j-th input photon flux $Q_j(t) = \bar{Q_j} + \Delta Q_j(t)$, where r_{SS} and $\bar{Q_j}$ are the steady-state time invariant terms. If

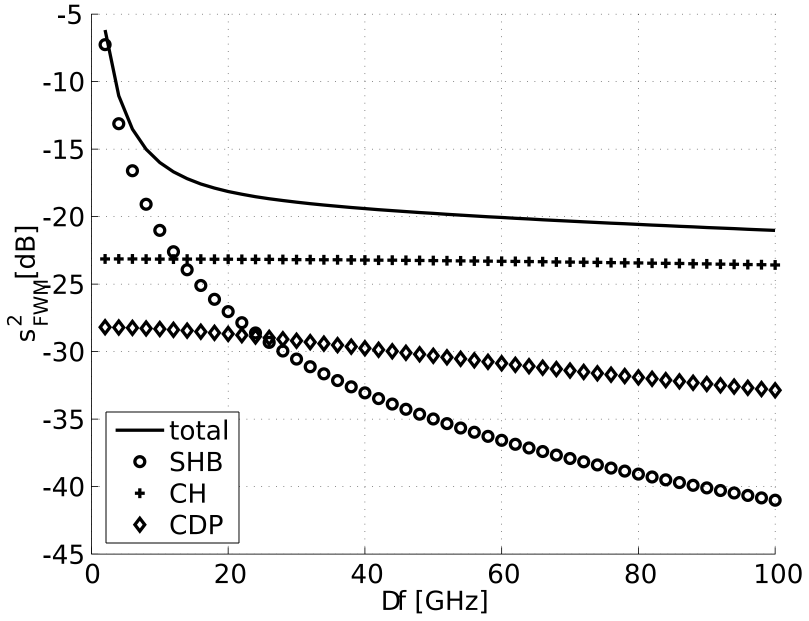

Figure 1.7: Variance of the single mechanisms involved in FWM generation: CH, SHB e CDP (markers); solid line represents the total variance of FWM. P_{IN} = -20 dBm, synchronous channels, 100 GHz spacing.

we define:

$$G_{j,SS} \triangleq B_j r_{SS} - A_j \tag{1.113}$$

and if we use the following approximation

$$\frac{1}{1+x} \simeq 1 - x \tag{1.114}$$

which is valid if $x \ll 1$ then we can write:

$$\frac{G_j(r)}{G_j(r) - \alpha L} = \frac{G_{j,SS}}{G_{j,SS} - \alpha L}\left(\frac{1 + (\frac{B_j}{G_{j,SS}})\Delta r}{1 + (\frac{B_j}{G_{j,SS}-\alpha L})\Delta r}\right) \tag{1.115}$$

and

$$\begin{aligned}
\frac{G_j(r)}{G_j(r)-\alpha L} &\simeq \frac{G_{j,SS}}{G_{j,SS}-\alpha L}[1+(\frac{B_j}{G_{j,SS}}-\frac{B_j}{G_{j,SS}-\alpha L})\Delta r] \\
&= \frac{G_{j,SS}}{G_{j,SS}-\alpha L}[1+\frac{B_j}{G_{j,SS}}(1-\frac{1}{1-\frac{\alpha L}{G_{j,SS}}})\Delta r] \\
&= \frac{G_{j,SS}}{G_{j,SS}-\alpha L}[1-\frac{\alpha L}{(G_{j,SS}-\alpha L)}\frac{B_j\Delta r}{G_{j,SS}}] \\
&= M_{1,j}[1-M_{2,j}B_j\Delta r] \qquad (1.116)
\end{aligned}$$

where we used the parameters

$$\begin{cases} M_{1,j}=\frac{G_{j,SS}}{G_{j,SS}-\alpha L} \\ M_{2,j}=\frac{\alpha L}{(G_{j,SS}-\alpha L)G_{j,SS}} \end{cases}. \qquad (1.117)$$

The approximation

$$e^x \simeq 1+x$$

valid if $x \rightarrow 0$ yields to the following equation:

$$(e^{G_j(r)-\alpha L}-1) \simeq K_{j,SS}(1+B_j\Delta r)-1=(K_{j,SS}-1)+K_{j,SS}B_j\Delta r \qquad (1.118)$$

where we used the new parameter

$$K_{j,SS} \triangleq e^{B_j r_{SS}-A_j-\alpha L} \qquad (1.119)$$

which is the net gain of the j-th signal.

From equations (1.116) and (1.118), the reservoir equation (1.15) becomes:

$$\begin{aligned}
\dot{\Delta r} = -\frac{r}{\tau_r}+\frac{I}{q}-\sum_{j\in S}\{M_{1,j}[1-M_{2,j}B_j\Delta r][(K_{j,SS}-1) \\
+K_{j,SS}B_j\Delta r](\bar{Q}_j+\Delta Q)\}. \qquad (1.120)
\end{aligned}$$

At steady-state all temporal derivatives are zero so $\frac{r_{SS}}{\tau_r}$ can be calculated as:

$$\frac{r_{SS}}{\tau_r}=\frac{I}{q}-\sum_{j\in S}M_{1,j}(K_{j,SS}-1)\bar{Q}_j. \qquad (1.121)$$

Using equation (1.121) in (1.15) and neglecting second order terms we have:

$$\dot{\Delta r} = -\left\{ \frac{1}{\tau_r} + \sum_{j\in S}(M_{1,j}B_j\bar{Q}_jK_{j,SS}[1-(1-\frac{1}{K_{j,SS}})M_{2,j}) \right\} \\ \Delta r + \sum_{j\in S} M_{1,j}(1-K_{j,SS})\Delta Q_j. \tag{1.122}$$

The Laplace transform function of this last equation is:

$$s\Delta R(s) = -\left\{ \frac{1}{\tau_r} + \sum_{j\in S}(M_{1,j}B_j\bar{Q}_jK_{j,SS}[1-(1-\frac{1}{K_{j,SS}})M_{2,j}) \right\} \Delta R(s) \\ + \sum_{j\in S} M_{1,j}(1-K_{j,SS})\Delta Q_j(s) \tag{1.123}$$

which becomes:

$$(s+\frac{1}{\tau_0})\Delta R(s) = \sum_{j\in S} M_{1,j}(1-K_{j,SS})\Delta Q_j(s) \tag{1.124}$$

where:

$$\begin{aligned} \frac{1}{\tau_0} &\triangleq \frac{1}{\tau_r} + \sum_{j\in S}\left\{ M_{1,j}B_j\bar{Q}_jK_{j,SS}\left[1-\left(1-\frac{1}{K_{j,SS}}\right)M_{2,j}\right]\right\} \\ &= \frac{1}{\tau_r} + \sum_{j\in S}\left\{ B_j\bar{Q}_jK_{j,SS}\left(\frac{G_{j,SS}}{G_{j,SS}-\alpha L}\right)\right. \\ &\quad \left.\left[1-\left(1-\frac{1}{K_{j,SS}}\right)\frac{\alpha L}{(G_{j,SS}-\alpha L)G_{j,SS}}\right]\right\}. \end{aligned} \tag{1.125}$$

Trying to put this equation in form of a linear filter we write:

$$\Delta R(s) = H_0(s)K(s) \tag{1.126}$$

where

$$K(s) \triangleq \sum_{j\in S} M_{1,j}(1-K_{j,SS})\Delta Q_j(s) \tag{1.127}$$

depends on time fluctuation of input and gain flux and

$$H_0(s) \triangleq \frac{1}{(s + \frac{1}{\tau_0})} \tag{1.128}$$

is the transfer function of a band-pass filter with bandwith $B_0 = \frac{1}{\tau_0}$ and CW intensity of τ_0. The fact that the reservoir filter is a low-pass filter was already known but now we have proposed an expression for the reservoir filter for SOA. It's very interesting to notice which components are responsible for the value of τ_0. The bandwith of this filter is the most important parameter in an amplifier. All the perturbations outside this bandwith cannot interact with the reservoir, this means that they cannot produce gain modulation distortions.

1.5 Conclusions

A novel state-variable SOA model, amenable to block diagram implementation for WDM applications, and with fast execution times was presented and discussed. A critical step in the SOA reservoir model is the appropriate selection of the values of its wavelength dependent parameters that provide good fit with experiments. These parameters can be extracted from the accurate gain profile given by Connelly but this is not a universally valid method. Many new SOAs are realised with advanced technologies that make their gain profile much more complicated. In this case it should be better to look for an experimental method that enables the user to extract the best matching gain paramenters for the reservoir model instead of looking for a gain profile that is pretty unobtainable. Beating-induced carrier gratings that generate FWM and XPM in SOAs are not captured by the reservoir model, but thanks to the study of the model proposed by Mecozzi we added such effects and all the ultrafast FWM mechanisms due to intraband dynamics. We can state that the reservoir model is now complete with all the most important features required by a WDM optical simulator, but further detailed experimental investigations would be required to validate this model. The true value of the SOA reservoir model is that, together with block diagram descriptions of EDFA and Raman amplifiers, it provides a unique tool with reasonably short computation times for a reliable analysis of gain transients in WDM optical networks with complex topologies.

Appendix A

This appendix explains in detail the solution of the integral (1.91). In order to solve it, the definition of k_q, given in equation (1.62), should be written as:

$$\begin{aligned} k_q(S) = \frac{[g_{CH}(1-i\beta_{CH})\varepsilon_{CH}H_{CH}(q\Omega))]}{2} &+ \\ \frac{\varepsilon_{SH}H_{SH}(q\Omega)}{2}\frac{g_0}{1+\frac{\overline{P}}{P_S}} &+ \\ \frac{1-i\beta}{2P_S}\frac{g_0}{1+\overline{P}/P_S}\frac{1}{1+\overline{P}/P_S-iq\Omega\tau_s} & \end{aligned} \tag{A.1}$$

where three terms that depends on $\overline{P}$ are more clearly separated. The three terms, whose integrals need to be solved, are:

$$\begin{aligned} &1)\quad F_1 = \int_0^L G(z)dz \\ &2)\quad F_2 = \int_0^L G(z)\tfrac{g_0}{1+\overline{P}/P_S}dz \\ &3)\quad F_3 = \int_0^L G(z)\tfrac{g_0}{1+\overline{P}/P_S}\tfrac{1}{1+\overline{P}/P_S-iq\Omega\tau_s}dz \end{aligned} \tag{A.2}$$

where $G(z) = P(z)/P(0)$.

These three integrals can be solved thanks to the following rule:

$$F = \int_0^L f(P(z'))dz' = \int_{\overline{P}_0}^{\overline{P}(z)} f(s)\left(\frac{ds}{dz}\right)^{-1} ds \tag{A.3}$$

where $\overline{P}_0 = \overline{P}(0)$. Equation (1.80) contains the expression for $\frac{ds}{dz}$ which is needed to solve the integral. Moreover, equation (1.80) can be manipulated in order to obtain a second relation which is needed to solve the integrals of (A.2). In fact, (1.80) can be written as

$$\frac{(1+\overline{P}/P_S)d\overline{P}}{1-\frac{\alpha}{g_0}(1+\overline{P}/P_S)} = g_0\overline{P}(z)dz \tag{A.4}$$

and by the integration of both sides, one gets:

$$\frac{\alpha}{g_0}\ln\left(\frac{1-\frac{\alpha}{g_0-\alpha}\frac{\overline{P}_0}{P_S}}{1-\frac{\alpha}{g_0-\alpha}\frac{\overline{P}(L)}{P_S}}\right) = \ln\frac{G_0}{G(L)}. \tag{A.5}$$

The first equation in (A.2) is solved as:

$$\begin{aligned}
F_1 = \int_0^L G(z)dz &\overset{(A.3)}{=} \\
P_S \int_{\overline{P}_0}^{\overline{P}(L)} \frac{\frac{1}{\overline{P}_0}\frac{d\overline{P}}{P_S}}{-\alpha + \frac{g_0}{1+\overline{P}/P_S}} &= \frac{P_S}{\overline{P}_0} \int_{\overline{P}_0/P_S}^{\overline{P}(L)/P_S} \frac{1+x}{-\alpha x + g_0 - \alpha} dx = \\
&= \frac{1}{\frac{\overline{P}_0}{P_S}(g_0-\alpha)} \int_{\overline{P}_0/P_S=C_0}^{\overline{P}(L)/P_S=C_1} \frac{1+x}{1-(\frac{\alpha}{g_0-\alpha})x} dx \overset{(A.5)}{=} \\
&= \frac{P_S}{\alpha\overline{P}_0}\left[\ln\frac{G_0}{G} - (G-1)\frac{\overline{P}_0}{P_S}\right] \qquad \text{(A.6)}
\end{aligned}$$

where $G = G(L)$ and (A.5) is used for the last relation.

Similarly, the solution for the second equation in (A.2) is derived as:

$$\begin{aligned}
F_2 = \int_0^L G(z)\frac{g_0}{1+\overline{P}/P_S}dz &\overset{(A.3)}{=} \\
= P_S \int_{\overline{P}_0/P_S=C_0}^{\overline{P}(L)/P_S=C_1} \frac{\frac{g_0}{\overline{P}_0(1+\overline{P}/P_S)}\frac{d\overline{P}}{P_S}}{-\alpha + \frac{g_0}{1+\overline{P}/P_S}} &= g_0\frac{P_S}{\overline{P}_0} \int_{C_0}^{C_1} \frac{dx}{g_0 - \alpha - \alpha x} = \\
= \frac{P_S}{\overline{P}_0}\frac{g_0}{g_0-\alpha} \int_{C_0}^{C_1} \frac{dx}{1-(\frac{\alpha}{g_0-\alpha})x} &\overset{(A.5)}{=} \frac{P_S}{\overline{P}_0}\ln\frac{G_0}{G} \qquad \text{(A.7)}
\end{aligned}$$

Finally, the solution of the third equation in (A.2) is

$$
\begin{aligned}
F_3 = \int_0^L G(z)\frac{g_0}{1+\overline{P}/P_S}\,\frac{1}{1+\overline{P}/P_S-iq\Omega\tau_s}dz &\overset{(A.3)}{=} \\
= P_S\int_{\overline{P}_0/P_S=C_0}^{\overline{P}(L)/P_S=C_1}\frac{g_0\,d\overline{P}/P_S}{\overline{P}_0(1+\overline{P}/P_S)(1+\overline{P}/P_S-iq\Omega\tau_s)(\frac{g_0}{1+\overline{P}/P_S}-\alpha)} &= \\
= \frac{g_0}{\frac{\overline{P}_0}{P_S}}\int_{C_0}^{C_1}\frac{dx}{x+(1-iq\Omega\tau_s)(g_0-\alpha-\alpha x)} &= \\
= \frac{P_S}{\overline{P}_0}\frac{g_0}{g_0-\alpha}\int_{C_0}^{C_1}\frac{dx}{\Big[x+(1-iq\Omega\tau_s)\Big]\Big[1-\left(\frac{\alpha}{g_0-\alpha}\right)x\Big]} &\overset{(A.5)}{=} \\
= \frac{P_S}{\overline{P}_0}\frac{1}{1-iq\Omega\tau_s\frac{\alpha}{g_0}}\left[\ln\left(\frac{1+\frac{\overline{P}_0}{P_S}G-iq\Omega\tau_s}{1+\frac{\overline{P}_0}{P_S}-iq\Omega\tau_s}\right)+\frac{\alpha}{g_0}\ln\frac{G_0}{G}\right] & \qquad (A.8)
\end{aligned}
$$

The three solutions (A.6), (A.7), and (A.8) can be used in the integral (1.91) to obtain the final solution:

$$
\begin{aligned}
c_q = \frac{1-i\beta}{2\overline{P}}\left\{\frac{1}{1-iq\Omega\tau_s\xi}\left[\ln\left(\frac{1+\overline{P}/P_S G_L-iq\Omega\tau_s}{1+\overline{P}/P_S-iq\Omega\tau_s}\right)+\xi\ln\frac{G_0}{G_L}\right]\right\}&+ \\
\frac{P_S\varepsilon_{SH}H_{SH}(q\Omega)}{2\overline{P}}\ln\frac{G_0}{G_L}&+ \\
g_{CH}\frac{1-i\beta_{CH}}{2}\frac{P_S\varepsilon_{CH}H_{CH}(q\Omega)}{\overline{P}}\frac{1}{g_0\xi}\left[\ln\frac{G_0}{G_L}-(G_L-1)\frac{\overline{P}}{P_S}\right] & \qquad (A.9)
\end{aligned}
$$

where $\overline{P}\equiv\overline{P}_0$, $\ln G_0=(g_0-\alpha)L$ is the non-saturated gain, and $\xi=\alpha/g_0$.

Chapter 2

Gain Clamped SOA

Amplifier gain is in general a nonlinear function of input power. This is true for optical and electrical amplifiers. This function, which is represented in the so called "saturation curve", is very important in the design of an optical link. It shows that the function of gain versus input power is nonlinear and there is a threshold value, called saturation input power, after which the gain decreases or, equivalently, the output power saturates to its maximum value. The presence of this threshold value divides the functioning range of the amplifier into two regions. The first region, where the gain is more or less constant with respect to the input power, is called the linear region. For input powers higher than the threshold, we can say that the amplifier works in saturation. In the first region the output power is a linear function of the input power while in the second region the output power has reached its maximum value and the gain is a decreasing function of the input power.

When time variations are involved, gain dynamics become more complex and the saturation curve is not sufficient to describe them. As we saw in section 1.2, optical amplifiers present a finite response time and they have a given impulse response. Since generally power varies in time, the optical amplifiers react to this variation. To better understand the nature of this reaction, power variations should be divided into two categories: slow and fast variations. Slow with respect to what? The reference time constant, as shown by the results of section 1.4, is mainly due to the carrier lifetime of the optical amplifier. If power varies faster than the carrier lifetime then the *reservoir* of the amplifier is not able to follow these variations and the bias point in the gain vs. input power saturation characteristic is determined by the mean value of the input power. On the contrary, if power variations are slower than the carrier lifetime then they affect the reservoir: the output power is deformed (since the *reservoir* filter is a lowpass filter, see section 1.4) and the bias point on the gain versus input power saturation characteristic moves, following the power variation. This approach is simplifying the real physics of the optical amplifiers but is a quick way to foresee the results. In particular, if we consider that the values for the carrier lifetime for EDFA and SOA are:

$$\begin{cases} \tau_e \simeq 1\ ms & \text{for EDFA} \\ \tau_s \simeq 0.1\ ns & \text{for SOA} \end{cases}$$

then it is evident that any optical amplitude modulation with a symbol rate higher than 1 Gbit/s is a fast variation for an EDFA; while add/drop of channels in a WDM transmission is slow for both EDFA and SOA. In a WDM transmission system every "slow" variation represents a problem since pulses are deformed by the response of the *reservoir* filter and the gain of the amplifier changes. When slow variations cannot be avoided, a mechanism to stabilise the gain of the amplifiers should be implemented. These mechanisms could be electronic aided or all-optical. In this chapter we will discuss only all-optical gain stabilisation technique, also known as gain-calmping structures.

The first proposal of gain-clamping, for an EDFA, has been done by Zirngibl of Bell Labs [31]; his aim was to design an amplifier robust against add and drop of channels thanks to an optical feedback. This technique requires to introduce more optical components in the already complex EDFA manufacturing procedure. SOAs are different: they are integrated devices. And the technology that produces SOAs does not need great improvements to write gratings in the SOA waveguide. In this way a gain-clamped SOA (GC-SOA) would require a very little cost increase. GC-SOA have been proposed in [32] for crosstalk reduction in WDM transmission. Using the detailed model for GC-SOA proposed in [23], Wolfson *et al.* [33] showed that gain-clamping can extend the linear range of an amplifier by 8 dB but this extension is not exploitable because of relaxation oscillations of the clamping laser. This oscillations cause a dynamic extinction ratio degradation that reduces the linear range extension to 0.5 dB. Another typical variation of input power can be due to optical packets. A network with optical packets [34, 35] has a bursty traffic that presents problems for the amplifiers. Packets are not a periodic perturbation; since their number is random the amplifier input power varies with different speeds: from the fastest, the symbol rate, passing through the packet rate, down to the changes in the mean traffic during the day. With this kind of traffic it is important to work in the linear region (or almost in the linear region) of an amplifier and it is also important that the impulse response of the amplifier does not affect the shape of the packets. When a packet goes through an amplifier the number of bits subject to the transient can be estimated by looking at the carrier life time. With a symbol rate of 10 Gbit/s, in an EDFA the first 10 million bits could be affected by the transient while in an SOA only the first bit of the packet could be affected. Since this dynamic response implies a large penalty on the transmission, gain-clamping is the only way to implement an optical packet network using EDFA. On the contrary, SOA could be used, if the problem of gain stabilisation is not critical. In fact SOA without gain clamping have a gain that depends on the actual number of packets being injected in the amplifier. In this chapter, through experimental and theoretical results it will be discussed if gain-clamping can be an enhancing technique in optical networks with bursty traffic.

A new SOA has recently been introduced [36] that achieves gain-stabilisation through a series of internal vertical clamping laser cavities. Linear operation is thus guaranteed for a wide range of input powers, hence the name Linear Optical Amplifier (LOA) [36]. LOAs have been tested against add-drop of channels and compared to standard EDFA showing good performance [37]. They also have been tested in a WDM metropolitan area network (MAN) environment where up to 8 LOAs have been cascaded with an error-free result [38]. Although LOA simulations have been performed by solving the detailed equations that govern the signal-amplifier interactions [39, 40], it would be highly desirable to have simple analytical and simulation tools able to quickly model LOAs in the design and analysis of an optical link. The numerical model presented for the SOA will be extended to the LOA and it will be validated against experimental results.

This chapter is organised as follows.

In section 2.1 a reservoir model for LOA will be proposed. It will be derived in a way similar to the reservoir model for SOA with multiple cavities [24].

In section 2.2 this model will be verified against some experimental results.

In section 2.3 the linear filters for the state variables involved in this model will be derived.

In section 2.4 an experimental comparison involving three different kinds of SOAs verify which is the most suitable technology for the specific case of: a WDM metropolitan network based on optical packets.

2.1 A model for SOA clamped by a vertical laser field

LOAs achieve gain stabilisation thanks to a series of internal vertical lasing cavities that clamp the carrier density along the device. A numerical analysis of signals propagation in a LOA requires the joint solution of a set of differential equations [40] representing: signals propagation, the time adaptation of the vertical lasers, and the amplifier rate equation, describing the time evolution of the carrier density profile. In an SOA, the rate equation can be integrated along the SOA length, by properly accounting for the amplifier material gain, scattering loss, and the generation of ASE noise, thus reducing the analysis to the solution of a single differential equation describing the time evolution of a state variable: the reservoir $r(t)$. Once $r(t)$ is known, the input-output relationship is readily determined for every input signal. Since a LOA is made of multiple cavities, the integration of the rate equation is done in each cavity separately, resulting in a multi-slice amplifier, each containing a vertical clamping laser. The amplifier geometry has been modeled considering that the length L of the active region is divided in N_C independent cavities, each with a transverse area $A = wd$ and length $l = L/N_C$. Inside each cavity there is a laser oscillation along the vertical direction. The transverse area seen by these lasers is $A_L = wl$ and the length of their cavity is d_L. In general $d_L > d$ since the laser propagates through the gratings that are outside the active region.

This is the rate equation (see [40] eq. (1)):

$$\frac{\partial N(z,t)}{\partial t} = \frac{I}{eV} - R\left(N(z,t)\right) - \frac{\Gamma}{A}\sum_{j\in S} g_m(N(z,t),\nu_j)Q_j(z,t) - \frac{\Gamma_L}{A_L}\left[g_m(N(z,t),\nu_L)Q_L(z,t)\right] \quad (2.1)$$

where ASE has been neglected and Γ_L and A_L are the overlap factor and the transverse area of the vertical lasers.

This is the general propagation equation (see [40] eq. (4)):

$$\frac{\partial Q_j(z,t)}{\partial z} + \frac{1}{v}\frac{\partial Q_j(z,t)}{\partial t} = \left[\Gamma g_m(N(z,t),\nu_j) - \alpha\right] Q_j(z,t) + R_{sp}(N(z,t),\nu) \quad (2.2)$$

and neglecting the time derivative, the simplified propagation equation is:

$$\frac{\partial Q_j(z,t)}{\partial z} = \left[\Gamma g_m(N(z,t),\nu_j) - \alpha\right] Q(z,t) + R_{sp}(N(z,t),\nu). \quad (2.3)$$

With the same trick used in the previous section the propagation equation for the LOA can be written as:

$$\frac{\partial Q_k(z,t)}{\partial z} = \left\{\Gamma\sigma_k^g \left[N(z,t) - N_{0,k}\right] - \alpha\right\} Q_k(z,t). \tag{2.4}$$

The vertical laser does not propagate along the z direction. The laser flux varies in time and not in space so this equation is used to describe it:

$$\frac{1}{v}\frac{\partial Q_L(z,t)}{\partial t} = \Gamma_L \left[g_m(N(z,t),\nu_L) - g_{th}\right] Q_L(z,t) + R_{sp,L}(N(z,t)) \tag{2.5}$$

where $v = c/n$ is the group velocity. The absence of the variable z can be justified if the division in cavities is taken into account. This is the dynamic equation for the vertical laser fields:

$$\frac{\partial Q_L(t)}{\partial t} = v\Gamma_L \left[\sigma_L^g \left[N(z,t) - N_{0,L}\right] - g_{th}\right] Q_L(t) + R_{sp,L}(N(z,t)) \tag{2.6}$$

where g_{th} is the threshold gain. When the active medium gain is below this threshold then there is no vertical field. Considering that the reflective mirrors on the facet of the device have reflectivity R_L, we can write

$$g_{th} = \frac{1}{\Gamma_L}\left(\alpha - \frac{\ln R_L}{d_L}\right) \tag{2.7}$$

where the losses due to the reflectivity have been distributed along the propagation length d_L. By using (2.1), (2.4) and (2.6) and neglecting the term responsible for spontaneous emission R_{sp} then in the i-th cavity we have this relation:

$$\frac{\partial N(z,t)}{\partial t} = \frac{I^i}{eAl} - R\left(N(z,t)\right) - \frac{1}{A}\sum_{j\in S}\left[\frac{\partial Q_j(z,t)}{\partial z} + \alpha Q_j(z,t)\right] - \frac{\Gamma_L}{A_L}\left\{\sigma_L^g \left[N(z,t) - N_{0,L}\right] Q_L^i(t)\right\} \tag{2.8}$$

where the z variable goes from $(i-1)l$ to il (with $i = 1 \dots N_C$ and $l = L/N_C$), $I^i \equiv I/N_C$, and $Q_L^i(t)$ is the photon flux of this cavity. Making the same assumption as in [40], that the photon flux of the vertical laser does not vary in z inside a single cavity, we define the reservoir of the i-th cavity as:

$$r^i \triangleq A\int_{\frac{(i-1)L}{N_C}}^{\frac{iL}{N_C}} N(z,t)dz \tag{2.9}$$

and for the i-th cavity the reservoir dynamic equation is:

$$\frac{\partial r^i(t)}{\partial t} = \frac{I^i}{e} - R_r(r^i) - \sum_{j\in S}\left[Q_j^{in,i}(t)\left(\frac{G(r)}{G(r)-\alpha l}\right)\left(e^{B_j r^i(t)-A_j-\alpha l}-1\right)\right] - \frac{\Gamma_L A}{A_L\Gamma}\left\{B_L r^i(t)-A_L\right\}Q_L^i(t) \quad (2.10)$$

where, like for the traditional SOA model, by the integration of (2.4) the following equation can be obtained:

$$\int_{\frac{(i-1)L}{N_C}}^{\frac{iL}{N_C}}\frac{\partial Q_k}{Q_k} = \ln\frac{Q_k^{out,i}}{Q_k^{in,i}} = G_k^i(t)-\alpha l = \int_{\frac{(i-1)L}{N_C}}^{\frac{iL}{N_C}}\left\{\Gamma\sigma_k^g\left[N(z,t)-N_{0,k}\right]-\alpha\right\} = \\ = B_k r^i(t) - A_k - \alpha l \quad (2.11)$$

where

$$\begin{cases} A_k = \Gamma\sigma_k^g N_{0,k} l = -\Gamma p^0 l \\ B_k = \frac{\Gamma}{A}\sigma_k^g \end{cases} . \quad (2.12)$$

For each cavity we consider the presence of signals and amplified spontaneous emission (ASE) wavelengths, propagating in the forward direction only. The photon flux Q_i^L of the $i-th$ clamping laser is independent of z.

The gain constants A_k e B_k depend only on the signals wavelength and do not depend on the cavity index when the active region is divided in uniform cavities.

Defining:

$$G_j^{net}(r) = B_j r^i(t) - A_j - \alpha l \quad (2.13)$$

and

$$\begin{cases} C_L = \frac{A}{A_L}\Gamma_L\sigma_k^g N_{0,k} l = \Gamma_L\sigma_k^g N_{0,k} d = -\Gamma_L p^0 d \\ D_L = \frac{\Gamma_L}{A_L}\sigma_k^g \end{cases} \quad (2.14)$$

eq. (2.10) can be written as:

$$\dot{r}^i = \frac{I^i}{e} - \frac{r^i}{\tau} - \sum_{j\in S}\left[Q_j^{in,i}(t)\frac{G_j(r)}{G_j^{net}(r)}\left(e^{G_j^{net}(r^i)}-1\right)\right] - G_L(r^i)Q_L^i(t) \quad (2.15)$$

where

$$G_L(r^i) = \frac{\Gamma_L A}{A_L\Gamma}\left\{B_L r^i(t) - A_L\right\} = C_L r^i(t) - D_L. \quad (2.16)$$

Eq. (2.15) is the main result of this section but now this equation is not sufficient to describe the behaviour of a LOA. Since LOAs have two state variables for each cavity, there is the need to calculate another differential equation that will be coupled to this one. If in eq. (2.6) the carrier density is considered constant on the whole cavity, $N(z,t) = \bar{N} = \frac{1}{l}\int_{[l]} N(z,t)dz$, then $N(z,t) = r^i/Al$ and the equation we need is:

$$\frac{\partial Q_L^i(t)}{\partial t} = v\Gamma_L \left\{ \sigma_L^g \left[\frac{r^i}{Al} - N_{0,L}^i \right] - g_{th} \right\} Q_L^i(t) + vR_{sp,L}\left(\frac{r^i}{Al}\right) \tag{2.17}$$

which is best expressed with this notation:

$$\frac{\partial Q_L^i(t)}{\partial t} = \frac{v}{d}\left\{ D_L r^i - C_L - d\Gamma_L g_{th} \right\} Q_L^i(t) + vR_{sp,L}\left(\frac{r^i}{Al}\right). \tag{2.18}$$

The equations (2.15) and (2.18) are the two equations that are needed to model a single LOA cavity. The whole device is described by $2N_C$ differential equations and by these relations:

$$Q_k^{in,0} = Q_k^{in}; \qquad Q_k^{in,i+1} = Q_k^{in,i} e^{G_k^i - \alpha l} \tag{2.19}$$

where α represents the scattering losses.

At steady-state, which means that the time varying quantities are zero, the reservoir equation becomes:

$$r_{SS}^i = \tau \left\{ \frac{I^i}{e} + \sum_{j\in S} \frac{G_j(r_{SS})}{G_j^{net}(r_{SS})} \left(e^{G_j^{net}(r_{SS}^i)} - 1 \right) Q_{j,SS}^{in,i} - G_L(r_{SS}^i) Q_{L,SS}^i \right\} \tag{2.20}$$

while eq. (2.18) can be zero, neglecting the spontaneous emission term, just in two cases:

$$\begin{cases} D_L r_{SS}^i - C_L = d\Gamma_L g_{th} & \text{VCL ON} \\ Q_{L,SS}^i = 0 & \text{VCL OFF} \end{cases} \tag{2.21}$$

In the “VCL OFF” case, the LOA becomes a traditional SOA:

$$r_{SS}^i = \tau \left\{ \frac{I^i}{e} + \sum_{j\in S} \frac{G_j(r_{SS})}{G_j^{net}(r_{SS})} \left(e^{G_j^{net}(r_{SS}^i)} - 1 \right) Q_{j,SS}^{in,i} \right\} \tag{2.22}$$

while in the “VCL ON” case the LOA steady-state equation becomes:

$$G_L(r_{SS}^i) = D_L r_{SS}^i - C_L = d\Gamma_L g_{th} = d\left(\alpha - \frac{\ln R_L}{d_L}\right) \tag{2.23}$$

from which this relation can be easily obtained:

$$r_{SS}^i = \frac{d\left(\alpha - \frac{\ln R_L}{d_L}\right) + C_L}{D_L} = \frac{d\Gamma_L g_{th} + C_L}{D_L}. \tag{2.24}$$

2.1.1 Model extended with ASE

Spontaneous emission can be included in the reservoir model for the LOA in the same way it was included in the model for SOA. By dividing the optical band into discrete frequencies it is possible to associate an ASE virtual channel to each discrete frequency. To take into account the spontaneous emission the rate-equation becomes:

$$\frac{\partial N(z,t)}{\partial t} = \frac{I}{eV} - \frac{N}{\tau} - \frac{\Gamma}{A}\sum_{j\in S} g_m(N(z,t),\nu_j)Q_j(z,t) - \\ \frac{\Gamma_L}{A_L}\left[g_m(N(z,t),\nu_L)Q_L(z,t)\right] - \frac{\Gamma}{A}\sum_{j\in ASE} g_m(N(z,t),\nu_j)Q_j^{ASE}(z,t) \tag{2.25}$$

while the propagation equation is still:

$$\frac{\partial Q_k(z,t)}{\partial z} = \left\{\Gamma\sigma_k^g\left[N(z,t) - N_{0,k}\right] - \alpha\right\} Q_k(z,t). \tag{2.26}$$

The channels of ASE follow this equation:

$$\frac{\partial Q_k^{ASE}(z,t)}{\partial z} = \left\{\Gamma\sigma_k^g\left[N(z,t) - N_{0,k}\right] - \alpha\right\} Q_k^{ASE}(z,t) + R_{sp,k}\left(N(z,t)\right) \tag{2.27}$$

And the vertical laser fields equation becomes:

$$\frac{1}{v}\frac{\partial Q_L(z,t)}{\partial t} = \Gamma_L\left[g_m(N(z,t),\nu_L) - g_{th}\right] Q_L(z,t) + R_{sp,L}(N(z,t)) \tag{2.28}$$

From eq. (2.27), considering an initial condition $Q(0) = 0$ we obtain:

$$Q_k^{ASE}(z) = e^{\int_{[l]}\left\{\Gamma\sigma_k^g\left[N(z',t)-N_{0,k}\right]-\alpha\right\}dz'} \\ \int_{[l]} \frac{R_{sp,k}(N(s))}{e^{\int_{[l]}\left\{\Gamma\sigma_k^g\left[N(z',t)-N_{0,k}\right]-\alpha\right\}dz'}}ds \tag{2.29}$$

If the approximation of constant carrier density holds, $N(z) \equiv \bar{N} = r^i/(Al)$, we can write:

$$Q_k^{ASE}(z) \simeq \frac{R_{sp,j}(\bar{N})}{\Gamma\sigma_k^g\left(\bar{N} - N_{0,k}\right) - \alpha}\left(e^{\left[\Gamma\sigma_k^g\left(\bar{N}-N_{0,k}\right)-\alpha\right]z} - 1\right). \tag{2.30}$$

To obtain the reservoir equation with ASE it is necessary to integrate along the z variable eq. (2.25):

$$\begin{aligned}&4\int_{\frac{(i-1)L}{N_C}}^{\frac{iL}{N_C}} \Gamma\sigma_k^g\left[N(z',t) - N_{0,k}\right] Q_k^{ASE}(z)dz = \\ &\quad 4\int_{\frac{(i-1)L}{N_C}}^{\frac{iL}{N_C}} R_{sp,j}(\bar{N})\frac{\Gamma\sigma_k^g\left[N(z',t) - N_{0,k}\right]}{\Gamma\sigma_k^g\left[\bar{N} - N_{0,k}\right] - \alpha}\left(e^{\left[\Gamma\sigma_k^g\left(\bar{N}-N_{0,k}\right)-\alpha\right]z} - 1\right)dz\end{aligned} \tag{2.31}$$

which can be simplified as:

$$\begin{aligned}&4R_{sp,j}(\bar{N})\frac{\Gamma\sigma_k^g\left[\bar{N} - N_{0,k}\right]}{\Gamma\sigma_k^g\left[\bar{N} - N_{0,k}\right] - \alpha}\int_{\frac{(i-1)L}{N_C}}^{\frac{iL}{N_C}}\left(e^{\left\{\Gamma\sigma_k^g\left[\bar{N}-N_{0,k}\right]-\alpha\right\}z} - 1\right)dz = \\ &\quad 4R_{sp,j}(\bar{N})\left[\frac{\sigma_k^g\left(\bar{N} - N_{0,k}\right)}{\sigma_k^g\left(\bar{N} - N_{0,k}\right) - \frac{\alpha}{\Gamma}}\right] \\ &\quad \frac{e^{\left\{\Gamma\sigma_k^g\left[\bar{N}-N_{0,k}\right]-\alpha\right\}\frac{L}{N_C}} - 1 - \left\{\Gamma\sigma_k^g\left[\bar{N} - N_{0,k}\right] - \alpha\right\}\frac{L}{N_C}}{\left\{\Gamma\sigma_k^g\left[\bar{N} - N_{0,k}\right] - \alpha\right\}}.\end{aligned} \tag{2.32}$$

From equation (2.12),

$$\Delta\nu\, n_{sp,k} = \frac{R_{sp,j}(\bar{N})}{\Gamma\sigma_k^g\left(\bar{N} - N_{0,k}\right) - \alpha} \tag{2.33}$$

and the uniformity of cavity lengths $l = L/N_C$ we write eq. (2.32) in this form:

$$4\Delta\nu\, n_{sp,k}^i\left[\frac{G_k(r^i)}{G_k(r^i) - \alpha l}\right]\left[e^{G_k(r^i)-\alpha l} - 1 - \left(G_k(r^i) - \alpha l\right)\right] \tag{2.34}$$

where $n_{sp,k}$ is the ratio between $g'(\nu, N)$ and the material gain coefficient $g_m(\nu, N)$:

$$n_{sp,k}(r^i) = \frac{g'(\nu, N)}{g_m(\nu, N)} = \frac{\Gamma\gamma_k^g\left(\bar{N} - N_{1,k}\right)}{\Gamma\sigma_k^g\left(\bar{N} - N_{0,k}\right)} = \frac{F_k r^i - E_k}{B_k r^i - A_k} \tag{2.35}$$

where $g'(\nu, N)$ has been linearised and we defined

$$\begin{cases} E_k = \Gamma \gamma_k^g N_{1,k} l \\ F_k = \frac{\Gamma}{A}\gamma_k^g \end{cases} . \tag{2.36}$$

The presence or absence of ASE term in the vertical laser field equation does not impact the equation for the reservoir:

$$\begin{aligned} \dot{r^i} = \frac{I^i}{e} - \frac{r^i}{\tau} - \sum_{j\in S,ASE} \left[Q_j^{in,i}(t) \frac{G_j(r)}{G_j^{net}(r)} \left(e^{G_j^{net}(r^i)} - 1 \right) \right] - G_L(r^i) Q_L^i(t) - \\ 4\Delta\nu \sum_{j\in ASE} n_{sp,k}(r^i) \frac{G_j(r^i)}{G_k^{net}(r^i)} \left[e^{G_k^{net}(r^i)} - 1 - G_k^{net}(r) \right] \end{aligned} \tag{2.37}$$

where $G^{net} = G - \alpha l$ and

$$G_L(r^i) = \frac{\Gamma_L A}{A_L \Gamma} \left[B_L r^i(t) - A_L \right] = C_L r^i(t) - D_L$$

where C and D are defined in eq. (2.14). The other differential equation becomes:

$$\frac{1}{v}\frac{\partial Q_L(z,t)}{\partial t} = \Gamma_L \left[g_m(N(z,t), \nu_L) - g_{th} \right] Q_L(z,t) + R_{sp,L}(N(z,t)) \tag{2.38}$$

and becomes with the substitution $\bar{N} = r/V$,

$$\begin{aligned} \frac{\partial Q_L(z,t)}{\partial t} &= v\Gamma_L \left[\sigma_L^g \left(\bar{N} - N_{0,L} \right) - g_{th} \right] Q_L(z,t) + \\ &\quad v\Delta\nu\, n_{sp,k} \left[\Gamma_L \sigma_L^g \left(\bar{N} - N_{0,L} \right) - \alpha \right] = \\ &= \left(\Gamma_L \sigma_L^g \frac{r^i}{wdl} - \Gamma_L \sigma_L^g N_{0,L} - \Gamma_L g_{th} \right) v Q_L(z,t) + \\ &\quad v \left(\Gamma_L \sigma_L^g \frac{r^i}{wdl} - \Gamma_L \sigma_L^g N_{0,L} - \alpha \right) \Delta\nu\, n_{sp,k} = \\ &= \frac{v}{d} \left(\Gamma_L \sigma_L^g \frac{r^i}{A_L} - d\Gamma_L \sigma_L^g N_{0,L} - d\Gamma_L g_{th} \right) Q_L(z,t) + \\ &\quad \frac{v}{d} \left(\Gamma_L \sigma_L^g \frac{r^i}{A_L} - d\Gamma_L \sigma_L^g N_{0,L} - \alpha d \right) \Delta\nu\, n_{sp,k} = \\ &\frac{v}{d} \left[\left(D_L r^i - C_L - d\Gamma_L g_{th} \right) Q_L(z,t) + \Delta\nu\, n_{sp,L} \left(D_L r^i - C_L - d\alpha \right) \right] . \end{aligned} \tag{2.39}$$

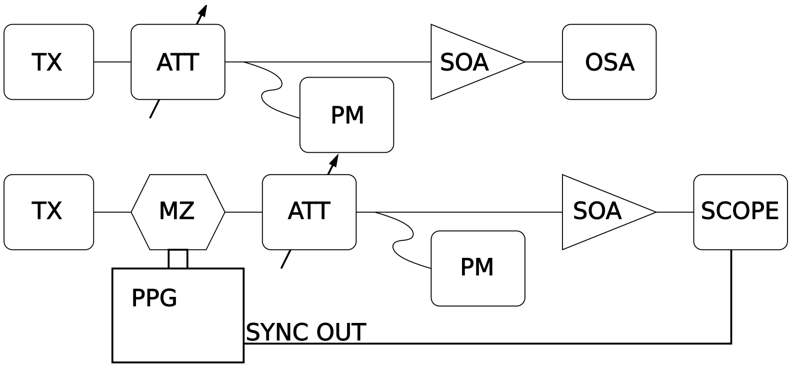

Figure 2.1: Upper diagram: setup for gain saturation measurments. Lower diagram: setup for step response using sampling scope. PM = power meter; OSA = optical spectrum analyzer; ATT = variable attenuator; TX = 1550.0 nm laser source; MZ = Mach-Zehnder modulator; PPG = pulse pattern generator.

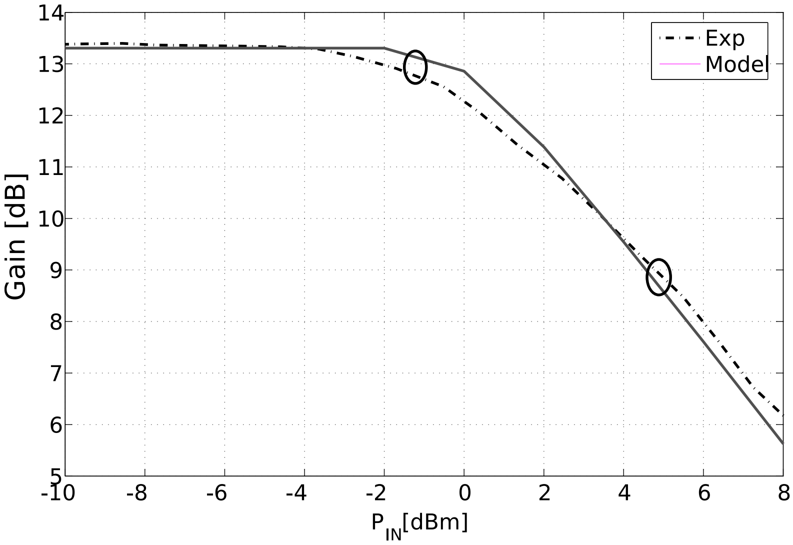

Figure 2.2: Gain saturation curve of an LOA. Experimental (dashed) and numerical (dashed) results. Circles refers to the working points of the next figures. LOA current I=250 mA.

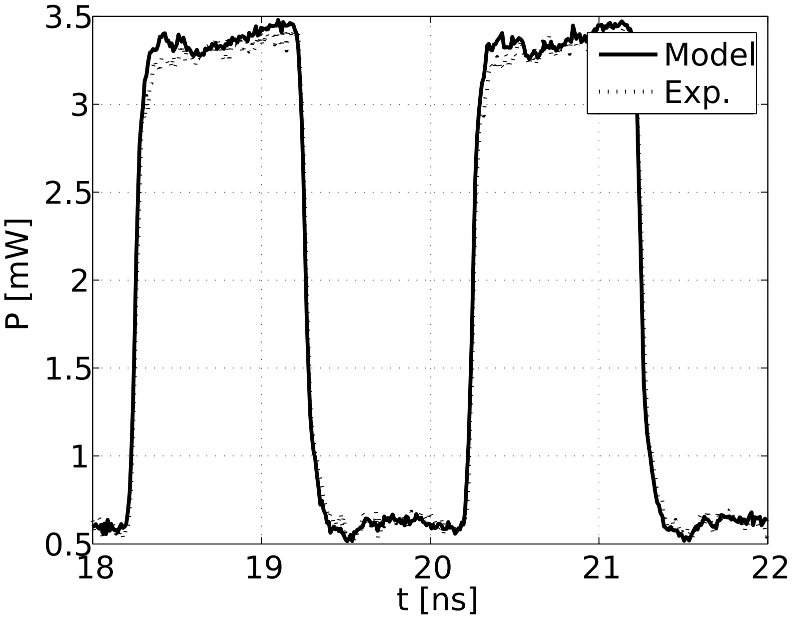

Figure 2.3: LOA dynamic response; mean input power -10 dBm.

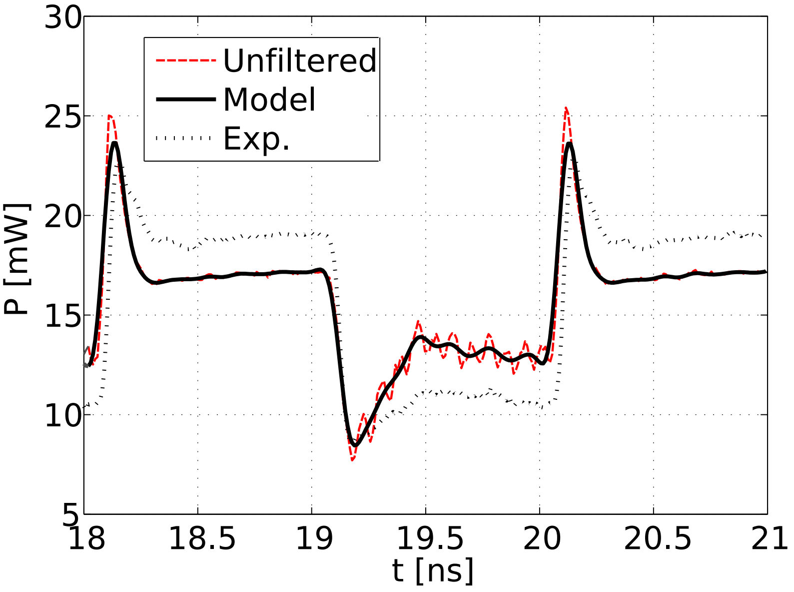

Figure 2.4: LOA dynamic response; mean input power +3 dBm.

Parameter	Value	Parameter	Value
Length	1 mm	Cavities	10
Transverse area, A	0.2 μm^2	Laser area, A_L	200 μm^2
Thickness, d	0.1μm	Overlap Factors, Γ and Γ_L	0.23
Carrier lifetime, τ	216 ps	Current, I	250 mA
Reflectivity	99.6%	Loss, α	6000 m^{-}1
Gain Parameter, A	2.16	Gain Parameter, B	9.97E-8

Table 2.1: Reservoir model parameters used to fit experimental results on Alphion SOA 5762.

2.2 Model validation

We now compare the simulation results of our model with static and dynamic measurements that were performed on a Finisar LOA [41]. At first, we measured the gain of the LOA versus input power using an input CW signal at 1550 nm. The setup used for this experiment is represented in the upper block diagram of Fig. 2.1. Measurements are shown in Fig. 2.2 along with simulations from the reservoir model, and a good fit is observed. Table 2.1 contains the values of the parameters used by the numerical simulator. A second experiment is represented in the lower block diagram in Fig. 2.1. A laser source is modulated with a Mach-Zehnder modulator driven by a square-wave. The output of the SOA is acquired by a digital sampling scope. Fig. 2.3 shows the dynamic response of the LOA to a square-wave input. The input mean power is -10 dBm, ensuring that the device is in a state where all the vertical lasers are ON. In this situation our model, fed with the measured input signal, well fits experimental results. The transmitter operates at 1Gb/s, and bandwidth limitations are due to the transmitter circuitry, as visible in the input signal inset. Fig. 2.4 shows the LOA behaviour in saturation. The amplifier is fed with a mean input power of 3 dBm and the extinction ratio is kept at 7dB so that the input power levels are those marked in Fig. 2.2. This way, we can test the gain clamping model when switching between near-linear and saturated modes of operation. When the same input signal is used for the simulations, the reservoir model well captures the transient behaviour of the amplifier. The large power overshoots are due to the clamping lasers turned momentarily off by the very large step transition in the input. The onset of gain-clamping is achieved after a small fraction of the bit duration, eventually reaching steady power on the mark level. A mark-zero transition in our setup makes the LOA operate in the near-linear region in Fig. 2.2, where the clamping lasers tend to oscillate in a metastable state. This produces ripples on the zeros which are averaged out by the receiver. An unfiltered simulation is added in Fig. 2.4 to show such remarkable feature, appearing only in this most critical situation. The residual offset of power levels in Fig. 2.4 is quantified by the mismatch of static gain curves in Fig. 2.2, which still require finer fitting.

2.3 Filters

Like in the SOA case let's now see how to derive a "reservoir" filter for the linear optical amplifiers. We expect that this filter will show that the gain-clamping technique enables to change the low-pass filter of a traditional SOA into a band-pass filter, so that lowpass components of the power transients will not interact with the amplifier, which will be able to work in presence of transients due to packets or add/drop of channels. The approach will begin by analysing a single LOA cavity. Let's consider eq. (2.15) in the presence of a perturbation of the state variable $r(t) = r_{SS} + \Delta r(t)$:

$$\begin{aligned}\dot{\Delta r} = \frac{I^i}{q} - \frac{r_{SS} + \Delta r(t)}{\tau} - \\ \sum_{j \in S} \left[(\bar{Q}_{j,in} + \Delta Q_j(t)) \frac{G_j(r)}{G_j(r) - \alpha L} \left(e^{G_j(r) - \alpha L} - 1 \right) \right] - \\ G_L(r^i)(\bar{Q}_L + \Delta Q_L(t)) \quad (2.40)\end{aligned}$$

where $\bar{Q}_{j,in}$ is the j-th input flux and $\bar{Q}_L$ is the photon flux of the vertical clamping laser. In the SOA case we obtained:

$$\frac{G_j(r)}{G_j(r) - \alpha L} \simeq M_{1,j}[1 - M_{2,j} B_j \Delta r] \quad (2.41)$$

where

$$\begin{cases} M_{1,j} = \frac{G_{j,SS}}{G_{j,SS} - \alpha L} \\ M_{2,j} = \frac{\alpha L}{(G_{j,SS} - \alpha L) G_{j,SS}} \end{cases} \quad (2.42)$$

are constants for the j-th signal and:

$$(e^{G_j(r) - \alpha L} - 1) \simeq K_{j,SS}(1 + B_j \Delta r) - 1 = (K_{j,SS} - 1) + K_{j,SS} B_j \Delta r \quad (2.43)$$

where

$$K_{j,SS} \triangleq e^{B_j r_{SS} - A_j - \alpha L}$$

is the total net gain of the j-th signal.

In the same way, for the vertical field we can write:

$$\begin{aligned} G_L(r) &= D_{Las} r - C_{Las} \\ &= D_{Las}(r_{SS} + \Delta r) - C_{Las} \\ &= (D_{Las} r_{SS} - C_{Las}) + D_{Las}\Delta r \\ &= G_{L,SS} + D_{Las}\Delta r. \end{aligned} \tag{2.44}$$

It is possible to write eq. (2.40) in this form:

$$\begin{multline} \dot{\Delta} r = \frac{I^i}{q} - \frac{r_{SS} + \Delta r(t)}{\tau} - \sum_{j \in S} \Bigg\{ \left[\bar{Q}_{j,in} + \Delta Q_j(t)\right] \\ M_{1,j}[1 - M_{2,j} B_j \Delta r(t)] \cdot [(K_{j,SS} - 1) + K_{j,SS} B_j \Delta r(t)] \Bigg\} - \\ \left[\bar{Q}_L + \Delta Q_L(t)\right]\left[G_{L,SS} + D_{Las}\Delta r(t)\right]. \end{multline} \tag{2.45}$$

The value of r_{SS} is calculated in the hypothesis of steady-state, so no perturbations at all:

$$\frac{r_{SS}}{\tau} = \frac{I^i}{q} - \sum_{j \in S} \bar{Q}_j M_{1,j}(K_{j,SS} - 1) - \bar{Q}_L G_{L,SS}. \tag{2.46}$$

Using this relation in eq. (2.45) and neglecting all the terms of higher orders we obtain:

$$\begin{multline} \dot{\Delta} r = -\frac{\Delta r(t)}{\tau} - \sum_{j \in S} \left\{ \bar{Q}_{j,in} M_{1,j} K_{j,SS} B_j \left[1 - M_{2,j} \frac{(K_{j,SS} - 1)}{K_{j,SS}}\right] \right\} \Delta r(t) \\ - \bar{Q}_L D_{Las} \Delta r(t) - \Delta Q_L(t) G_{L,SS} + \sum_{j \in S} \Delta Q_j M_{1,j}(1 - K_{j,SS}). \end{multline} \tag{2.47}$$

Defining:

$$A_j \triangleq \left\{ \bar{Q}_{j,in} M_{1,j} K_{j,SS} B_j \left[1 - M_{2,j} \frac{(K_{j,SS} - 1)}{K_{j,SS}}\right] \right\} \tag{2.48}$$

and the Laplace transform function of the reservoir perturbed equation becomes:

$$s\Delta R(s) = -\left(\frac{1}{\tau} + \sum_{j\in S} A_j + \bar{Q}_L D_{Las}\right)\Delta R(s) - \Delta Q_L(s) G_{L,SS} + \sum_{j\in S}\Delta Q_j(s) M_{1,j}(1-K_{j,SS}). \tag{2.49}$$

From the dynamic equation of the vertical laser field (2.18) it is possible to derive a relation from the two state variables of the cavity: $\Delta Q_L(s)$ and $\Delta R(s)$. From eq. (2.18), considering that at steady-state the gain is zero ($G_{L,SS} = d\Gamma_L g_{th}$) it is possible to write:

$$D_{Las} r_{SS} - C_{Las} - d\Gamma_L g_{th} = 0, \tag{2.50}$$

and again:

$$\begin{aligned}\frac{\partial Q_L^i(t)}{\partial t} &= \frac{v}{d} D_{Las}\Delta r(t)(\bar{Q}_L + \Delta Q_L(t)) \\ &= \frac{v}{d} D_{Las}\bar{Q}_L \Delta r(t)\end{aligned} \tag{2.51}$$

where the term containing the product of Δr and ΔQ_L has been neglected.

Its Laplace transform is:

$$s\Delta Q_L(s) = \frac{v}{d} D_{Las}\bar{Q}_L \Delta R(s)$$

from which we derived:

$$\Delta Q_L(s) = \frac{\frac{v}{d} D_{Las}\bar{Q}_L \Delta R(s)}{s} \tag{2.52}$$

that's the requested equation.

This equation can be written in eq. (2.49) obtaining:

$$\Delta R(s)\left\{ s + \frac{1}{\tau} + \sum_{j\in S} A_j + \bar{Q}_L D_{Las} + G_{L,SS}\frac{\frac{v}{d} D_{Las}\bar{Q}_L}{s}\right\} = = \sum_{j\in S}\Delta Q_j(s) M_{1,j}(1-K_j, SS) \tag{2.53}$$

$$\frac{\Delta R(s)}{s}\left\{s^2+s\left(\frac{1}{\tau}+\sum_{j\in S}A_j+\bar{Q}_L D_{Las}\right)+\frac{v}{d}G_{L,SS}D_{Las}\bar{Q}_L\right\}= \\ =\sum_{j\in S}\Delta Q_j(s)M_{1,j}(1-K_j,SS). \quad (2.54)$$

If we define

$$K(s)\triangleq\sum_{j\in S}\Delta Q_j(s)M_{1,j}(1-K_j,SS) \quad (2.55)$$

we can write:

$$\Delta R(s)=H_{LOA}(s)K(s) \quad (2.56)$$

where $H_{LOA}(s)$ is the reservoir filter for a single LOA cavity:

$$\begin{aligned} H_{LOA}(s) &= \frac{s}{s^2+s\left(\frac{1}{\tau}+\sum_{j\in S}A_j+\bar{Q}_L D_{Las}\right)+\frac{v}{d}G_{L,SS}D_{Las}\bar{Q}_L} \\ &= \frac{s}{s^2+\frac{1}{\tau_{LOA}}s+\frac{v}{d}G_{L,SS}D_{Las}\bar{Q}_L}. \end{aligned} \quad (2.57)$$

This is the expression of a band-pass filter and the term $\frac{1}{\tau_{LOA}}$ is defined here:

$$\frac{1}{\tau_{LOA}}=\frac{1}{\tau}+\sum_{j\in S}A_j+\bar{Q}_L D_{Las} \quad (2.58)$$

$$\frac{1}{\tau_{LOA}}=\frac{1}{\tau}+\sum_{j\in S}\left[\bar{Q}_{j,in}M_{1,j}K_{j,SS}B_j\left(1-M_{2,j}\frac{K_{j,SS}-1}{K_{j,SS}}\right)\right]+ \\ \bar{Q}_L D_{Las} \quad (2.59)$$

$$\frac{1}{\tau_{LOA}}=\frac{1}{\tau}+\sum_{j\in S}\left\{\bar{Q}_{j,in}\frac{G_{j,SS}}{G_{j,SS}-\alpha L}e^{G_{j,SS}}e^{-\alpha L}B_j \right. \\ \left. \cdot[1-\frac{\alpha L}{(G_{j,SS}-\alpha L)G_{j,SS}}\frac{(e^{G_{j,SS}}e^{-\alpha L}-1)}{e^{G_{j,SS}}e^{-\alpha L}}]\right\}+\bar{Q}_L D_{Las}. \quad (2.60)$$

Since $K_{j,SS}>>1$, we can write

$$\frac{K_{j,SS}-1}{K_{j,SS}}=\frac{(e^{G_{j,SS}}e^{-\alpha L}-1)}{e^{G_{j,SS}}e^{-\alpha L}}\simeq\frac{e^{G_{j,SS}}e^{-\alpha L}}{e^{G_{j,SS}}e^{-\alpha L}}=1, \quad (2.61)$$

obtaining:

$$\frac{1}{\tau_{LOA}} \simeq \frac{1}{\tau} + \sum_{j \in S} \frac{\bar{Q}_{j,in}}{(G_{j,SS} - \alpha L)^2} e^{G_{j,SS}} e^{-\alpha L} B_j [G_{j,SS}(G_{j,SS} - \alpha L) - \alpha L] + \bar{Q}_L D_{Las}. \quad (2.62)$$

The denominator of eq. (2.57) is a second order polynomial function that can be written as: $s^2 + 2\xi\Omega_n s + \Omega_n^2 = (s + s_1)(s + s_2)$ where

$$\Omega_n \triangleq \sqrt{\frac{v}{d} G_{L,SS} D_{Las} \bar{Q}_L} \quad (2.63)$$

is the natural pulsation of the system, $\xi \triangleq \frac{1}{2\tau_{LOA}\Omega_n}$ is the damping factor, and s_1 and s_2 are the roots, with $|s_1| = |s_2| = \Omega_n$. In eq. (2.62), the damping factor can be expressed as:

$$\xi = \frac{\frac{1}{\tau} + \sum_{j \in S} \frac{\bar{Q}_{j,in}}{(G_{j,SS} - \alpha L)^2} e^{G_{j,SS}} e^{-\alpha L} B_j [G_{j,SS}(G_{j,SS} - \alpha L) - \alpha L] + \bar{Q}_L D_{Las}}{2\sqrt{\frac{v}{d} G_{L,SS} D_{Las} \bar{Q}_L}}.$$

The terms $\frac{1}{\tau_{LOA}}$ and ξ depend on the signal powers, on their gains and on the intrinsic loss term α, on the average photon flux of the vertical laser.

Thanks to gain-clamping the low frequency does not reach the reservoir of the amplifer. They get absorbed by the vertical laser. In fact it is possible to calculate an approximation for the vertical laser filter, from eq. (2.52) and eq. (2.56):

$$H_L(S) = \frac{\frac{v}{d} D_{Las} \bar{Q}_L}{s^2 + \frac{1}{\tau_{LOA}} s + \frac{v}{d} G_{L,SS} D_{Las} \bar{Q}_L} = \frac{\frac{v}{d} D_{Las} \bar{Q}_L}{s^2 + 2\xi\Omega_n s + \Omega_n^2} \quad (2.64)$$

which is a second order low-pass filter, so $\Delta Q_L(S) = H_L(S)K(S)$.

2.4 Experimental comparison of SOAs

In this section the problem of choosing the best amplifier for a particular environment is addressed. The environment is a metropolitan area network (MAN) based on optical packets and WDM. The presence of optical packets and the add/drop of channels induces power transients on the line. It seems

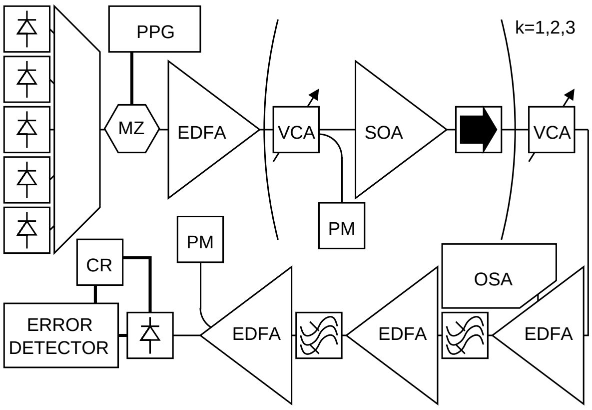

Figure 2.5: Experimental set-up.

that gain-clamping is the proper solution in order to improve performance by gain stabilisation. The implementation of gain clamping in Semiconductor Optical Amplifiers (SOA) can be achieved, due to their integrability, with different techniques and structures: grating along the propagation direction [32] or vertical laser [36]. We propose to experimentally investigate the performance of SOA versus gain clamped SOA (GC-SOA) to understand what can be the best candidate to realise an SOA based all-optical switch where the SOA are intended as WDM amplifiers or optical switches and not nonlinear devices like wavelength converters. Since carrier lifetime in SOA is in the order of 100 ps, gain-clamping in a packet switched environment where the bitrate is less than 10 Gbit/s is not mandatory. After one or few bits the amplifier state variable has already reached a new steady-state value. This particular circumstance is a good condition in order to test different SOA structure since each of them could work well.

2.4.1 Experimental Setup

The experimental setup, depicted in Fig. 2.5, has been designed to evaluate the impact of gain dynamics on the performances of a WDM transmission system amplified with SOA. The performance of three different SOA structures is evaluated through the curves of error-rate versus received OSNR. The parameters that have been changed are the number of injected signals, their power and the number of SOAs in the transmission line. Five 100 GHz spaced laser sources ($\lambda_1 = 1545.135$ nm to $\lambda_5 = 1545.135$ nm) are coupled together with a polarisation maintaining (PM) arrayed waveguide grating (AWG), which ensures that the five fields have the same polarisation vector. This WDM is modulated by a Mach-Zehnder modulator driven by a pulse-pattern generator (PPG) set to produce a $2^{31} - 1$ pseudo random bit sequence (PRBS) at 9.953 GHz. The EDFA that follows the modulator, functioning as a booster amplifier, enables us to inject in the fibre as much as 16 dBm of power. The five channels are equalised in order to have all the same average power. The voltage controlled attenuator (VCA) that follows the booster varies the optical power in the range -19 to +16 dBm. The transmission line we choose to investigate is a chain of SOAs where attenuators introduce losses between the amplifiers. This scheme reflects the structure of an SOA based optical switch. The basic block of this channel is constituted by an attenuator, a splitter, a power meter, and the SOA under test followed by an isolator. Attenuators are used to set the input power level of the amplifier. This power is monitored through a 99/1 splitter and a power meter connected to its -20 dB output. The three different SOA structure that have been tested are: standard SOA, gain-clamped SOA (GC-SOA) [32] and Linear Optical Amplifiers (LOA) [36].

In order to measure error rates in the range 10^{-3} – 10^{-9} the attenuator before the receiver degrades the OSNR of the signals. The OSNR is measured through an optical spectrum analyser (OSA), with a resolution bandwidth of 0.2 nm, connected to the monitor output of the first EDFA of the receiver. After this EDFA, a tunable optical bandpass filter selects the desired channel and a second EDFA is used to recover the power loss. Another filter, more selective (Bo$\simeq$0.25 nm), and another EDFA are used to remove ASE noise and to feed the photodetector with constant input power. The photodetector has a bandwith of 12 GHz and an electronic integrated transimpedance amplifier (TIA). A clock recovery is used to generate the clock signal for the error detector. In all the measures described hereafter the central channel, λ_3, will always be the extracted one.

2.4.2 Results

Each test consisted in measurements of BER varying the OSNR at the detector. At first, each device was tested separately, being the only device present in the transmission line. Fig. 2.6 reports the sensitivity curves of a standard SOA. Each curve represents the performance for a different value of input power. Every point of each curve was measured varying the decision threshold of the

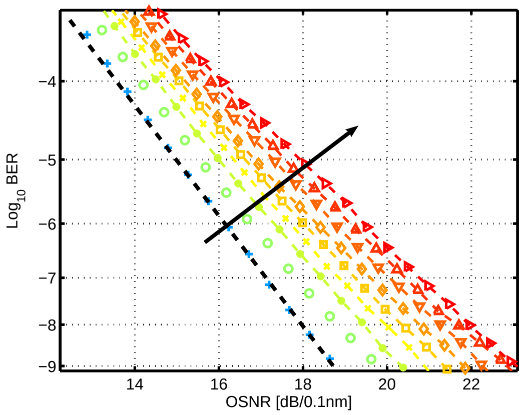

Figure 2.6: BER versus OSNR for input powers ranging from -18 dBm to 5 dBm. SOA5760 with 5 channels turned on. Black dotted line represent back to back.

error detector hence the curves represent the error rate at the optimum threshold. This is a technique that requires a lot of time, especially for the points closer to 10^{-9}. To acquire all these BER curves all the setup has been automatised and it is driven by a PC. The curves in Fig. 2.6 have been measured with all the five sources turned on. To understand what's the effect responsible for the performance penalty these measures have been taken also in the single channel case and with three channels only. Since we measure the total input power and all the channels have the same power, they are co-modulated, and there's no dispersion, the SOA works at the same saturation regime. Varying the number of transmitted channels without changing the total input power permits us to quantify the impact of cross nonlinear effects with respect to self gain modulation penalty. In order to compare performances of different setups from each set of measurements like the one presented in Fig. 2.6, the OSNR penalty for a given BER of 10^{-5} was extracted. In Fig. 2.7 the OSNR penalty versus the total mean input power is reported for the same device of Fig. 2.6, SOA model 5760. Each one of the figures between Fig. 2.7 and Fig. 2.15 propose the OSNR penalty for each one of the nine devices that have been tested, three for each kind of device. On the Y-axis there is the OSNR penalty measured at a BER of 10^{-5} while on the X-axis there is the total input power P_{IN} TOT.

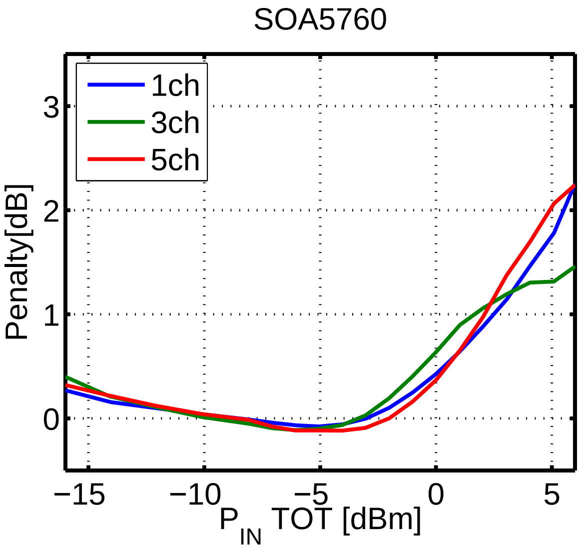

Figure 2.7: OSNR penalty versus input power for the SOA5760 with 1,3 and 5 channels. Current I = 250mA.

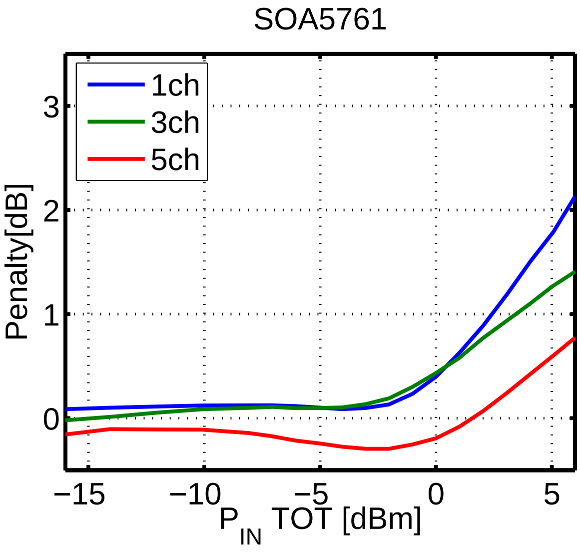

Figure 2.8: OSNR penalty versus input power for the SOA5761 with 1,3 and 5 channels. Current I = 250mA.

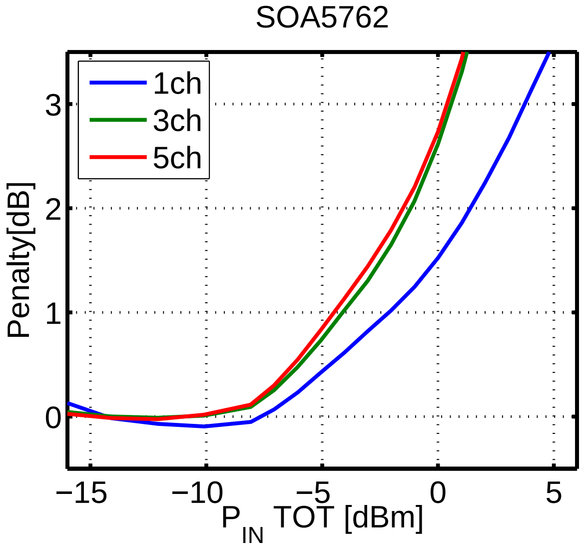

Figure 2.9: OSNR penalty versus input power for the SOA5762 with 1,3 and 5 channels. Current I = 250mA.

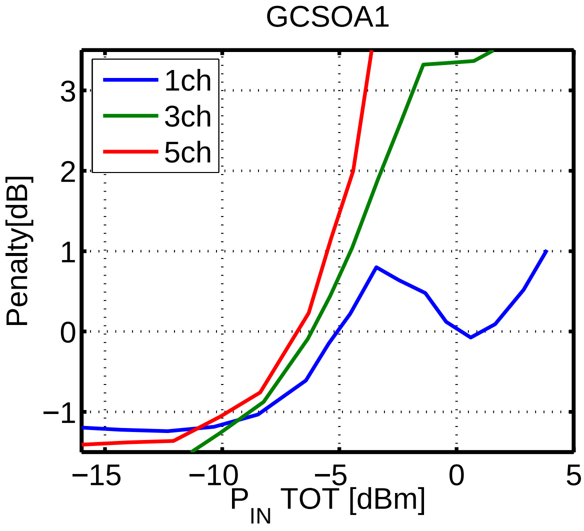

Figure 2.10: OSNR penalty versus input power for the GCSOA1 with 1,3 and 5 channels. Current I = 250mA.

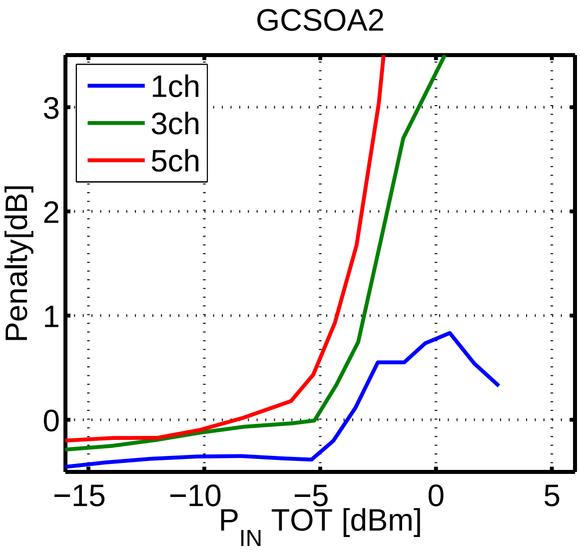

Figure 2.11: OSNR penalty versus input power for the GCSOA2 with 1,3 and 5 channels. Current I = 250mA.

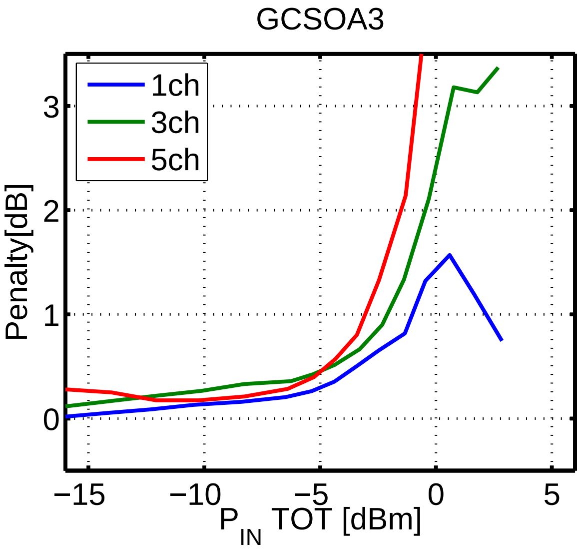

Figure 2.12: OSNR penalty versus input power for the GCSOA3 with 1,3 and 5 channels. Current I = 250mA.

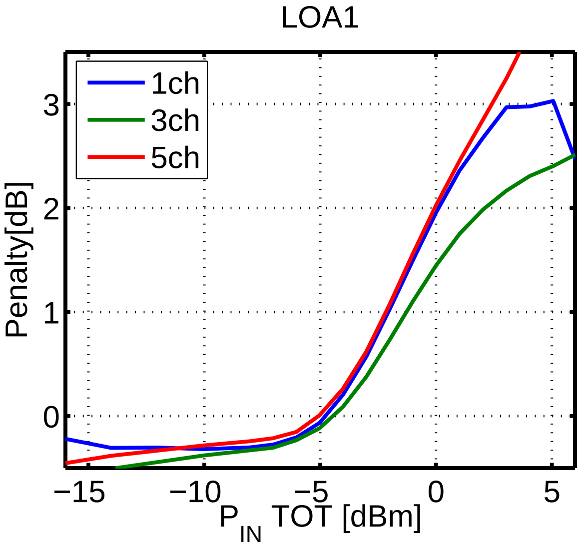

Figure 2.13: OSNR penalty versus input power for the LOA1 with 1,3 and 5 channels. Current I = 250mA.

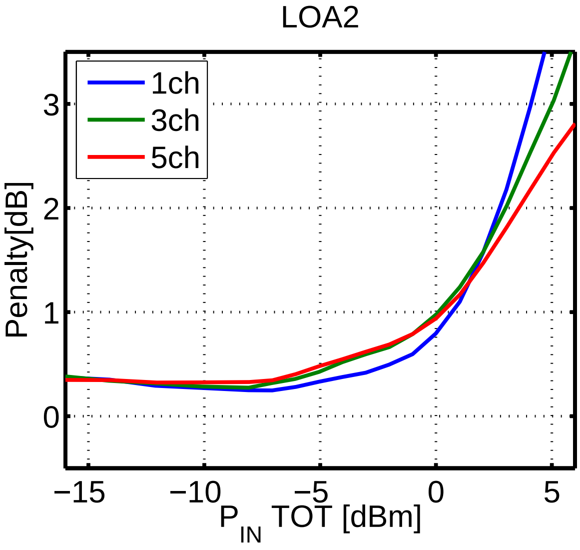

Figure 2.14: OSNR penalty versus input power for the LOA2 with 1,3 and 5 channels. Current I = 250mA.

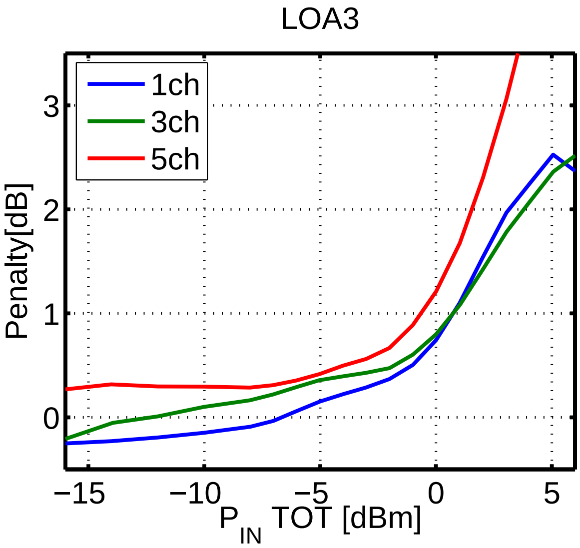

Figure 2.15: OSNR penalty versus input power for the LOA3 with 1,3 and 5 channels. Current I = 250mA.

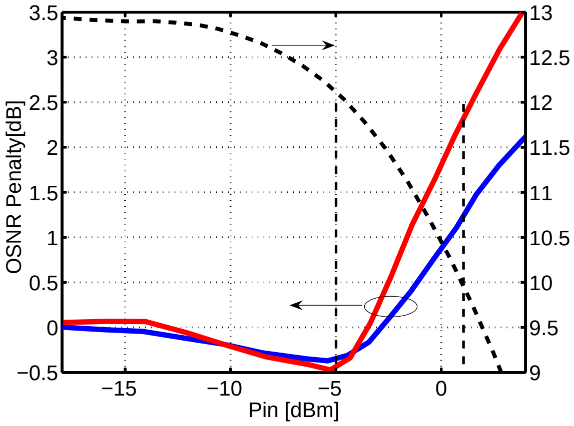

Figure 2.16: OSNR penalty versus input power for the SOA5760. Two cases: single channel (blue) and 5 channels (red). The dotted line refers to the right y-axis and represent the SOA gain saturation.

The most evident aspect is that single channel transmission amplified with GCSOA presents an anomalous behaviour. This fact can be explained if we consider that in the case of GCSOA the penalties are due to the internal laser oscillations. In fact the laser round-trip time is comparable with the bitrate and this leads to a disastrous resonance effect. When the input power is so high that even for a transmitted zero the internal laser is turned off, then the penalty curve has a local minimum (see Fig. 2.10). It has been already mentioned that this kind of measure needs several hours to be concluded. Because of thermal drifts the modulator and other components present variable performances. In order to take into account these drifts it is better to perform a sort of calibration of the setup by taking a back-to-back measurement after each transmission. In this way, by referring the acquired transmission BER vs. OSNR curve to the closest back-to-back it is possible to improve the accuracy of the final result. The two curves presented in Fig. 2.16 represent two cases: single channel transmission and five channels transmission. On the second y-axis it is possible to read the value of the gain for the same input power. It's approximately for 1 dB of gain compression that the penalty curves begin to rise and it's near 3 dB of gain compression that the penalties reach noticeable values. It's interesting to note that the curve with 5 channels turned on, with respect to the single channel case, does not begin to rise before the other but it rises with a faster slope. The saturation of an amplifier should be taken into account: since each device has a different saturation point, it is not fair to put in relation the curves from one of these figures to another. If we define P_{1dB} the power that gives 1 dB of gain compression, then it is clear that it is important to evaluate the performance of each device with the same ratio $P_{rel} \triangleq P_{IN}/P_{1dB}$. Unfortunately a direct consequence of the presence of an internal laser in the gain-clamped devices is that the saturation level is unknown. In fact the measured saturation characteristic (G vs. P) is the clamped-one. The power level seen by the active medium is not the input power only but it is the input power plus the internal laser power, which is unknown. For input power levels in the linear region (where the gain is constant) the power seen by the active medium is mainly due to the internal laser; for input power levels in the "saturated" region (where the gain is dropping) the power seen by the active medium is mainly the input power. The typical design of a gain-clamped amplifier is chosen in order to have an internal laser power that keeps the amplifier saturated. Consider, for example, an amplifier with an ideal saturation curve that is constat at a given gain $G_0 = 20$ dB for input powers $P_{IN} < P_{SAT} = 0$ dBm and that after this threshold the gain decreases by 1 dB for each dB of input power. Then consider to add the gratings needed to gain-clamp the amplifier and suppose that the new device has a new linear gain $G_{0,GC} = 18$ dB; of course the new saturation threshold will be $P_{SAT,GC} = 2$ dBm. By looking at the nonlinear penalties of this device at 1dB of gain compression we are looking at an active medium which is working at 3 dB of gain compression and not 1 as desired. So we are overestimating the -1dB saturation input power by at least 2dB.

Although it is difficult to estimate the real saturation of a gain-clamped amplifier, there is no choice. For a fair comparison the saturation should be taken into account. For this reason all the saturation input powers have been measured (see Fig. 1.2). In all the curves reported from Fig. 2.17 to Fig. 2.25 the same results are plotted versus P_{rel} instead of P_{IN} TOT. It seems that standard SOA devices are the ones with the smallest nonlinear impact. The fact is that at least for them it is fair to use this comparison since the SOA5762, which is the one with the highest gain and lowest saturation power, now behaves like the other two. If all the tested devices were made on the same semiconductor layer, this measurment could have been used in order to extract the unknown value of input laser power. But, since the tested devices are completely different, this case does not apply.

After these measurements involving a single device, a chain of similar devices has been tested. In Fig. 2.26, Fig. 2.27 and, Fig. 2.28 we report the OSNR penalties versus total input power for a chain of three devices of the same kind(3 SOA, 3 GC-SOA and, 3 LOA respectively). The axis limits have been changed since penalties grow faster and for lower input powers. In order to have 1 dB of penalty it is necessary to work with a total input power of -7 dBm in the case of a chain of SOAs with 5 channels. It is evident that semiconductor devices are strongly affected by nonlinear effects and thus a modulation format with constant power should perform better.

2.5 Conclusions

A novel reservoir LOA dynamic model was introduced. For the first time, simulation results from a LOA model are checked against experimental measurements performed on a commercial device. The purpose of the proposed model is twofold. First, it reduces the equations describing the LOA to a minimal complexity, using a single state variable for each independent amplifier

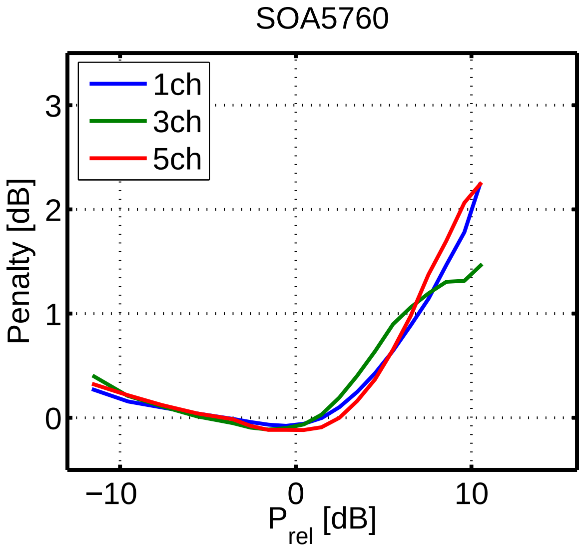

Figure 2.17: OSNR penalty versus input power for the SOA5760 with 1,3 and 5 channels. Current I = 250mA.

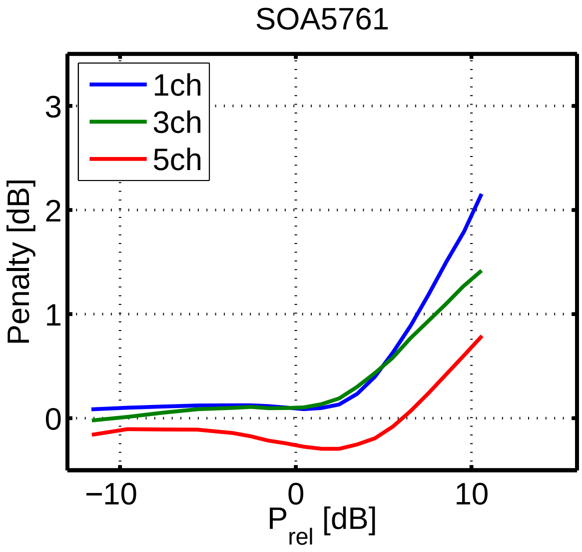

Figure 2.18: OSNR penalty versus input power for the SOA5761 with 1,3 and 5 channels. Current I = 250mA.

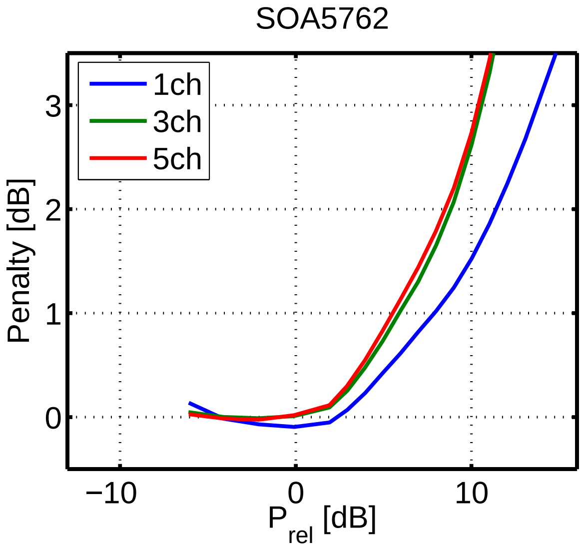

Figure 2.19: OSNR penalty versus input power for the SOA5762 with 1,3 and 5 channels. Current I = 250mA.

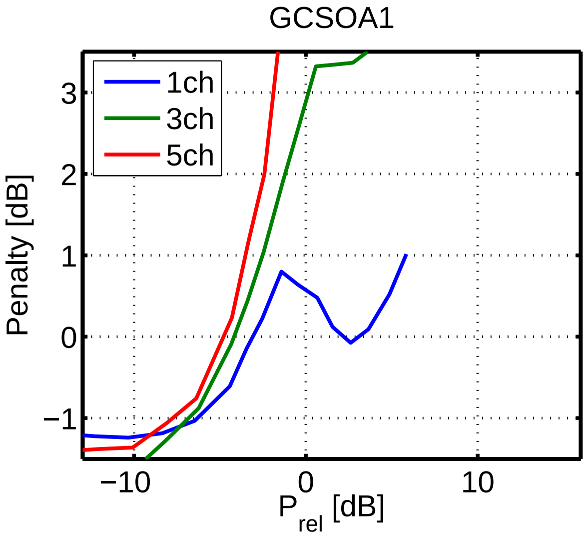

Figure 2.20: OSNR penalty versus input power for the GCSOA1 with 1,3 and 5 channels. Current I = 250mA.

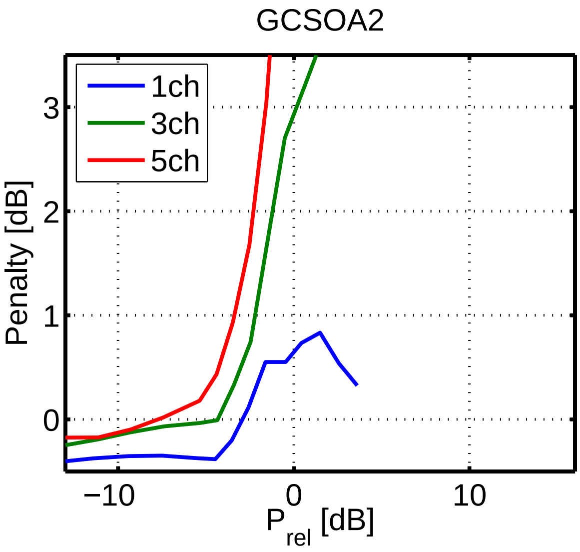

Figure 2.21: OSNR penalty versus input power for the GCSOA2 with 1,3 and 5 channels. Current I = 250mA.

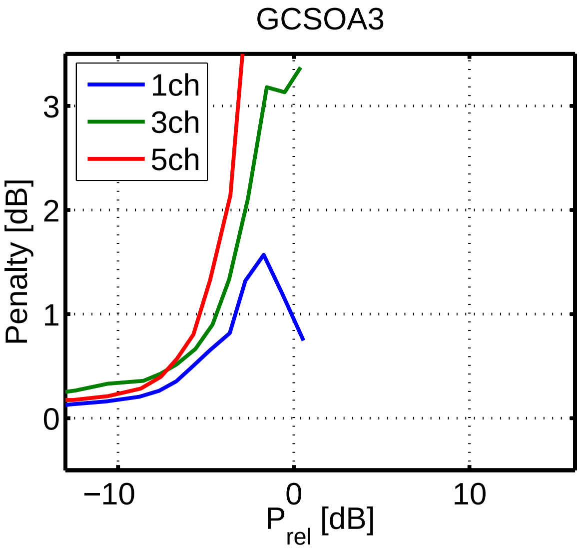

Figure 2.22: OSNR penalty versus input power for the GCSOA3 with 1,3 and 5 channels. Current I = 250mA.

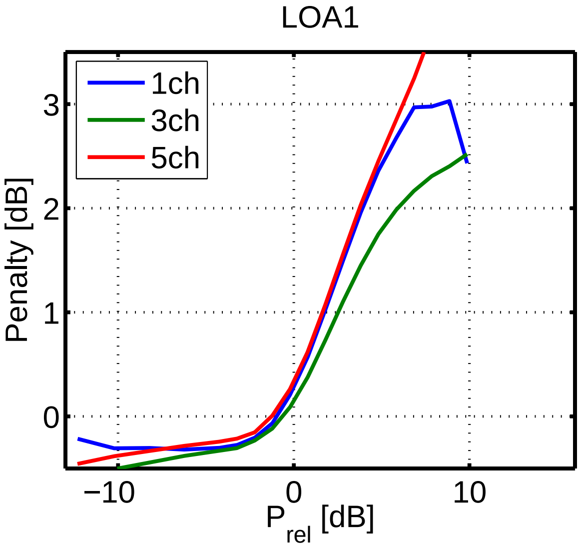

Figure 2.23: OSNR penalty versus input power for the LOA1 with 1,3 and 5 channels. Current I = 250mA.

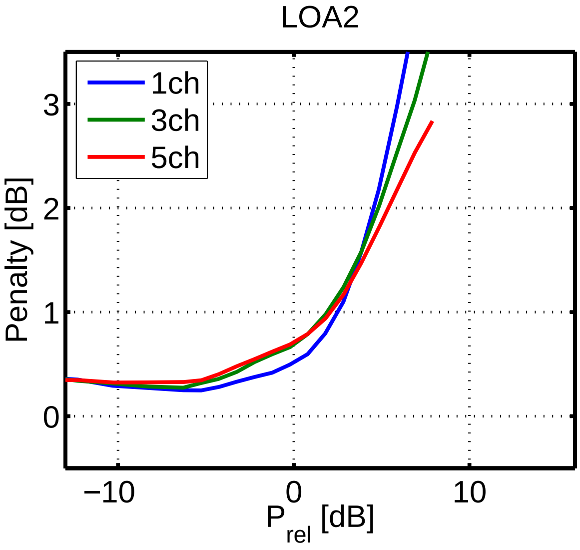

Figure 2.24: OSNR penalty versus input power for the LOA2 with 1,3 and 5 channels. Current I = 250mA.

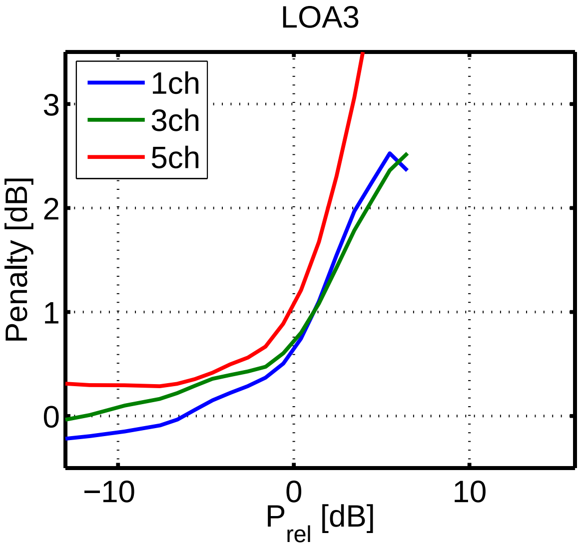

Figure 2.25: OSNR penalty versus input power for the LOA3 with 1,3 and 5 channels. Current I = 250mA.

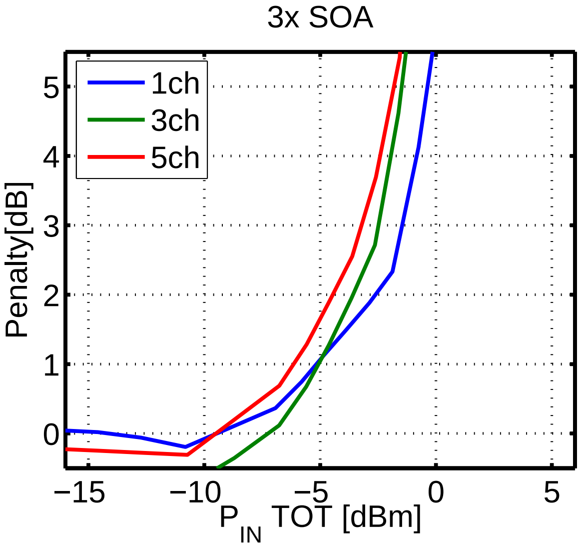

Figure 2.26: OSNR penalty versus input power for a chain of 3 SOA with 1,3 and 5 channels. Current I = 250mA.

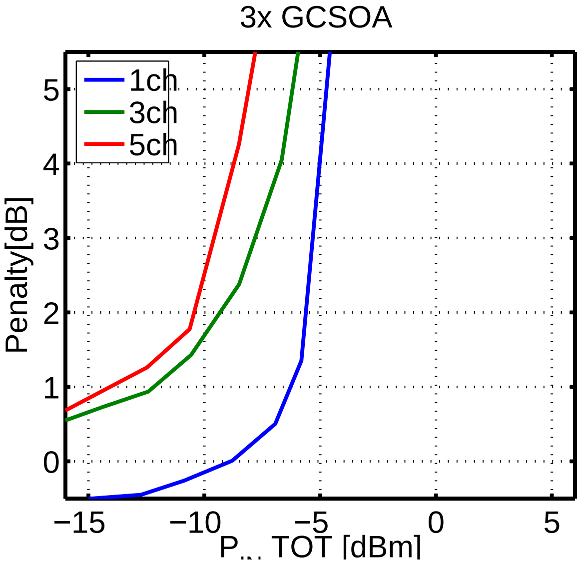

Figure 2.27: OSNR penalty versus input power for a chain of 3 SOA with 1,3 and 5 channels. Current I = 250mA.

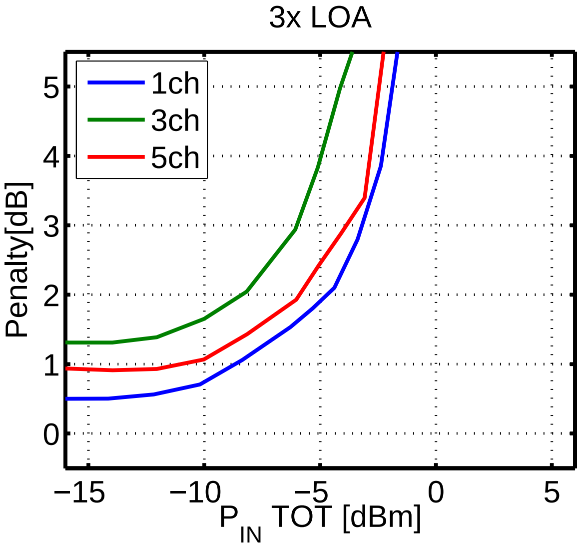

Figure 2.28: OSNR penalty versus input power for a chain of 3 SOA with 1,3 and 5 channels. Current I = 250mA.

cavity; hence, it is suitable for performing fast simulations in optical network design. Second, the model gives analytical insight and a monitoring of the LOA transverse clamping lasers, otherwise not accessible from the device. In addition, thanks to the reservoir approach, there is no need for solving joint differential equations for signals and ASE, hence the low computation times are little affected by the number of channels. The model is thus a good tool in WDM large optical networks simulations.

Although these are very good achievements, the last section of the chapter, with the experimental comparison, shows the faults of the gain-clamped devices. In a SOA based switch there are no added benefits by using a gain-clamped structure for a bitrate of 10 Gbit/s. The extended linear region is not linear at all. In fact nonlinear effects arise despite of gain-clamping. When there is the need for a WDM SOA based amplification then it would be better to look for different solutions since gain-clamping do not constitute a true improvement. OOK modulation format with SOA based amplification does not work well with chain of amplifiers, but DPSK modulation format could perform much better. For transmission purposes the best working point is close to the 1 dB gain compression value. This means that in order to exploit all the benefits given by a gain-clamped structure it is necessary to work below this optimum point.

Chapter 3

Optical Coherent Detection

In most networks, WDM channels at 40-Gbit/s rate have to be sent over links designed for 10-Gbit/s rate. However, fibre transmission is more challenging at 40 Gbit/s than at 10 Gbit/s. Advanced modulation formats such as differential phase-shift keying (DPSK), [42–44], phase-shaped binary transmission (PSBT) [45], and differential quadrature phase-shift keying (D-QPSK) [46,47] have been proposed in order to reduce the performance gap when comparing the two bit-rates, but up to a certain extent only [47–49]. A promising solution against fibre impairments for 40-Gbit/s channel rate is to reduce the symbol rate to 10 Gbaud. This is obtained by coding information over four phase levels, according to the quadrature phase shift keying (QPSK) format, and over two orthogonal polarisation states thanks to polarisation multiplexing.

At the receiver side, polarisation demultiplexing is achieved by coherent detection and digital signal processing (DSP). The interest of the coherent detection solution is twofold here. First, it has to be highlighted that polarisation demultiplexing is almost straight forward with coherent detection, only involving improved DSP algorithms [50–53] without any additional optoelectronic hardware compared to singly polarised data transmission. Second, contrary to conventional direct detection schemes which are extremely sensitive to polarisation mode dispersion (PMD) [54] and polarisation dependent loss (PDL), coherent detection provides access to all the signal characteristics (polarisation, amplitude, and phase) and offers the possibility to compensate for several linear impairments, thanks to high-speed digital signal processing (DSP). Among these linear impairments, the high tolerance to optical noise has first been observed [55] using coherent detection and DSP at the receiver side. Next, the compensation of accumulated chromatic dispersion has been demonstrated in uncompensated long haul transmission [56, 57] using a finite impulse response (FIR) filter, with a number of taps proportional to the amount of cumulated dispersion.

An experimental investigation of the tolerance of 40 Gb/s coherent polarisation division multiplexing (PDM)-QPSK to linear impairments such as narrow optical filtering, chromatic dispersion (CD) and PMD is the main topic of this chapter, which is organised as follows:

In section 3.1 basic concepts such as optical modulation formats and polarisation multiplexing are introduced.

In section 3.2 the structure of the optical coherent detector and the algorithm of the digital signal processor are described.

In section 3.3 the experimental setup used for the generation of PDM-QPSK modulation as well as the particular configuration of the coherent receiver are described. The experimental results obtained after 400 km transmission in terms of tolerance to optical filtering and PMD are reported. Finally a WDM transmission experiment over 4080 km is illustrated, where not only the effect of PMD/PDL but also the effects of chromatic dispersion and narrow filtering due to reconfigurable optical add drop multiplexers (ROADMs) have been emulated and successfully mitigated.

3.1 Optical modulation formats

In this section, theory and practical schemes for optical modulation techniques will be exposed. Through the same basic component, the Mach-Zehnder modulator, it is possible to realise several optical modulation formats. A more complex scheme, still based on the same interferometric structure, is required for the QPSK modulation.

3.1.1 On-Off Keying

On-Off Keying (OOK) is the most elementary amplitude modulation format. It is a binary modulation format where the transmitted bits $\{0, 1\}$ correspond to the presence or absence of light. This modulation can be obtained by direct modulation or with an external modulator. Direct modulation requires to turn on and off the laser diode and has many disadvantages since it changes the central frequency of the laser. In high performance systems only external

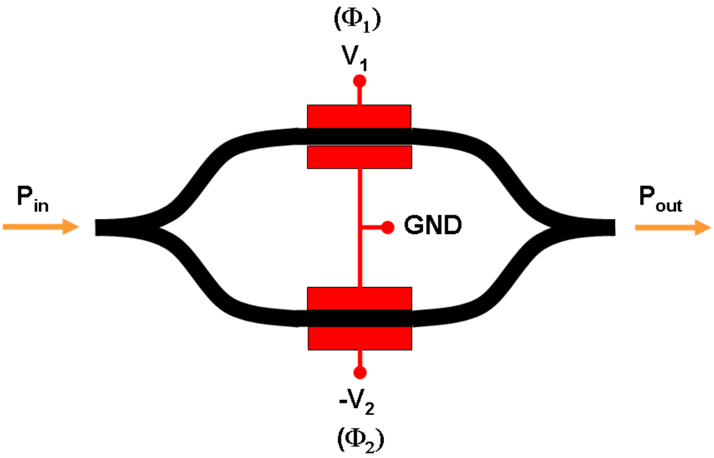

Figure 3.1: Scheme of a Mach-Zehnder modulator.

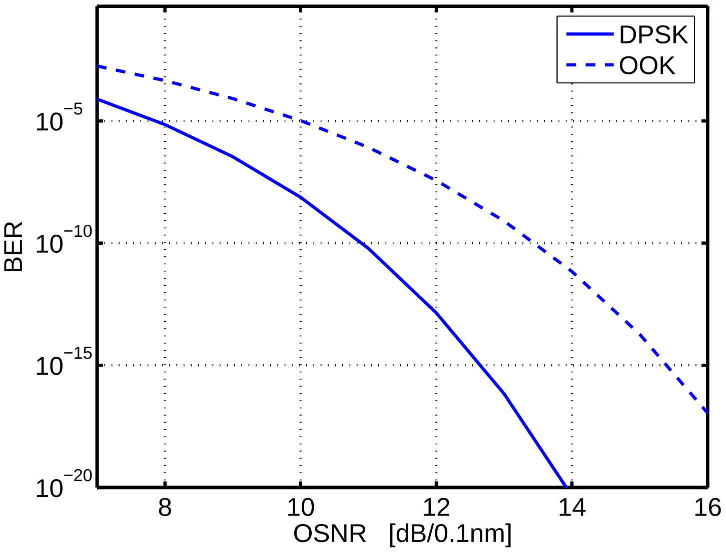

Figure 3.2: Theoretical curves of sensitivity for NRZ-OOK (solid) and DPSK (dashed) at R = 10 Gbit/s.

modulators are employed; the most common one is the Mach-Zehnder interferometer. Its interferometric structure is depicted in Fig. 3.1; the incoming optical field is split along two paths and then combined again. The structure is integrated in a waveguide together with electrical contacts that can change the refractive index of one or both paths. By varying the driving electrical voltage it is possible to add a delay between the upper and lower arms of the interferometer. When the two fields recombine there is an interference that can be constructive or destructive. When the delay imposed by the electrical signal is the one corresponding to a phase difference of π then the two fields form a destructive interference and there is no optical power going out of the modulator. If we plot the optical output power vs. voltage of a modulator we can see that it looks like a squared sine with a phase offset. The voltage difference between a peak and a through is called V_π. In order to modulate a signal with an NRZ-OOK the input voltage DC value (called bias voltage) should be set to match the middle point of the P vs. V function (also called the -3dB point) and the RF voltage should have a $V_{p-p} = V_\pi$. Another very popular OOK modulation format is the RZ-OOK (return to zero), where a shorter pulse is used. The sensitivity curve of NRZ OOK for 10 Gbits/s modulation formats is reported in Fig. 3.2. Those curves are calculated using an electrical forming pulse of the raised cosine type with a roll-off factor of 0.2. The sensitivity is calculated after optical filtering with a normalised bandwith 1.6 and a Bessel electrical filter of normalised bandwidth 0.65.

3.1.2 Phase Shift Keying

Phase Shift Keying (PSK) is the name of the most general constant envelope modulation format. In optics the most used PSK modulation is BPSK (Binary PSK), with differential coding (and for this reason it is called DPSK). This format can be obtained mainly in two ways: with a Mach-Zehnder modulator or with an optical delay line (phase modulator). In the first case it is not true that the envelope is constant over the entire bit length but there are many advantages connected with this technique. The first one is that it is very similar to OOK, in fact there are only two differences: the bias voltage should be changed in order to match a through of the P-V function and the RF frequency should by doubled in order to move between two adjacent peaks. The BPSK transmits a binary alphabet $\{-1, +1\}$ and to transmit a DPSK a differential coder should be added. The delay line modulator works directly on the phase of the signal. This means that on the complex plane the phase moves across a semicircular path with constant modulus. The Mach-Zehnder on the contrary moves the transmitted field along the real axis, realising a phase jump of exactly π rad instead of a continuous phase change. While there are several cases in which a constant envelope could be very helpful (e.g. with SOAs, see previous chapters), in long-haul transmission systems it is better to have a sharp phase change in combination with a minimum of optical power. This is because phase changes that take place when the optical power is low do not induce nonlinear effects. Moreover, delay line modulators can be employed over long-haul transmission but a pulse carver is added. A pulse carver is a second modulator that creates “holes” in the optical power in correspondence of phase changes. In Fig. 3.2 the theoretical sensitivity curve for a 10 Gbit/s DPSK modulation format is reported. These curves have been calculated with the *optilux* simulator [58] using the Karhunen-Loève series expansion method [59].

3.1.3 QPSK

Quaternary Phase Shift Keying is a particular case of PSK where the alphabet has 4 symbols equispaced by $\pi/2$. This modulation format needs a dedicated section for several reasons: it is the first modulation format presented which is not binary, and to obtain a QPSK signal in optics a particular modulator scheme is needed. This scheme, called IQ modulator, is very general and is the basic transmitter scheme for any kind of PAM/PSK modulation. The modulator is a special kind of Mach-Zehnder interferometer called QI modulator. A QI modulator contains two independent traditional Mach-Zehnder interferometers coupled together with an adjustable phase offset. If the upper interferometer applies the in-phase component of the modulation, the lower one applies the in-quadrature component. The adjustable bias is able to add the required $\pi/2$ phase offset between I and Q. When the electrical signal on the I-modulator and the one on the Q-modulator are of the same kind as the one used for the BPSK, then a QPSK modulation is obtained. More complex modulation formats require more complex electrical signals. Phase transitions with this kind of modulator are of two kinds: both I and Q change or just one of them does. In the first case the optical power crosses the zero point, in the other the power reaches a minimum corresponding to half the peak value. Differential coding is more complex when the alphabet is quaternary. The coding scheme should be carefully chosen in order to respect the circular symmetry required to ignore a potential phase mismatch between the transmitted carrier

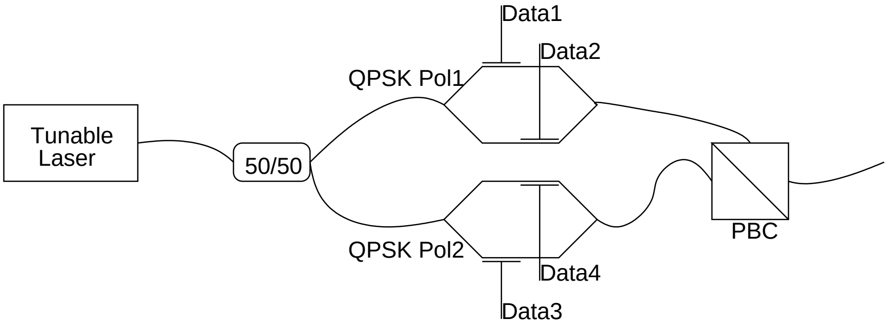

Figure 3.3: Polarisation multiplexed transmitter scheme.

and the received one.

3.1.4 Polarisation Multiplexing

The source of the electric field that is transmitted through the optical link is a tunable laser diode. The output of this diode is

$$\vec{E_s}(t) = E_s e^{j(\omega_s(t)t + \psi_s'(t) + \Phi_0)} \hat{\mathbf{i}} \tag{3.1}$$

where E_s^2 is the output power of the laser in mW, $\psi_s'(t)$ is the phase noise of the source, Φ_0 is the phase reference and the vector $\hat{\mathbf{i}}$ represents the polarisation of the electromagnetic field. The laser frequency is modulated (dithering) so that $\omega_s(t) = \omega_s + 2\pi\varepsilon\cos(2\pi f_M t)$ where $\omega_s = \frac{c}{2\pi\lambda_s}$ is the central frequency of the laser, $\varepsilon \simeq$ 50MHz is the modulation depth and $f_M \simeq$ 50kHz is the modulation frequency[1]. Considering that the symbol rate R will be at least 10Gbaud, the ratio $\frac{f_M}{R} < 10^{-5}$ enables us to consider the dithering as a slow variation. Besides, we can consider that the phase noise is a Wiener process whose increments, denoted by a temporal increment τ, have variance $\sigma^2 = 2\pi\tau\Delta\nu$ where $\Delta\nu$ is the linewidth of the laser diode ($\simeq$ 100kHz in our case). For the sake of simplicity we prefer to emphasize the constant value of the central wavelength with respect to all the other terms present in the phase. Thus we can write

$$\vec{E_s}(t) = E_s e^{j(\omega_s t + \psi_s(t))} \hat{\mathbf{i}} \tag{3.2}$$

where $\psi_s(t) = \varepsilon\cos(2\pi f_M t) + \psi_s'(t) + \Phi_0$.

---

[1] This is a technique to suppress Brillouin effect.

We want to investigate two kinds of transmitter settings: single polarisation and polarisation multiplexing. The scheme of our transmitter is described by Fig. 3.3. For single polarisation transmission, the second QPSK modulator is switched off and the transmitted signal after the first QPSK modulator becomes:

$$\vec{E_s}(t) = E_s(t)e^{j(\omega_s t+\varphi(t)+\psi_s(t))}\hat{\mathbf{i}} \tag{3.3}$$

where the amplitude has become time varying and the phase modulation term $\varphi(t)$ has been added. Ideally, this term should be written as:

$$\varphi(t) = \sum_i \Pi(t - iT)d_i$$

where Π is the gate function, $T = 1/R$ is the symbol period and $d_i \in (k\frac{2\pi}{M})$ with $k = 0, \ldots, M - 1$ is the i-th transmitted symbol in the general M-PSK case. We will study only the case of BPSK ($M = 2$) and QPSK ($M = 4$). For polarisation multiplexed transmission both modulators are working and the transmitted signal is

$$\begin{aligned}\vec{E_s}(t) &= E_{s1}(t)e^{j(\omega_s t+\varphi_1(t)+\psi_{s1}(t))}\hat{\mathbf{i}} + E_{s2}(t)e^{j(\omega_s t+\varphi_2(t)+\psi_{s2}(t))}\hat{\mathbf{j}}\\ &= (E_{s1}(t)e^{j(\varphi_1(t)+\psi_{s1}(t))}\hat{\mathbf{i}} + E_{s2}(t)e^{j(\varphi_2(t)+\psi_{s2}(t))}\hat{\mathbf{j}})e^{j\omega_s t}\end{aligned} \tag{3.4}$$

where the polarisation vectors $\hat{\mathbf{i}}$ and $\hat{\mathbf{j}}$ are orthogonal and the intrinsic phase terms on the two polarisations are related in this way: $\psi_{s1}(t) = \psi_{s2}(t + \tau_p)$, where τ_p is the delay of the second polarisation with respect to the first one due to the different path lengths.

3.2 Coherent Detector Scheme

The principle scheme of the receiver is depicted in Fig. 3.4. Calling $\hat{\mathbf{x}}$ and $\hat{\mathbf{y}}$ the polarisation axes of the PBS at the beginning of our receiver, the first two photodiodes (PD1 and PD2) will detect the components along the $\hat{\mathbf{x}}$ direction while the other two photodiodes (PD3 and PD4) will detect the components along the $\hat{\mathbf{y}}$ direction. The received field is in the form:

$$\vec{E_r}(t) = E_{rx}\hat{\mathbf{x}} + E_{ry}\hat{\mathbf{y}} \tag{3.5}$$

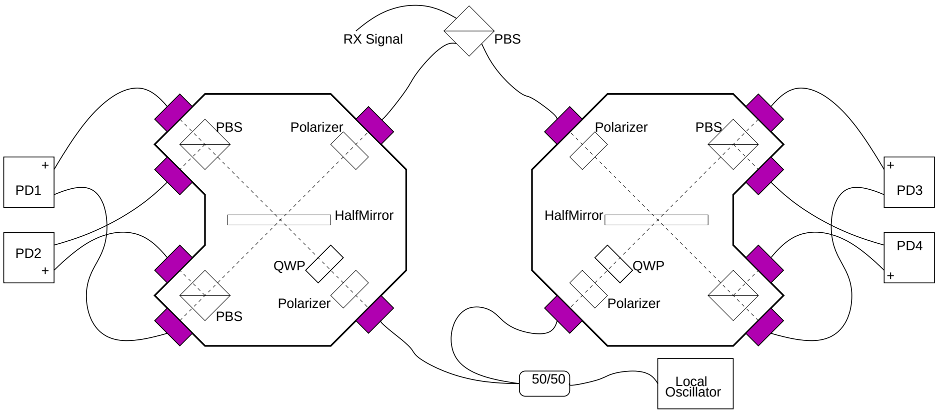

Figure 3.4: Scheme of the coherent receiver with polarisation diversity.

and the two components E_{rx} and E_{ry} are separately detected by two pairs of balanced photodiodes. In particular, considering that each reflection is responsible for a $\frac{\pi}{2}$ phase offset, the light is split on the photodiodes as follows:

$$\left\{\begin{array}{l} E_{r1^+} = \frac{1}{2\sqrt{2}} E_{rx} e^{j\frac{\pi}{2}} \\ E_{r1^-} = \frac{1}{2\sqrt{2}} E_{rx} \\ E_{r2^+} = \frac{1}{2\sqrt{2}} E_{rx} e^{j\frac{\pi}{2}} \\ E_{r2^-} = \frac{1}{2\sqrt{2}} E_{rx} e^{j\pi} \end{array}\right. \qquad \left\{\begin{array}{l} E_{r3^+} = \frac{1}{2\sqrt{2}} E_{ry} e^{j\frac{\pi}{2}} \\ E_{r3^-} = \frac{1}{2\sqrt{2}} E_{ry} \\ E_{r4^+} = \frac{1}{2\sqrt{2}} E_{ry} e^{j\frac{\pi}{2}} \\ E_{r4^-} = \frac{1}{2\sqrt{2}} E_{ry} e^{j\pi}. \end{array}\right. \tag{3.6}$$

The local oscillator (LO) is a laser diode identical to the transmitter one. After the rotation due to the $\pi/4$ polariser and the quarter-wave plate (QWP), the laser beam from the LO can be written as:

$$E_{LO}(t) = \frac{E_{LO}}{\sqrt{2}} e^{j(\omega_{LO}t+\psi_{LO}(t))} (e^{j\frac{\pi}{2}} \hat{\mathbf{x}} + \hat{\mathbf{y}}) \ . \tag{3.7}$$

So if we consider the reflections inside the coherent mixer, we have:

$$\left\{\begin{array}{l} E_{LO1^+} = E_{LO3^+} = \frac{1}{2\sqrt{2}} E_{LO} e^{j\frac{\pi}{2}} \\ E_{LO1^-} = E_{LO3^-} = \frac{1}{2\sqrt{2}} E_{LO} e^{j\pi} \\ E_{LO2^+} = E_{LO4^+} = \frac{1}{2\sqrt{2}} E_{LO} e^{j\pi} \\ E_{LO2^-} = E_{LO4^-} = \frac{1}{2\sqrt{2}} E_{LO} e^{j\frac{\pi}{2}} \end{array}\right.$$

because each reflection involves a phase shift of $\pi/2$. The expression for the photocurrent at each photodiode is:

$$I_{PDn^{\pm}} \propto |E_{LOn^{\pm}} + E_{rn^{\pm}}|^2 \tag{3.8}$$

3.2.1 Coherent Detection Algorithm

Our coherent detection receiver needs digital signal processing (DSP) to extract the symbol information (φ_1 and φ_2) from the photocurrents. The use of DSP relaxes the constraints on the local oscillator stability and phase noise, and it is not needed to lock it on the received signal; in other words the coherent mixer doesn't bring the signal to base band but just to an intermediate frequency $\Delta\omega$. This will made the photocurrents proportional to a term $\cos(\Delta\omega t + \Delta\psi(t))$. Through a digital signal processing scheme it is possible to estimate this intermediate frequency and to recover the information hidden in the photocurrents. There are two ways of doing signal acquisition: synchronous and free-running. The first technique uses an analog clock recovery amplifier connected to the analog to digital converters (ADC). In this case the ADCs are driven by this amplifier. This is the traditional way of working, also in direct detection. The second technique is called free-running because it does not require an analog clock recovery. It is well known that, to exploit all the features of signal processing, two samples per symbol are needed (Nyquist sampling theorem). In our setup each balanced photodiode is directly connected to a free-running ADC. We must mention that, for certain schemes, trans-impedance amplified (TIA) photodiodes are used and variable gain amplifiers (VGA) are inserted before ADCs. Our scheme is simpler and we don't see any advantage in using TIA and VGA. However it is important to use very linear devices, hence we prefer not to use electronic amplification. ADCs represent the critical components in the whole setup. State of the art ADCs are barely fast enough for 10 Gbaud QPSK and power consumption is really high ($> 10W$). In the case of free-running ADC we would need, for a 10.7 Gbaud QPSK with polarisation multiplexing (hence, a bit rate of 42.8 Gbit/s), 4 ADCs having at least a sampling rate of 21.4 Gbit/s and an analog bandwith of 10 GHz with 5 bits of resolution. This means a throughput of 856 Gbit/s in the FPGA module. Our experiments are made in off-line mode, this means that we save a short burst of bits from the ADC and we do the signal processing off-line with a Linux PC in a Matlab environment. To record the waveforms, we use a real-time digital sampling oscilloscope from Agilent with

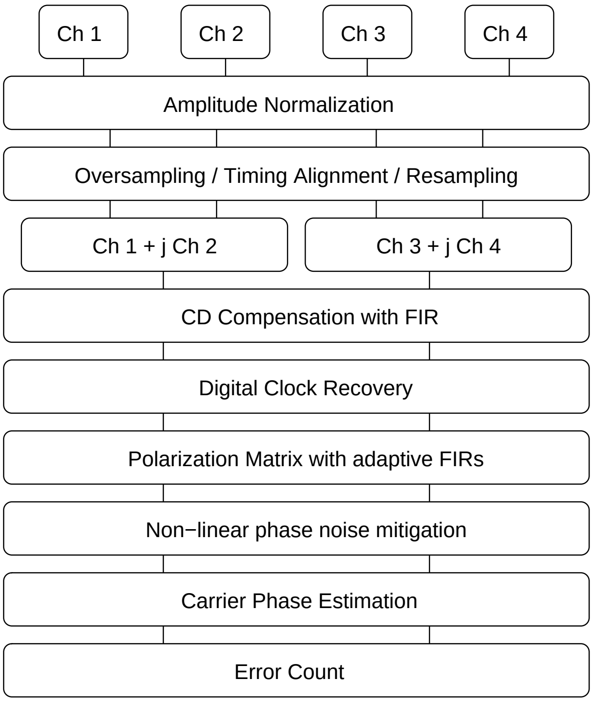

Figure 3.5: Block diagram of the coherent detection algorithm.

4 input channels and 20 Gbit/s sampling rate on each channel. This scope has 5 bits resolution and 8 GHz of analog bandwith. It can save a maximum of 1Msamples (that corresponds to $50\mu s$) per channel. Since we have two samples per symbol and two bits per symbol then 1Msamples corresponds to 1Mbits. This means that if we need a minimum of 10 errors observed to estimate BER, then we can measure a minimum error rate of 1E-5.

The first step of the *coherent detection algorithm* is the signal conditioning. Here we remove the residual DC values from the acquired sequences and we multiply them by a coefficient calculated through a calibration process. Since we will use an adaptive algorithm based on amplitude values, calibration is mandatory.

The second step is timing alignment. Here we should compensate for several timing impairments between the acquired sequences. In particular we have the following delays:

1. The fibres from the two coherent mixers have different lengths
2. The photodetectors have fibres of different lengths

Although in a real system the delays would be reduced to a minimum and compensated for with electrical delay lines, we prefer to adjust the sequences in the digital domain. Through oversampling we can achieve the required resolution in the time domain. Typically we use an oversampling factor of 16 which corresponds to a sampling rate of 320 Gsamples/s, equivalent to a sampling period of 3.125 ps. This period corresponds to the resolution of our timing alignment function. Since ADCs are not synchronous (20 Gsamples/s instead of 21.4 Gsamples/s) we do a two step resampling in order to achieve the desired sampling rate. The first step is a linear interpolation to increase the sampling rate by a factor 1.07 (the ratio between bit rate and scope sampling rate); the second step is downsampling by the same factor as the one used in oversampling, to reach the exact sampling rate of $2 * R = 21.4$ Gsamples/s. This kind of operation is necessary only in our laboratory environment because we do not have the possibility to adjust the ADC sampling rate. The extra-band noise added by this kind of interpolation is negligible.

The third step of the algorithm is dispersion compensation through FIR filter. Given the compensation the receiver should compensate for, we calculate the frequency response of the $H_{disp}(\omega)$ filter and we truncate the inverse FFT at the given number of filter coefficients.

The fourth step is digital clock recovery through one of the many already known numercal solutions. A typical algorithm analyses the sum of the powers of the incoming signals. After a numerical oversampling it is possible to evaluate which sample can be the best central sample. Then the signal can be decimated starting from the estimated best central sample.

The fifth step is the adaptive polar rotation filter matrix based on the constant modulus algorithm (CMA, proposed by Godard in [60]). The principle of this step is to obtain a rotation of the incoming signals state of polarisation (SOP) so that the transmitted one will be recovered. This is done using an adaptive filter based on the algorithm known as CMA. The SOP recovery block, whose diagram is presented in Fig. 3.6, is based on four adaptive filters $\mathbf{h_{a,b}}$ (with $a, b \in \{1, 2\}$). The working principle of the scheme is explained by the following equation:

$$\begin{bmatrix} y_1 \\ y_2 \end{bmatrix} = \begin{bmatrix} h_{1,1} & h_{1,2} \\ h_{2,1} & h_{2,2} \end{bmatrix} \otimes \begin{bmatrix} s_1 \\ s_2 \end{bmatrix} . \tag{3.9}$$

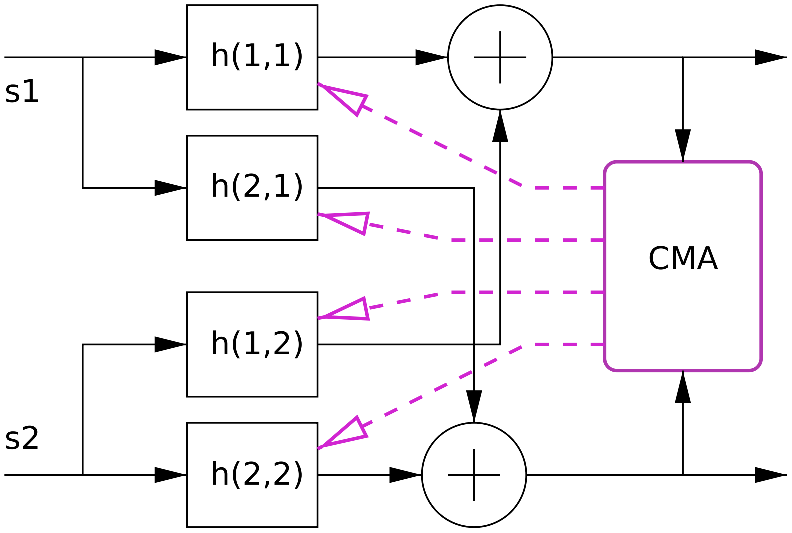

Figure 3.6: Diagram of the SOP recovery filter based on CMA adaptive algorithm.

Filter coefficients $\mathbf{h_{a,b}}$ are complex vectors of length T. It is necessary to use filters in place of scalar values because there is more than just the SOP to compensate for. Many of the effects of the channel on the polarisation of the signals are frequency dependent, so that filters are needed. Ideally, without any effect other than SOP rotation, all the elements of the filters should be equal to zero with the exception of the central ones. This configuration is interesting because, without knowing anything about the channel and its effects on the signals, we can use as initial values the ideal ones. Since they depend on azimuth θ and elevation δ of the SOP, we are free to choose their values. There is no reason to think that there is a preferable initial value so, in general, the configuration $\theta = 0, \delta = 0$ is chosen. Calling $c = \lceil T/2 \rceil$ the central index of the filter vectors, we can write:

$$\begin{bmatrix} h_{1,1}(c) & h_{1,2}(c) \\ h_{2,1}(c) & h_{2,2}(c) \end{bmatrix} = \begin{bmatrix} \cos\theta e^{j\delta} & -\sin\theta e^{j\delta} \\ \sin\theta & \cos\theta \end{bmatrix} \underbrace{=}_{\theta=0,\delta=0} I_2 \tag{3.10}$$

where I_2 is the 2×2 identity matrix. The CMA is heavily dependent on the initial value of the coefficients. It can be shown that changing this choice leads

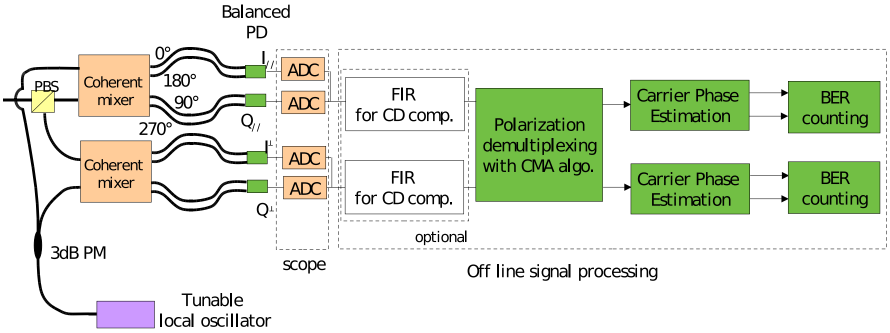

Figure 3.7: Description of the coherent receiver.

to the inversion of the outputs and to different convergence times.

The sixth step is a non linear operation on the signal amplitude. We have implemented this block to mitigate the effects of non-linear phase noise but its use is not mandatory. The implemented function adds a phase rotation proportional to the amplitude of the sample, as in [61].

The seventh block is the carrier phase estimator. This block has to estimate the value of $\Delta\omega t + \Delta\psi(t)$. We have tested several phase estimation algorithms. The method currently used to estimate the carrier phase from the detected phase is derived from the one proposed by Viterbi and Viterbi [62]. According to this estimation method, the digital complex signals are elevated to the 4-th power (2nd for BPSK modulation format) to cancel the phase modulation $\varphi_s \in \{0, \pi/2, \pi, 3\pi/2\}$. The phase of the resulting complex field is obtained by taking its argument and dividing by 4, leading to a carrier phase estimate $\vartheta \in [-\pi/4; \pi/4]$, using the formula:

$$\vartheta = \frac{\angle y^4}{4} \tag{3.11}$$

Last block is the error count block. At first, an hard decision is made on both polarisation states. The thresholds for the hard decision coincide with the axes of the I-Q diagram. Since a differential coding is used, decided symbols are obtained by the difference of the phases with their delayed copies. Finally, the algorithm looks for the beginning of the reference PRBS sequences from the pulse pattern generator for both polarisations and, starting from that point, it counts the errors.

3.3 Experiments on Optical Coherent Detection

In our experiments, PDM-QPSK is obtained by splitting the light from a 100-kHz linewidth laser into its two orthogonal polarisation components. As shown in Fig. 3.3, these components are sent into two distinct QPSK modulators. The modulators are fed with $2^{15}-1$ PRBS at 10.7 Gbit/s, including a 7% forward-error correction (FEC) overhead. They produce two distinct, electrically pulse-shaped streams of symbols, which are polarisation-multiplexed into a polarisation beam combiner (PBC). From the setup described in Fig. 3.3, it can be seen that, compared to singly polarised QPSK at 20 Gbaud, PDM-QPSK does not involve any major hardware upgrade while decreasing the line rate down to 10 Gbaud, which offers the possibility to use standard electronics and optoelectronic components. At the receiver side, two coherent mixers, one for each polarisation state separated by a polarisation beam splitter (PBS), combine the signal with a CW laser, i.e. the (unlocked) local oscillator (LO), as schematised in Fig. 3.7. The mixers are designed to achieve a phase offset of 90° between each of their four outputs, so as to supply the in-phase and quadrature components of the incoming signal. These components are detected by four balanced photodiodes (PD) and connected to the four ADCs of the sampling heads of our free-running oscilloscope in order to produce digitised waveforms corresponding to real and imaginary parts of the beat terms of the incoming signal and the LO. This oscilloscope operates at a rate of 20 Gsamples/s and can store 1 million samples at once (which corresponds to a time slot of 50 μs), simultaneously from all four heads. The bit-error rate (BER) is calculated out of the full 50 μs recordings, through off-line processing in six steps: resampling at twice the symbol rate, possible dispersion compensation through finite impulse response (FIR) filter [50], digital clock recovery, polarisation demultiplexing through 5-tap adaptive filtering based on the constant modulus algorithm (CMA) [60], carrier-phase estimation using the Viterbi and Viterbi algorithm [62], and finally symbol identification. It should be emphasised that polarisation demultiplexing is achieved digitally only, without any manual control, and with the same equipment as that needed for the coherent detection of 20 Gbit/s QPSK data (which would require polarisation diversity anyway).

One of the primary advantages of 40 Gbit/s PDM-QPSK when used with coherent detection is that its sensitivity to noise can get very close to the lowest value recorded among all modulation schemes at 40 Gbit/s. Fig. 3.8

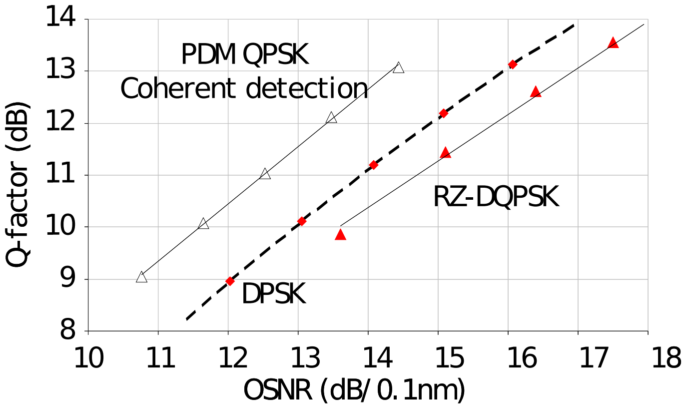

Figure 3.8: Measured OSNR sensitivity of PDM-QPSK versus DQPSK and DPSK at R = 10 Gbaud/s.

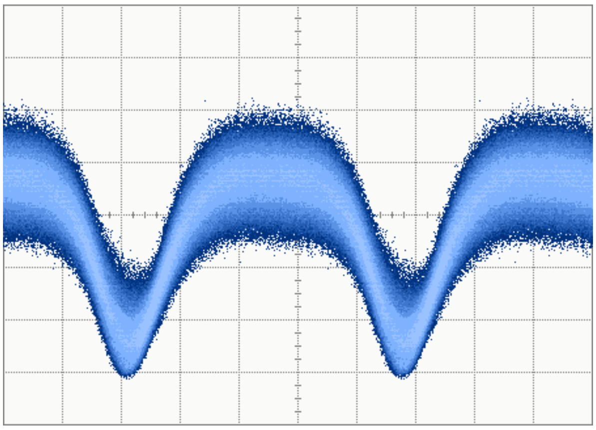

Figure 3.9: Measured launch eye diagram; 20 ms/div on the time axis, 20 mV/div on the vertical axis.

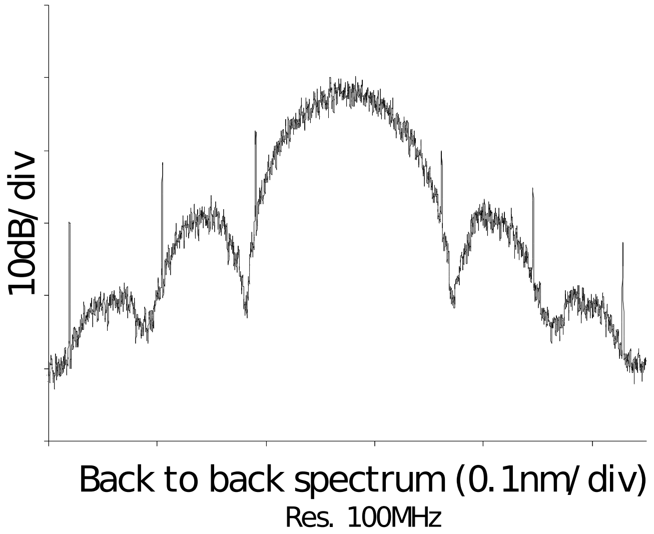

Figure 3.10: Experimental spectrum of PDM-QPSK.

depicts the Q factor of the PDM-QPSK format with coherent detection, versus the optical signal-to-noise ratio (OSNR) normalised to 0.1 nm, as recorded in a back-to-back configuration. The result is compared with a 40-Gbit/s RZ-DQPSK (respectively, DPSK) laboratory equipment based on differential direct detection. We observe a 2-dB (respectively, 1.3 dB) better sensitivity with coherent detection, in line with theoretical predictions. The eye-diagram of PDM-QPSK is also displayed in Fig. 3.9, as well as the spectrum shown in Fig. 3.10, recorded by a 100-MHz-resolution optical spectrum analyser. The central-lobe bandwidth of 40-Gbit/s PDM-QPSK is found almost identical to that of 10-Gbit/s NRZ, which is naturally advantageous for dense WDM channel packing.

3.3.1 Tolerance to linear fibre impairments

The purpose of this section is the assessment of the tolerance of coherent detection to optical filtering and PMD through a performance comparison between singly polarised QPSK and PDM-QPSK signals. The efficiency of the PMD mitigation is also evaluated in the case of large cumulated chromatic

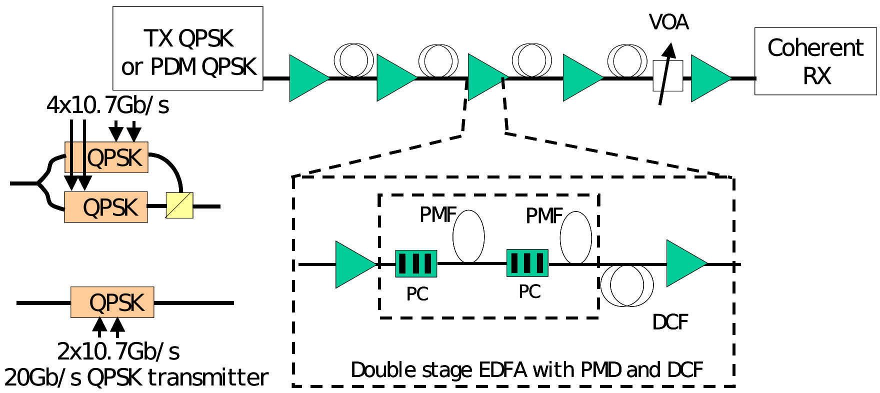

Figure 3.11: Experimental setup used to investigate for the impact of narrow optical filtering and PMD.

dispersion. These experimental results are obtained after 400-km transmission using the experimental setup described next.

Experimental Setup

The test-bed depicted in Fig. 3.11 involves 40 lasers spaced by 100 GHz, which are sent into one modulation equipment fed with $2^{15} - 1$-long words, either with PDM at 40 Gb/s or without PDM at 20 Gb/s, plus 7% FEC overhead. The multiplex is boosted and sent into a typical dispersion-managed link with four 100-km-long spools of standard fibre, separated by dual stage amplifiers. These amplifiers incorporate dispersion compensating fibre (DCF), and possibly two polarisation controllers each followed by a polarisation maintaining fibre (PMF) for PMD emulation. By adjusting a variable optical attenuator at the input of the preamplifier, the OSNR is intentionally degraded at the receiver in order to measure bit error rates in the range of 10^{-3} to 10^{-6}. The central channel is selected by an optical filter and sent to the coherent receiver. In the receiver, two coherent mixers, one for each polarisation component, combine the signal with a CW laser, standing for the (unlocked) local oscillator, and supply the real and imaginary parts of the signal. The signal is then sampled, digitised, stored by sets of 200 000 samples, and processed off-

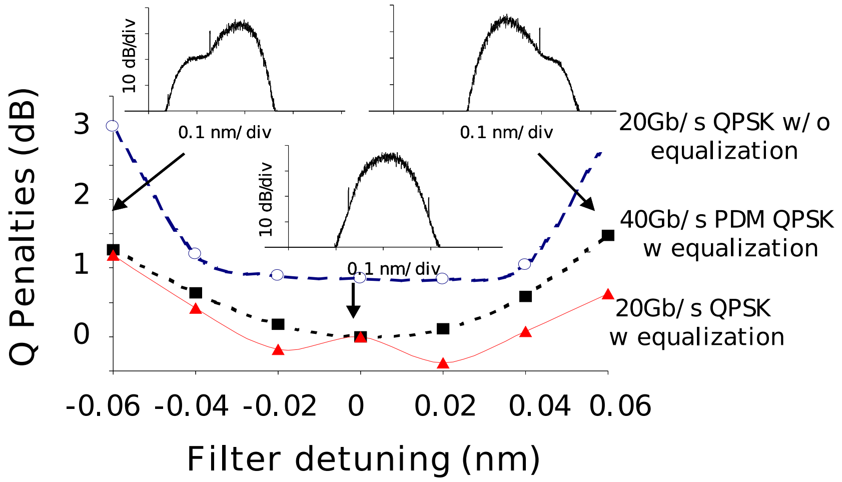

Figure 3.12: Evolution of Q-factor penalties with respect to the filter detuning, for 20 Gb/s QPSK signal with and without equalisation, and also for 40 Gb/s PDM-QPSK with equalisation.

line [51]. Regarding the real throughput of this technique, it is to be noticed that such kind of digital signal processing has already been implemented for real time test-beds [63].

Tolerance to Narrow Optical Filtering

One potentially critical impairment across optical networks is narrow optical filtering resulting from ROADMs. In our experiment, we set the optical filter of the receiver to its minimal bandwidth of 0.125 nm. This would correspond to the effective width of more than 100 concatenated ROADMs designed for 50 GHz channel spacing. The impact of filter detuning on the system Q factor is measured in three system configurations. The first one relies on PDM QPSK at 40 Gb/s, where polarisation demultiplexing is achieved thanks to the constant modulus algorithm (CMA) [50]. CMA also performs blind equalisation, based on a 9-tap adaptive FIR filter. The other two configurations involve singly polarised QPSK at 20 Gb/s, respectively, with and without [64] equalisation from the CMA. Fig. 3.12 depicts the evolution of the Q-factor penalties with respect to the filter detuning obtained for these three system

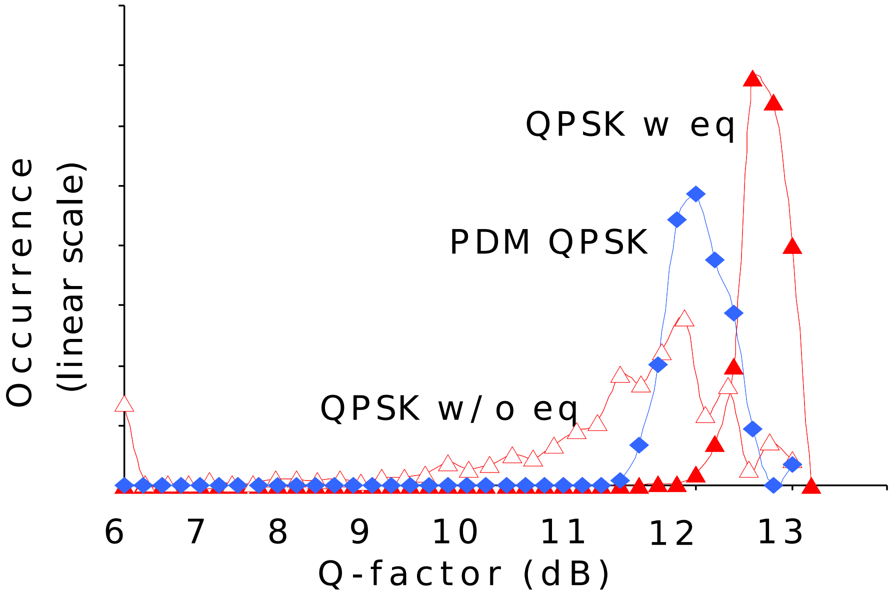

Figure 3.13: Q-factor distributions with 36ps PMD for 40 Gb/s PDM QPSK and 20 Gb/s singly polarised QPSK, with and without equalisation.

configurations. As shown in this figure, without PDM, the CMA is found to improve the Q-factor by ~ 0.85dB when the filter is well centred, and also to improve the signal robustness to filter detuning. Moreover, this robustness is almost unchanged with PDM at 40 Gb/s, assuming equalisation is turned on. Consequently, this result clearly demonstrates that coherent detection with digital equalisation (using CMA) can tolerate filtering functions equivalent to an extremely large number of 50 GHz ROADMs, with or without PDM.

Tolerance to Polarisation Mode Dispersion

Another concern for the implementation of PDM is the tolerance to PMD. To evaluate this tolerance, we have emulated all-order PMD using the scattering model [65] Indeed, two birefringent sections composed of PMF are connected with two polarisation controllers at the interstage of all the dual stage amplifiers. A computer is used to drive the polarisation controllers in order to vary randomly the input state of polarisation in each PMF. The PMF spools used here are composed of five sections with 10-ps differential group delay

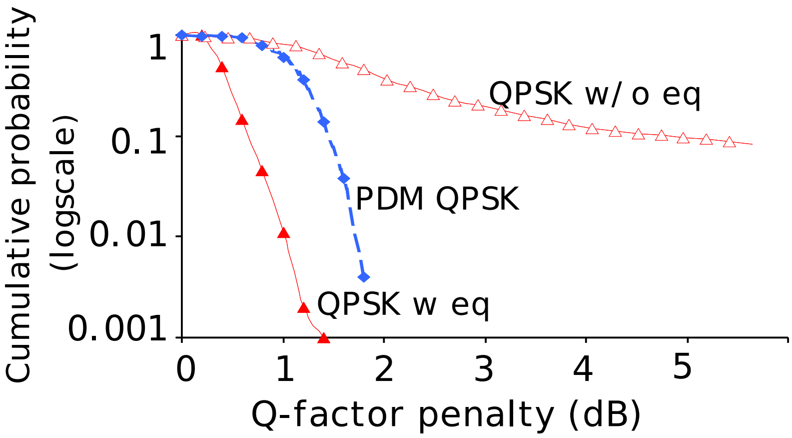

Figure 3.14: Cumulative probabilities penalty with 36ps PMD for 40 Gb/s PDM QPSK and 20 Gb/s singly polarised QPSK, with and without equalisation.

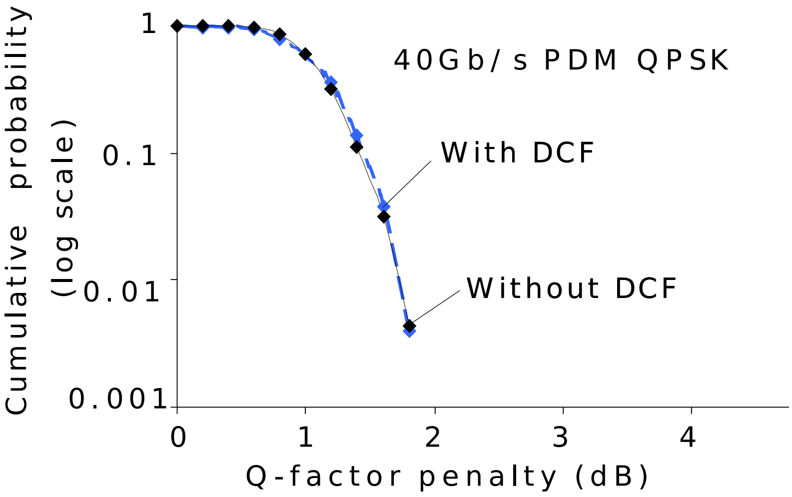

Figure 3.15: Cumulative probabilities with 36-ps PMD for 40-Gb/s PDM QPSK when DCF are removed.

(DGD) and five sections with 13-ps DGD, leading to a total PMD value of 36 ps [66]. Following this setup, the BER is measured for 1000 PMD sample configurations. The OSNR at the end of the link is set to 8.5 dB/0.2 nm for the 20-Gb/s QPSK signal measurement or to 11.5 dB/0.2 nm for the 40-Gb/s PDM QPSK signal, in order to have similar Q-factors. Fig. 3.13 represents the distribution of the recorded Q factors when the 1000 PMD conditions are varied, while Fig. 3.14 depicts the corresponding cumulative probabilities. The same three system configurations as in Fig. 3.12 are investigated. In the histograms of Fig. 3.13, any Q-factor equal or below 6 dB (or any penalty > 6dB) have been counted as 6 dB. When the system is operated with singly polarised QPSK at 20 Gb/s, the system performance appears drastically improved by equalisation from the CMA. Both mean Q-factor is improved and lower tail of the histogram is reduced. To maintain a similar robustness to PMD from 20 to 40 Gbit/s when polarisation multiplexing is implemented, no more than 1 dB extra margin appears to be needed. Therefore, 40-Gb/s PDM QPSK with coherent detection stands as much more resistant to PMD than any other proposed solutions for 40 Gbit/s over a single wavelength, exceeding the tolerance of 10 Gbit/s NRZ. Some PMD mitigation schemes are reportedly less efficient in presence of large chromatic dispersion. Next, we remove all the DCF spools out of the amplifier interstages. 1000 BER measurements are recorded with 40 Gb/s PDM QPSK format, each corresponding to a different PMD condition. A FIR filter is implemented before the CMA algorithm to cope with the large accumulated chromatic dispersion of the link ($\sim$ 6800 ps/nm). In Fig. 3.15, describing the cumulative probabilities of the recorded Q factors as a function of the Q-factor penalties, it can be seen that the Q-factor cumulative probability is almost identical with and without in-line DCF, even if the mean Q-factor was found degraded by $\sim$ 0.6dB without in-line DCF. This result highlights that the efficiency of PMD mitigation is not affected by large accumulated dispersion.

WDM TRANSMISSION EXPERIMENT

We then carry out a WDM transmission experiment over 4080 km with combined emulations of narrow optical filtering and PMD using a recirculating loop, as depicted in Fig. 3.16. Our transmitter involves 40 channels spaced by 100 GHz. Odd and even channels are modulated independently, each with a specific set of QPSK modulators. The loop incorporates eight 65-km-long spans of +D/-D UltraWave fibre, separated by Raman amplifiers and gain

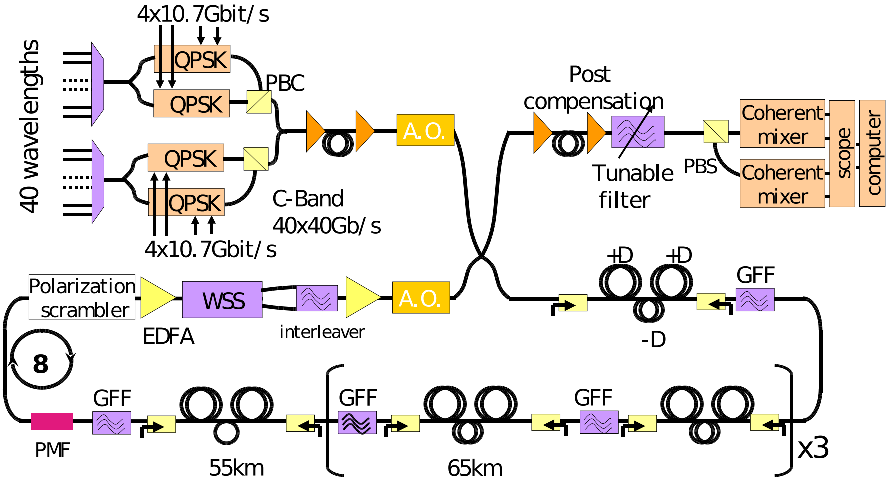

Figure 3.16: Experimental transmission setup with emulations of all-order PMD and narrow optical filtering.

flattening filters (GFF), as described in [67]. Two narrow-filtering elements are inserted at the end of the loop, namely a 50-GHz wavelength selective switch (WSS) and a 50-GHz interleaver, in order to emulate the possible presence of ROADMs in the network. The WSS is also used for gain equalisation. The loop also involves a small section of PMF of variable length, and hence, of variable DGD. The PMF is used to emulate a PMD well in excess of the small 0.8-ps PMD accumulated into the transmission fibre spools. It has been inserted just before a low-speed polarisation scrambler which scrambles at a characteristic time in the range of the loop transit time (2 ms). Therefore, after eight round-trips, the loop behaves very similarly to a eight-section PMD emulator with a PMD equal to $\sqrt{8}$ times the DGD of the PMF [65]. It produces an overall DGD which varies from one recording to the next, but which is almost constant over the 50 μs acquisition time of oscilloscope. Besides, PDL was found to generate up to ±1.5dB relative power variations, and, hence, relative OSNR variations, between the two polarisation components after 4080 km, which is relatively large compared to typical values reported for in deployed systems, but has likely been enhanced by the loop configuration. The performance of the 40 channels after 4080 km is first measured with a PMF of 3-ps DGD. As shown by Fig. 3.17, the Q-factor is measured at 2 dB above

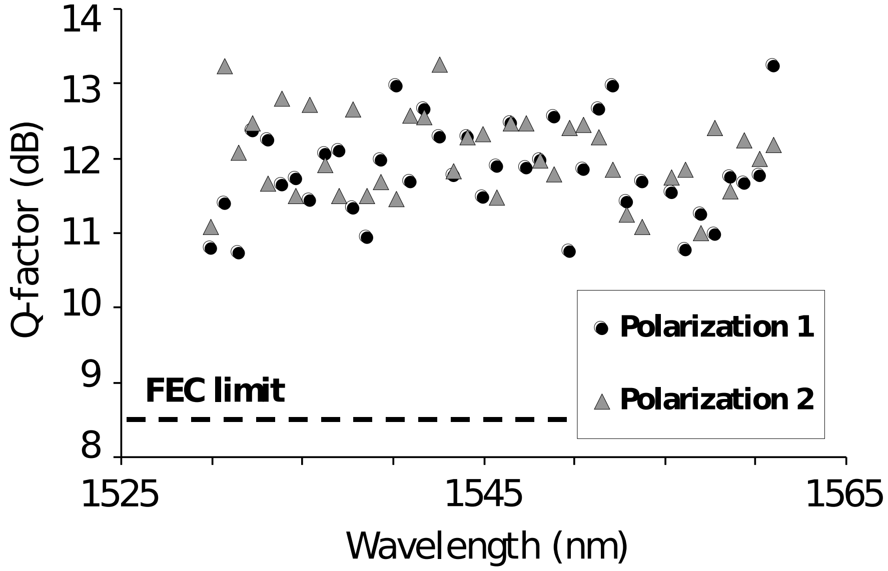

Figure 3.17: Measured Q-factors on both polarisations for all the transmitted channels after 4080 km.

the 8.5-dB FEC threshold across the whole multiplex, over both polarisation components. The variation of performance between the different channels and between the different polarisation components of each channel is mainly attributed to PDL that induces up to ±1.5 dB relative OSNR variations between the two polarisation components. In this experiment, the residual dispersion did not need to be compensated for with any dedicated component, despite large values it reached, between 700 and 900 ps/nm. Note that the tolerance to residual dispersion never exceeds ±150 ps/nm in 40 Gbit/s solutions based on direct direction, ±50 ps/nm being a typical limit. Therefore, the PDM-DQPSK solution with coherent detection advantageously removes the need for the dynamic dispersion compensators found in most of today's commercial 40 Gbit/s transponders. In addition, system suppliers could continue to avoid costly channel-by-channel dispersion compensation at 40 Gbit/s despite the fibre dispersion slope, exactly like at 10 Gbit/s. To further assess the resistance of PDM-QPSK with coherent detection to chromatic dispersion accumulation, we now add sections of dispersive fibre (dispersion-compensating fibre or stan-

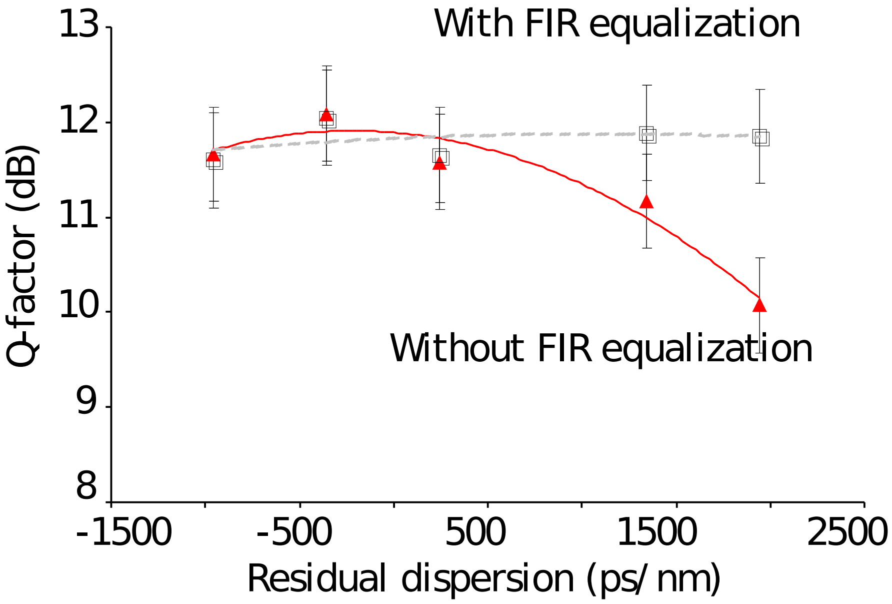

Figure 3.18: Q-factor evolution as a function of residual dispersion with and without the use of a FIR filter inserted before CMA to cope for chromatic dispersion.

dard fibre) in front of the receiver. One typical channel (1544.1 nm) in the multiplex is selected and the impact of the inserted fibre spools on its Q factor is measured, as shown in Fig. 3.18. With the full algorithm involving the FIR filter inserted before CMA to compensate for chromatic dispersion, no significant penalty can be observed in the $-1000 - +2000$ ps/nm range of cumulated dispersion, in accordance with the conclusions of [50]. Another important observation is that, even without the use of this specific FIR filter, the tolerance to cumulated dispersion is well above the standards for direct-detection 40 Gbit/s systems, and even larger than the standards with 10 Gbit/s NRZ, at more than ±1000 ps/nm for 1-dB penalty. This result suggests that a simpler algorithm without FIR filtering inserted before CMA would already provide very good mitigation of dispersion impairments in most transmission applications. It illustrates that our CMA algorithm not only performs polarisation demultiplexing but also excellent blind amplitude equalisation, which has a positive impact against all sources of pulse distortions. Next, we investigate

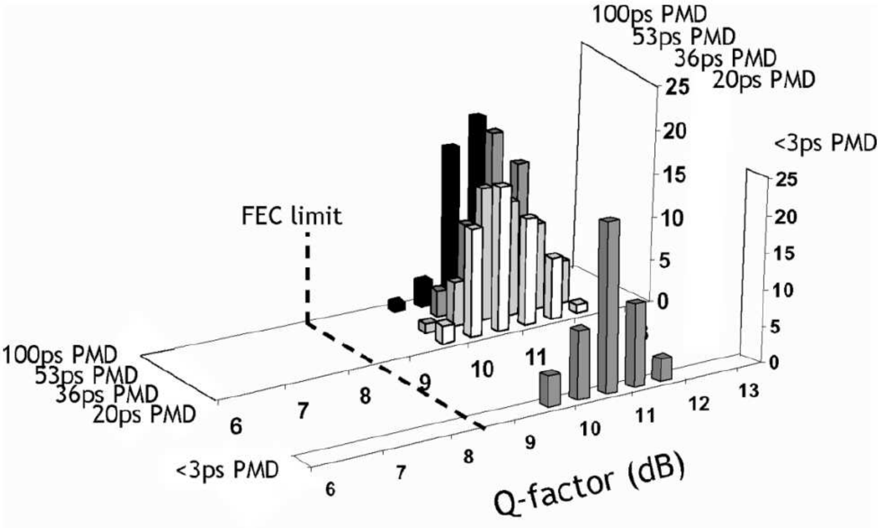

Figure 3.19: Impact of various amounts of PMD on 40-Gb/s PDM QPSK with coherent detection after 4080-km transmission.

further the tolerance of PDM-QPSK with coherent detection to PMD. The PMF DGD is 7, 13, 19, and 36 ps, respectively, to generate an overall PMD of around 20, 36, 53, and 100 ps, respectively, after eight loop round-trips. The impact of the PMF length on the Q factor of a typical channel is measured after 4080 km. For each PMF length, 50 recordings of 100 ksamples are collected and the Q factor is calculated for each of them. Fig. 3.19 shows the Q-factors histograms measured for the different PMD values of 20, 36, 53, and 100 ps, as well as the reference Q-factors histogram measured in the absence of PMF (< 3 ps total PMD). In [51], we reported an upper limit of PMD tolerance of 36 ps. Here, thanks to an upgrade of the polarisation demultiplexing step in off-line processing, this figure demonstrates that the increase of the PMD up to 100 ps does not even alter the Q factor distribution already recorded by propagation in the loop without PMF ($< 3ps$ ps total PMD). Although the number of measured samples is not sufficient to guarantee the system tolerance to 100 ps PMD, it shall be stressed that PMD values of 3 and 12 ps are often considered as an upper limit for 40 and 10 Gbit/s direct-detection systems, respectively. This result highlights the efficiency of the studied technique, despite cumulated PMDs at 40 Gbit/s which exceed the maximum values for conventional 10 Gbit/s NRZ systems. Note also that PMD is here mitigated as fast as the polarisation demultiplexing operation (in the order of 1 μs), i.e., at least three orders of magnitude faster than the best optical PMD compensators. Naturally, further investigations based on a larger number of measurements would be required to accurately estimate the outage probability of coherent-based systems due to PMD and PDL.

3.4 Conclusions

Through this chapter the new generation of optical coherent detectors has been introduced and widely investigated through several different experimental setups. We have demonstrated that polarisation-division multiplexing could offer an attractive alternative to existing 40 Gbit/s solutions, when combined with coherent detection and digital processing, because of its superior resistance to fibre impairments. The impact of linear impairments on QPSK and PDM QPSK signal has been evaluated and it has been demonstrated that the blind equalisation performed by CMA is efficient to mitigate linear distortions. In particular, we have shown that 40-Gb/s PDM QPSK with coherent detection can tolerate filtering functions equivalent to an extremely large number of 50 GHz ROADMs. Moreover, we have shown the extremely large robustness of 40-Gb/s PDM QPSK with coherent detection against PMD. Actually, this 40 Gb/s solution stands as much more resistant to PMD than any other proposed solutions for 40 Gbit/s, even exceeding the tolerance of 10 Gbit/s NRZ. Finally, we have also demonstrated that chromatic dispersion, optical filtering and PMD can be jointly mitigated without any efficiency degradation.

Chapter 4

Impact of nonlinear effects on coherent detection

In order to upgrade optical fibre networks and to provide higher capacities, much attention is paid to investigate high bit rate transmissions with narrow bandwidth signals to increase the spectral efficiency of transmission systems. Thanks to the development of GHz technologies for digital signal processing, 40 Gb/s QPSK associated with coherent detection represent a fascinating technique since it offers better sensitivity to optical noise and enhanced tolerance to linear impairments. In the previous chapter, 40 Gb/s PDM-QPSK with coherent detection has been proposed to take advantage of the tolerance to linear impairments provided by coherent detection while increasing the spectral efficiency. Such a transmission system appears attractive to overlay on DWDM existing 10Gb/s infrastructures, but its tolerance to nonlinearities should be better investigated. At present, there is no knowledge of what are the most impacting nonlinear effects on such a receiver. As a first step towards WDM configuration, in this chapter is presented an experimental investigation on the impact of single channel nonlinear impairments on 40 Gb/s coherent PDM-QPSK. Moreover, as a coherent receiver allows for compensation of large accumulated amount of chromatic dispersion [50], we investigate the impact of dispersion management on nonlinear impairments. Finally, through `optilux`, a numerical simulator developed by Prof. Bononi research group, a numerical investigation of the impact of nonlinear phase noise is presented.

This chapter is organised as follows.

In section 4.1 experimental results shows the impact of nonlinear effects

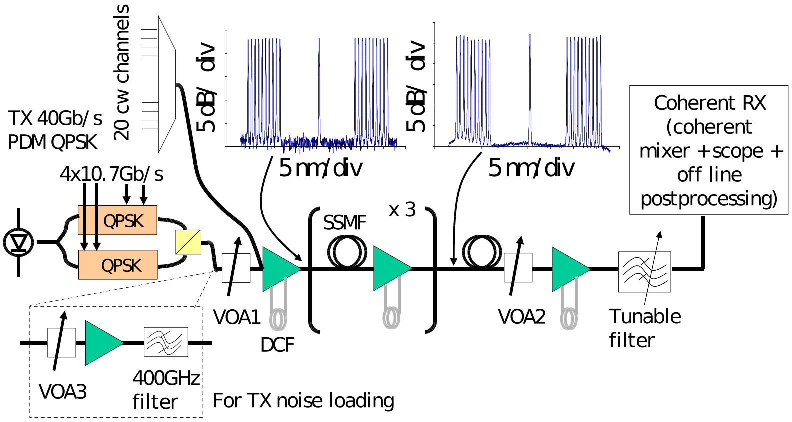

Figure 4.1: Experimental set-up

on 10 GBaud QPSK and 10 GBaud PDM-QPSK. The impact of dispersion management is evaluated by comparing two systems: one with dispersion compensating fibre (DCF) and one with all-digital dispersion compensation.

In section 4.2 a numerical simulation setup is presented. A Monte-Carlo simulation is used to calculate the performance of a multi-span optical system with 10 GBaud and 20 GBaud QPSK modulation.

In section 4.3 numerical results are reported. Single channel and WDM with 7 channel cases are analysed in order to quantify the impact of nonlinear phase noise.

4.1 Experimental Setup

As depicted on Fig. 4.1, the test-bed consists of 2×10 100 GHz spaced lasers combined by one multiplexer. A specific wavelength allocation is used in order to have CW channels only on the edges of the C-Band that maintain consistent amplifier loading. As shown by the optical spectra of Fig. 4.1, in the centre of the C-Band, the studied channel at 1545.72 nm consists of a narrow linewidth laser modulated either with 40Gb/s PDM-QPSK or with 20Gb/s single polarisation QPSK. The modulated signal passes through a Variable Optical Attenuator (VOA) and is combined with the 20 CW lasers before being injected in a booster. The comb is then sent into a 4×100km-

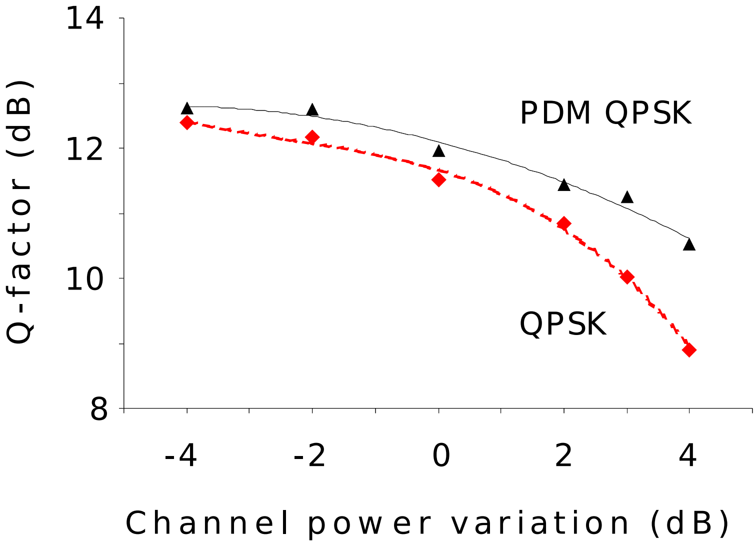

Figure 4.2: Q-factor evolution versus power ratio for PDM-QPSK signal and QPSK signal.

long standard SMF spans system, along which each double stage amplifier can include DCF. By adjusting another VOA at the input of the preamplifier, the OSNR is intentionally degraded at the receiver in order to measure BER in the range of 10^{-3} to 10^{-6}. The signal is selected by a tuneable optical filter and sent to the coherent receiver. The coherent receiver has the same settings used in the experiments of section 3.3.

4.1.1 Tolerance to non linear effect with in line DCF

Constant output power Erbium doped fibre amplifiers (EDFA) are used in the experimental set-up. The output power varies between 16 dBm to 18.7 dBm depending on the EDFA. The power of the studied channel can be varied around the nominal power, defined as the power of each CW loading channel, by adjusting the VOA at the transmitter side. The BER performance of 40Gb/s coherent PDM-QPSK is measured for various channel powers and is compared with the one of 20Gb/s QPSK signal. In both cases a polarisation diversity receiver is used and the original polarisation state recovery is performed by a 9-taps adaptive filtering using CMA. The OSNR at the receiver side was chosen to be 11.5 dB/0.2nm for 40Gb/s PDM QPSK and 8.5 dB/0.2nm for 20Gb/s QPSK signal. These OSNR values corresponds approximately to a back-to-back Q-factor of 13 dB in both cases. Fig. 4.2 shows the evolution of the Q-factor obtained from the measured BER as a function of the channel power variation. Straight line with triangles and dashed line with diamonds represent the performance of 10 Gbaud PDM-QPSK and QPSK respectively. We observe on Fig. 4.2 that both performance curves decrease when the channel power variation reaches 0 dB (e.g. channel power at same level as the one of CW channels). Moreover, PDM-QPSK outperforms single polarisation QPSK, more particularly for channel power variations higher than 3 dB indicating that single polarisation QPSK is more impaired by non linearities. This behaviour could be partially attributed to the 3 dB higher signal power per polarisation of single polarisation format. Therefore, this result demonstrates the interest of coherent PDM-QPSK to fully benefit from the enhanced complexity of coherent receivers while doubling the bit rate and slightly increasing the tolerance to nonlinear effects.

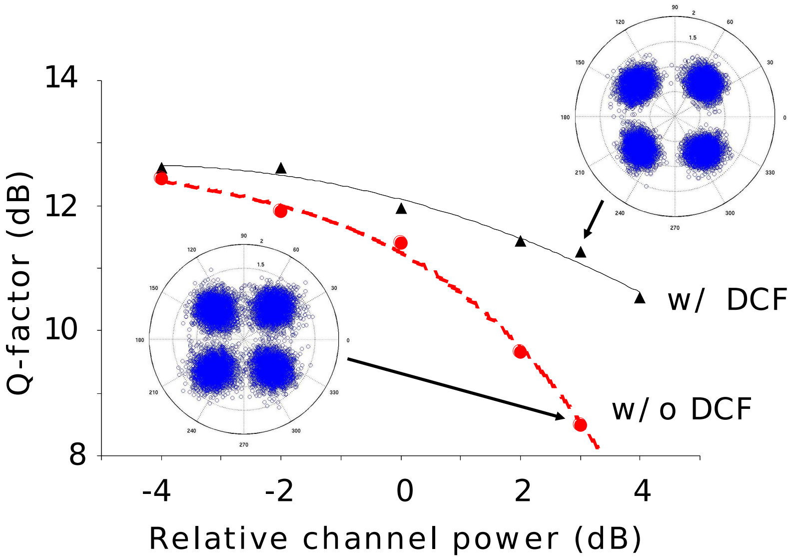

Figure 4.3: Q-factor performance versus channel power variation for 40Gb/s coherent PDM-QPSK, with and without in-line CD compensation.

4.1.2 Tolerance to non linear effects without in line DCF

In a second experiment, in line DCF have been removed and cumulated dispersion is compensated within the coherent receiver by using a 21-tap FIR filters. Fig. 4.3 presents the comparison of Q-factor performance, obtained with and without in-line dispersion compensation, as a function of the channel power variation. We observed on this figure that similarly to the performance of coherent PDM-QPSK versus channel power variation without in-line compensation is drastically reduced when input power becomes higher than 0 dB, similarly to the one obtained with in-line compensation. However, this figure also shows that the difference in performance between systems with and without in-line dispersion increases and becomes clearly larger than 1 dB.

4.1.3 Variation of transmitter OSNR and impact on non linear tolerance.

In a final step, an attenuator is inserted at output of the PDM-QPSK modulator, followed by a single channel EDFA and a 400 GHz-wide optical filter which selects the channel and remove the out of band noise. The previous experimental comparison is repeated with variable OSNR at the transmitter side set to 30 dB/0.2, 20 dB/0.2 and 15 dB/0.2nm, to further assess the tolerance to non linear effects of coherent PDM QPSK with and without in-line dispersion compensation. Experimental results are depicted on Fig. 4.4. Fig. 4.4.a shows that in the presence of dispersion management, the performance of coherent PDM-QPSK tends to decrease with the increase of nonlinear phase noise (NLPN), with penalties up to 2 dB. On the contrary, Fig. 4.4.b shows that uncompensated transmission gives stable performance whatever the increase of NLPN. Although this can be interpreted as a strong point of uncompensated systems it should be noted that the system with DCF is the one with the best absolute performance. Moreover, in Fig. 4.5 there is a curve that represents the difference in Q-factor when the nonlinear mitigation algorithm [61] is turned on. This processing can improve the Q-factor of 1 dB maximum and it is clearly visible in the constellation represented on the graph that the characteristic “beam” shape due to nonlinear phase noise disappear.

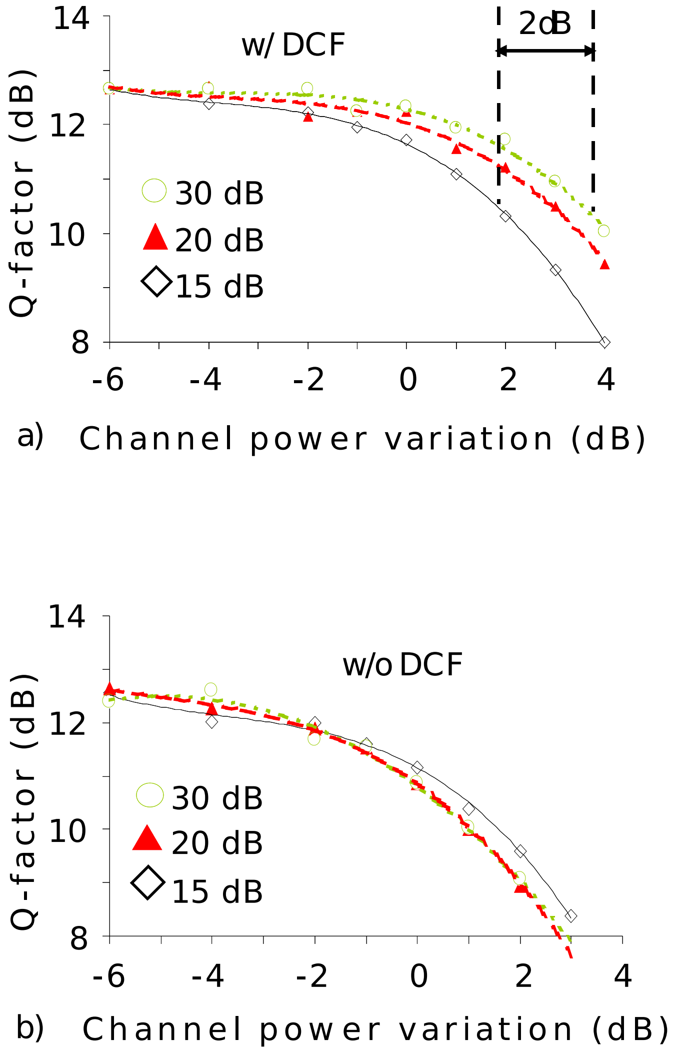

Figure 4.4: Q-factor performance versus channel power variation for various OSNR of 40Gb/s coherent PDM-QPSK, a) with and b) without in-line CD compensation.

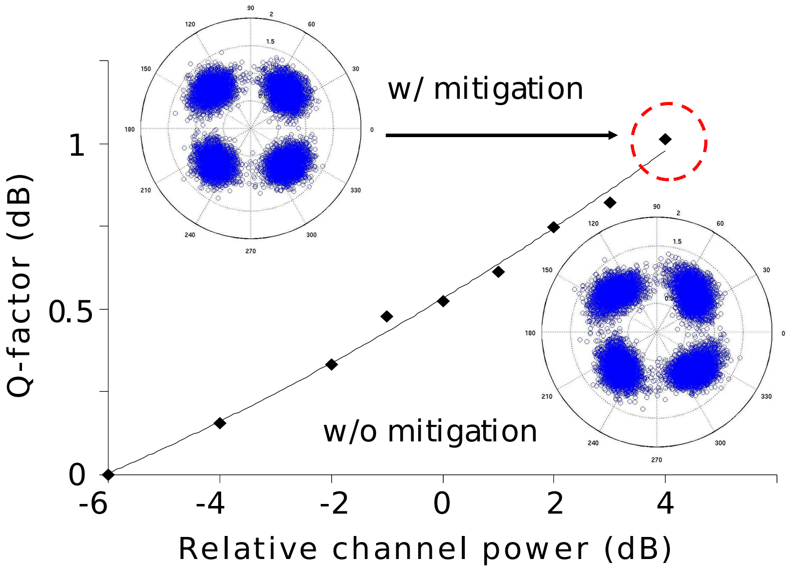

Figure 4.5: Q-factor improvement thanks to electronic nonlinear mitigation versus channel power variation. The constellation represented in the figure shows the “beam” shape that disappear after the digital processing.

4.2 Simulations parameters

The work reported in this section regards some simulation results obtained when the optical simulator `optilux` [58] is used with an optical coherent detector. Among all the aspects involved in a numerical simulation, the cost of the simulation is one of the most important since it can make the difference between simulations that can be run and the ones that are undoable. The most critical operation, from this point of view, remains the propagation along the fibre. In fact propagation is the most costly operation in terms of required time. Simulation with `optilux` or any FFT-based simulator are strongly impacted by the length of the used PRBS sequence. Moreover, all the results presented in this section are obtained through a Monte-Carlo approach, this means that in general, to obtain a single result, it is necessary to run several times the same optical simulation changing the seeds of the random noise or bit generators. The length of the simulated sequence with the unique field

Description	Parameter	Value
Minimum number of MC runs	N_{MC}	16
Maximum relative error	rel_err	0.1
Confidence interval	C.I.	99%
Number of transmitted symbols	N_{SYMB}	2^{10}
Number of samples per symbol	N_T	32
Number of polarisations	N_{POL}	1/2
Symbol rate [GBaud]	symbrate	10/20
Channel spacing [nm]	spac	0.4
Central wavelength [nm]	lambda	1550
Laser linewidth [MHz]	linewidth	1
Electrical Pulse type		raised cosine
Pulse duty cycle	duty	1
Pulse roll-off	roll	0.2

Table 4.1: Default parameters used for the simulation with `optilux`.

approach is $L = N_T * N_{SYMB} * N_{POL}$ while in the separate fields approach it is $L = N_{CH} * N_T * N_{SYMB} * N_{POL}$, where N_T is the number of samples per symbol, N_{CH} is the number of channels, N_{SYMB} is the number of transmitted symbols, and N_{POL} is the number of transmitted polarisations. In the first case the number of samples should be increased in order to enlarge the frequency range of the simulation. If the number of samples is not sufficiently large the channels that are close to the edges could be lost due to aliasing effects. In the second case any channel propagates separately hence there is no need to change the number of samples N_T. The problem is that given N_{CH} channels the simulator has to calculate N_{CH} separate propagations, so the calculation time increases linearly with the number of channels.

4.2.1 Monte Carlo parameters

All the simulation results reported in this chapter are obtained with the Monte Carlo method with several iterations of the same configuration by changing the noise samples. The parameters to be chosen are the ones related to the stop criterion. In order to choose when to stop the Monte-Carlo loop, the relative error of the cumulated quantity should be monitored.

Each run performs the BER estimation over N_{BIT} bits. So in the $k-th$ run we have:

$$B_k = \frac{1}{N_{BIT}} \sum_{i=1}^{N_{BIT}} E_i \tag{4.1}$$

where E_i is an error indicator, which is 1 in case of error on the $i-th$ bit of the $k-th$ run and 0 otherwise. We want to estimate the mean value η_E of the random indicator E, i.e. the bit-error rate, through the averaging $\overline{B}$ over N_{MC} runs:

$$\eta_E \simeq \overline{B} = \frac{1}{N_{MC}} \sum_{k=1}^{N_{MC}} B_k = \frac{1}{N_{MC}N_{BIT}} \sum_{i=1}^{N_{MC}N_{BIT}} E_i \ . \tag{4.2}$$

Since the variance σ_B^2 of this random variable is unknown, it should also be estimated. The unbiased and consistent variance estimator is (from [68], eq. (9-13)):

$$s^2 = \frac{1}{N_{MC}-1} \sum_{i=k}^{N_{MC}} (B_k - \overline{B})^2 \tag{4.3}$$

For large N_{MC} we can approximate σ_B^2 with s^2. Then the approximate confidence interval for the mean value η_B is (from [68], eq. (9-17)):

$$\overline{B} - t_u \frac{s}{\sqrt{N_{MC}}} < \eta_B < \overline{B} + t_u \frac{s}{\sqrt{N_{MC}}} \tag{4.4}$$

where t_u is the u-th percentile of the Student-t distribution with $N_{MC}-1$ degrees of freedom[1]. For $N_{MC} > 30$ the approximation $t_u \simeq z\sqrt{\frac{N_{MC}}{N_{MC}-2}}$ holds, where

$$\begin{cases} z = 1 & \text{C.I} = 68\% \\ z = 2 & \text{C.I} = 95\% \\ z = 3 & \text{C.I} > 99.7\% \end{cases} \tag{4.5}$$

is the $u-th$ percentile of a Gaussian distribution and it depends on the desired confidence. We will stop the simulator when the relative error ε_B will be below the desired threshold, usually 20%. The relative error is:

$$\varepsilon_B = \frac{t_u \frac{s}{\sqrt{N_{MC}}}}{\overline{B}} \leqslant 0.2 \tag{4.6}$$

---

[1] The Student-t distribution coefficients are employed in place of Gaussian coefficients because there is correlation between the estimated mean value and the estimated variance.

At each iteration the estimated variance and mean value of the random variable are updated and the relative error is calculated. The simulation stops when the desired relative error is obtained.

Sometimes it can happen that this technique fails. In fact, if the first iterations returns the same number of counted errors, then the calculated variance can be zero. This means that it will be below any possible threshold and the simulator will stop and will return a false result. In order to grant the good operation a second check is added: the simulator has a minimum number of iterations. This minimum number grants that the realisation of the indicator B will differ and that the estimated relative error has a meaningful value. All the simulations use a Monte-Carlo approach to estimate the error rate. Every run of the MC algorithm generates new noise samples that are added to the signal through noisy optical amplifiers or directly inside lasers (as phase noise). When there is more than one channel the bit pattern of the adjacent channels is also a random variable. Then the error rate is calculated as per equation (4.2). Whenever there are no random quantities involved in the propagation it is possible to save a huge amount of time by storing the received field and by running the iterations on the received field without redoing the propagation. In the table 4.1 there is a list of default parameters used in the simulation with the coherent detection.

4.2.2 Sources

The bit pattern is generated through the `bit_pattern()` function and the default pattern type is the De Bruijn sequence with length $\mathrm{N_{SYMB}}$. The sequence length has to be larger than the memory of the system. In our case there are several elements with memory: the fibre (through its dispersion), the filters, and the digital receiver algorithms. In particular, this last element, can be the one with the highest memory. In fact the frequency estimation and the phase estimation, both based on the Viterbi and Viterbi algorithm [62], could have a large memory and the adaptive filters of the polarisation demultiplexing algorithm have virtually an infinite memory (see section and table for more details). The default value reported in table 4.1 has been chosen accordingly to the other default parameters but should be changed if the other values get modified.

The electrical pulse is a “raised cosine” with roll-off `roll` and will be used as an input for the `opticalmodulator()` function which models the behaviour of a Mach-Zhender IQ modulator.

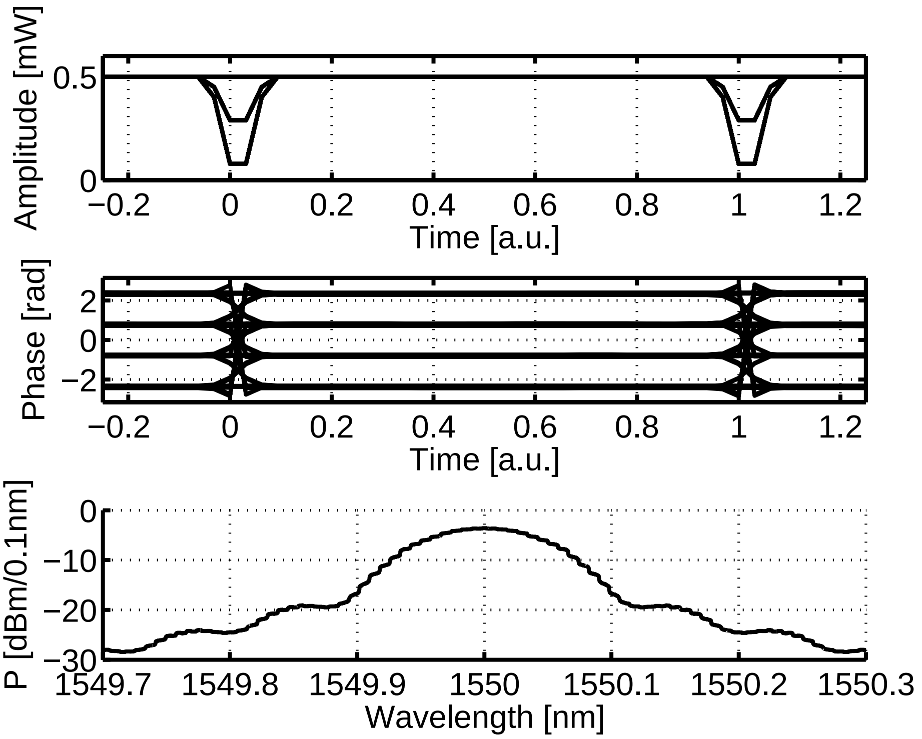

Figure 4.6: QPSK modulation eye and spectrum with default parameters. The first two figures represent the amplitude and phase eye. The bottom figure represents the optical spectrum as it would look like through an optical spectrum analyser with a resolution bandwith of 0.1 nm.

The laser source is modeled as an ideal WDM laser carriers with spacing `spac` and central wavelength `lambda`. As an optional parameter is possible to specify the laser linewidth but modeling of laser source with a given linewidth presents a problem. Since `optilux` is an FFT-based simulator, all the sequences must be periodic in the time domain. Laser source with phase noise cannot be correctly modeled with such an assumption. Phase noise is a Wiener process, which means that is a Gaussian non stationary process with independent Gaussian increments. The total number of noise samples is $N_S = N_T * N_{SYMB}$. Instead of generating N_S independent Gaussian increments, we have chosen to generate $N_S/2$ increments. The second half will

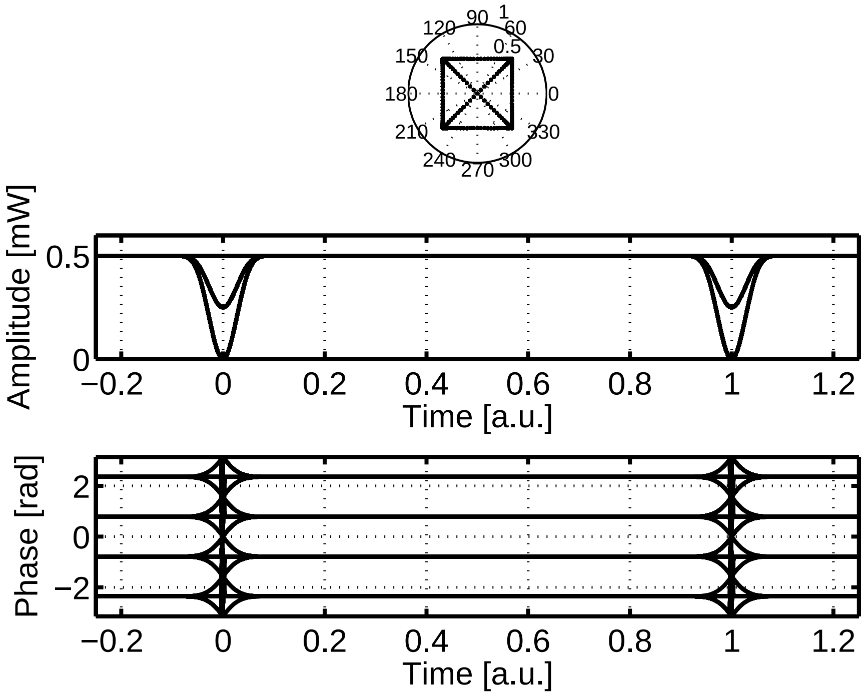

Figure 4.7: QPSK modulation eye with oversampling. The top figure represents the constellation with the transition paths on complex plane. The other two figures represents the amplitude and phase eye.

be calculated as the first half with an inverted sign. In this way we are sure that the sequence is periodic because it will always return to zero. In order to break the visually disturbing symmetry of the phase noise realisation, all the increments are shuffled before calculating the noise with the `cumsum()` function.

All the optical modulator impairments (although programmed in `optilux`) are not activated and the extinction ratio is ideal. In general with single channel simulation the sequence is sampled with N_T=32 samples per symbol. In Fig. 4.6 the eye and the spectrum of the optical signal at the output of the Mach-Zehnder modulator are represented. In Fig. 4.7 the same signal is oversampled by a factor of 8 and the constellation and the eyes are represented.

Description	Parameter	Value
Receiver Type	rx.rec	'coherent'
PDM modulation	rx.pdm	false
Optical Filter Type	rx.oftype	'gauss'
Optical Filter Bandwidth	rx.obw	1.9
Electrical Filter Type	rx.eftype	'bessel5'
Electrical Filter Bandwidth	rx.ebw	0.65
Local Oscillator Power [dBm]	rx.lopower	0
Local Oscillator Detuning [Hz]	rx.lodetuning	100E6

Table 4.2: Default parameters for the coherent receiver.

Description	Parameter	Value
Work at baudrate (inside DSP)[2]	dsp.baudrate	false
Apply ADC quantisation	dsp.applyadc	false
Number of bits of the ADC	dsp.adcbits	5
Sampling rate of the ADC [bitrate]	dsp.samplingrate	2
Digital Dispersion Compensation (DDC)	dsp.applydcf	false
Dispersion to compensate for [ps/nm]	dsp.dispersion	4000
Number of symbols used by DDC	dsp.ndispsym	16
Apply nonlinear mitigation function	dsp.applynlr	false
Apply polarisation demultiplexing	dsp.applypol	false
Pol. Demux method	dsp.polmethod	'Godard'
Modulation Order[3]	dsp.modorder	2
Averaging symbols for freq. estimation	dsp.freqavg	1001
Averaging symbols for phase estimation	dsp.phasavg	7
Power order for phase estimation	dsp.poworder	2

Table 4.3: Default parameters for the digital signal processing of the coherent receiver.

4.2.3 Receiver

The coherent receiver has a coherent mixer, also know as 90° hybrid. The receiver parameters refers to the optical filter, the post compensating fibre, the electrical filter after the photodiodes and the local oscillator. All the parameters needed by the receiver function `receiver_cohmix()` are stored in a structure rx (see table 4.2). This parameters regards the optical side of the coherent receiver. As already mentioned this receiver is based on a strong digital signal processing so the electronic side of the receiver has many parameters too.

The digital signal processing for the coherent detector (programmed in the `optilux` function `dsp4cohdec()`) has parameters regarding the analog to digital converters (ADC) such as the possibility to add the typical ADC quantisation over a variable number of bits and an adjustable sampling rate that could be different from the symbol rate. The whole receiver could work basically in two ways: at the baudrate, sampling one samples per symbol, or in over-sampling mode, sampling two samples per symbol. With two samples per symbol it is possible to recover all the linear impairments and it is the default operational mode that has been used in the following simulations. Then the DPS could apply an FIR filter to compensate for chromatic dispersion (CD) but in these simulations the CD has been compensated optically. The last two important stages of the digital receiver are the polarisation demultiplexing algorithm and the frequency and phase estimators. These are the main causes of receiver memory. The default value is to keep the polarisation demultiplexer turned off and to recover the original state of polarisation optically in an ideal way (works in simulation only). From table 4.3, the frequency estimator uses 1001 symbols and the phase estimator uses 7 symbols.

At the end of the digital receiver the estimated symbol phase is translated into a couple of bits by hard detection where the axis act as thresholds. The bits are stored in a matrix with size $\mathrm{N_{SYMB}} \times 2$ and this matrix is processed by a decoding function that performs the differential decoding. The calculated bit error rate refers to the decoded sequence, which has $2(\mathrm{N_{SYMB}} - 1)$ bits.

4.3 Results

In this section are presented the results obtained with the `optilux`simulator. The parameters used to obtain the results presented in the following sections are summarised in the tables and some lines of code, taken from the scripts, are presented in order to show the way it works

4.3.1 Sensitivity

For this simulation the following script has been used in order to generate the field at the receiver:

```
reset_all(Nsymb, Nt, Nch, Npol,'sensitivity','noprint');
pat_i   = bit_pattern('prbs', 1);
pat_q   = bit_pattern('prbs', 2);
elec_i  = intensitymod(2*pat_i-1,symbrate,'cosroll',duty,roll);
elec_q  = intensitymod(2*pat_q-1,symbrate,'cosroll',duty,roll);
E       = lasersource( Pavg, lambda, spac, linewidth );
opticalmodulator(E,'Qpsk', elec_i, elec_q );
savefield('rx_field');
```

where Pavg = 0 dBm. Also if there is no propagation, there is no need to run these instructions more than once since the noise is added at the receiver. So, in this case, the Monte-Carlo algorithm loop is applied to the receiver only. In this loop a noisy optical amplifier adds noise to the previously saved signal and then signal detection and error count calculation are performed. A chunk of the output log would look like this:

```
OSNR:6.00;BER:6.84e-03;Errors:2268;Rel. Error:0.1;MC runs:162
OSNR:6.50;BER:3.84e-03;Errors:2226;Rel. Error:0.1;MC runs:283
OSNR:7.00;BER:2.20e-03;Errors:1834;Rel. Error:0.1;MC runs:408
OSNR:7.50;BER:1.11e-03;Errors:1978;Rel. Error:0.1;MC runs:874
 . . .
```

The output of the simulator shows that in this case a relative error of 0.1 corresponds to 2000 errors on average. This simulation has an average execution time of 167 μs per run on a 1.6 GHz Intel Centrino CPU. This simulation has been launched twice: for a symbol rate of 10 GBaud and 20 GBaud. The results are reported in Fig. 4.8. Since all the involved quantities are normalised to the symbolrate it is not surprising that the two curves are identical and simply translated by 3 dB on the OSNR axis. In a recent paper by Ip and Kahn [69] there the topic of the feed-forward phase estimation filter is addressed. These two authors explain very clearly the importance of the ratio between the variance of the phase noise and the variance of the additive noise on the choice of the estimator filter. Also if the proposed optimal filter is an approximation of the Wiener filter, it is possible to understand that

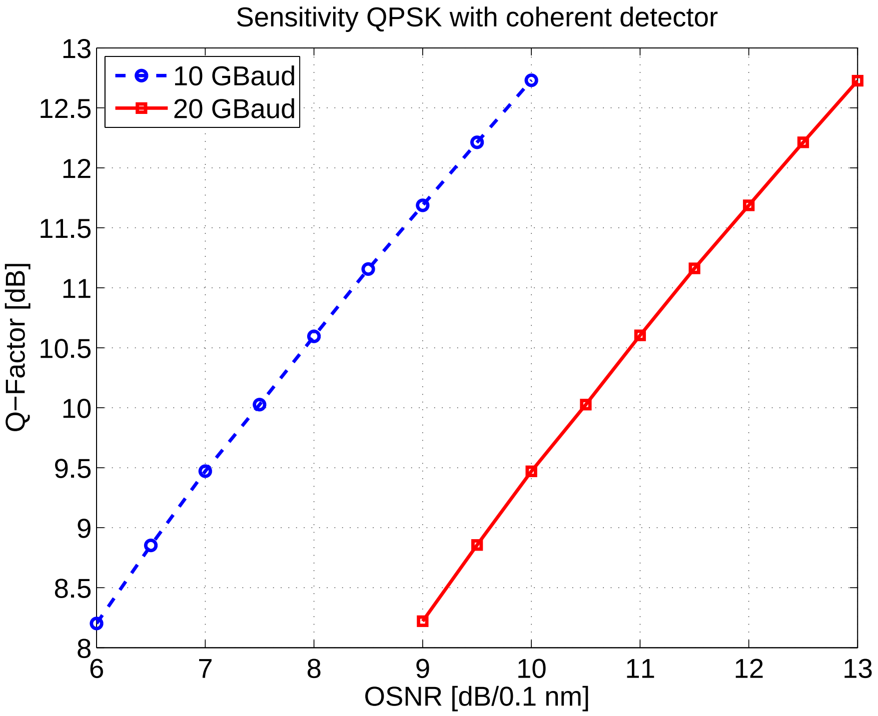

Figure 4.8: Results from sensitivity simulation for 10 GBaud (dashed) and 20 GBaud (solid) systems.

a predominance of the phase noise demands for a short filter and viceversa. This concept was already know thanks to the experimental works done in Alcatel-Lucent laboratory. Since in our sensitivity simulation the linewidth of the laser, which is the only source of phase noise, is kept constant while the OSNR is the variable parameter we are varying the ratio between these two noises. For this reason each point of the curve of Fig. 4.8 has its own optimum value for the phase estimation filter. The impact of a non optimal choice has already been studied and since it is not very pronounced in this simulation all the parameters regarding the Viterbi and Viterbi estimators have been kept constant to a good compromise value(see table 4.3).

Description	Parameter	Value
SMF length [m]	smf.length	100E3
SMF attenuation [dB/km]	smf.alphadB	0.2
SMF effective area [μm^2]	smf.aeff	80
SMF nonlinear index	smf.n2	2.5e-20
SMF wavelength [nm]	smf.lambda	1550
SMF dispersion [ps/nm/km]	smf.disp	17
SMF slope [ps/nm^2/km]	smf.slope	0.057
DCF attenuation [dB/km]	dcf.alphadB	0.6
DCF effective area [μm^2]	dcf.aeff	20
DCF nonlinear index	dcf.n2	2.7e-20
DCF wavelength [nm]	dcf.lambda	1550
DCF dispersion [ps/nm/km]	dcf.disp	-100
DCF slope [ps/nm^2/km]	dcf.slope	0
Maximum linear step [m]	dzmax	20000
Maximum nonlinear step [rad]	dphimax	0.005
Residual dispersion [ps/nm]	dres	100
OSNR at the receiver [dB/0.1 nm]	osnrrx	8 (or 11@20GBaud)

Table 4.4: Default parameters for transmission along 2000 km of SSMF.

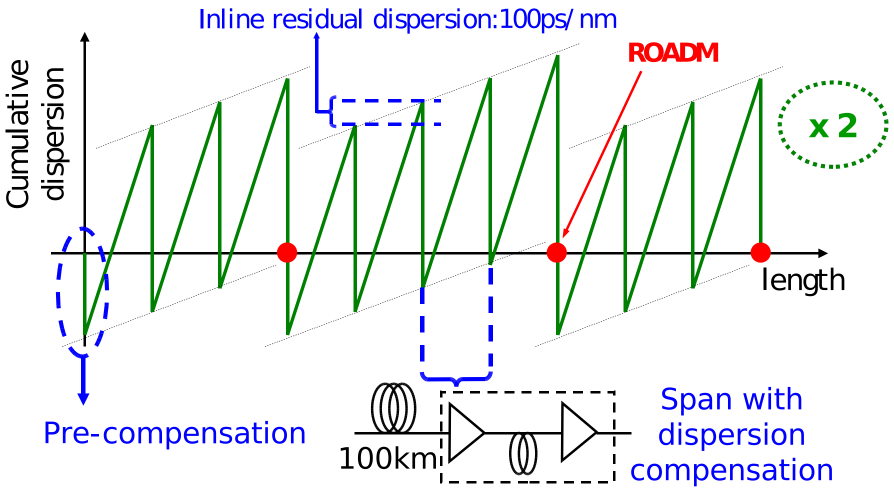

Figure 4.9: Map of the fibre system. The residual dispersion D_{RES} is 100 ps/nm.

4.3.2 Single channel transmission

The propagation of a single channel requires more parameters to be set. During the single channel transmission it is important to estimate the memory of the transmission system and to choose a sufficiently long PRBS sequence. The transmission line is a doubly-periodic map where the single span is formed by 100 km of standard single-mode fibre (SSMF) followed by some dispersion compensating fibre (DCF) as in Fig. 4.9. The length of the DCF is calculated in order to have a desired amount of residual dispersion D_{RES}. The script source code that implements the propagation is the following:

```
mapvector = [ 3 4 3 3 4 3 ];
for k = 1:length(mapvector)
     fiberpmd(pre,'g--');
     for q = 1:mapvector(k)
          fiberpmd(smf, 'gs-');
          fiberpmd(dcf, 'gs-');
          ampliflat( Gedfa,'gain', opt_amplitx );
     end
     roadmpostcomp.disp = -(pre.disp + q .* dres);
     fiberpmd(roadmpostcomp ,'g--');
```

```
end
ampliflat( -PtxdBm, 'gain', opt_amplrx);
```

where map vector describes the periodicity of the map. The numerical modeling of the fibre is done by the function `fiberpmd()`. It takes into account the nonlinear effects in the SSMF and DCF only while for pre- and post-compensating fibre (`pre` and `roadmpostcomp`) nonlinear effects are neglected.

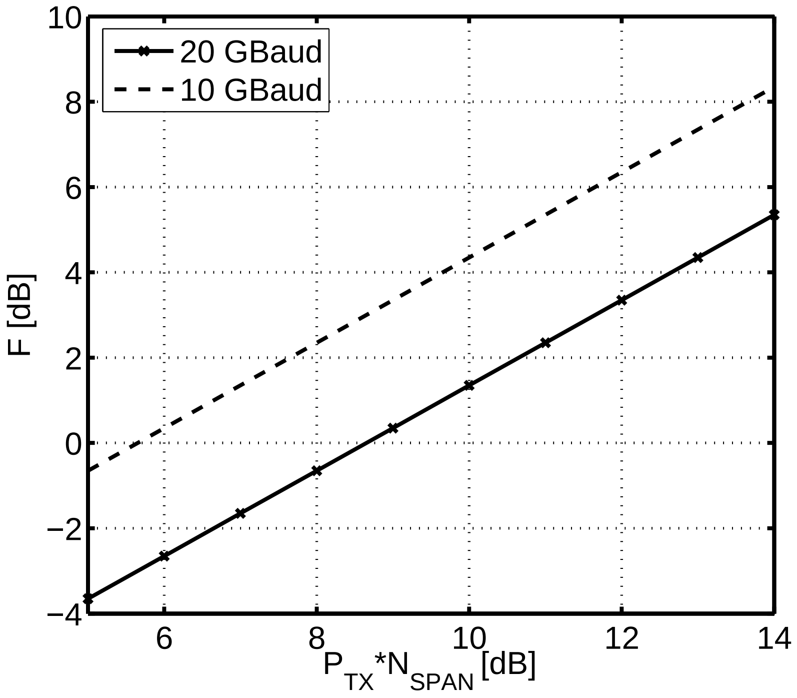

Figure 4.10: Noise Figure of the amplifier in the transmission line: 10 GBaud (dashed) and 20 GBaud (solid) systems.

This script is inserted inside a `for` loop in order to test different values of the injected power $P_{TX,dBm}$. The simulations are run with nonlinear phase noise (NLPN) and without it. Running a simulation with NLPN means that the noise figure F (in [dB]) of the amplifier after the DCF is selected with this equation:

$$F_{dB} = P_{TX,dBm} - 57.954 - 10Log_{10}(G_{LIN} - 1) - 10Log_{10}(N) - OSNR \quad (4.7)$$

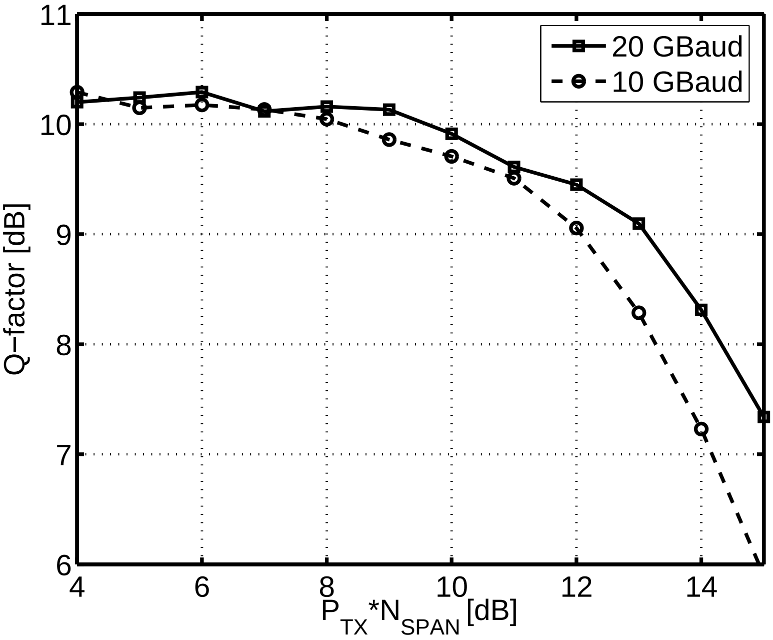

Figure 4.11: Results from single channel propagation with nonlinear phase noise simulation for 10 GBaud (dashed) and 20 GBaud (solid) systems.

where G_{LIN} is the linear gain of all the EDFA, N is the number of amplifiers and $OSNR$ is the desired OSNR at the receiver (expressed in [dB/0.1nm]). While running the simulation without NLPN means that the amplifiers along the transmission line are noiseless and the noise is added by the last amplifier, at the receiver side, in order to have the desired OSNR.

The results for the case without NLPN are reported in Fig. 4.12 and the results for the case with NLPN are reported in Fig. 4.11. The dotted curves are for 10 GBaud and the solid curves are for 20 GBaud. It is clear from those figures that the NLPN has more impact on the slowest symbol rate. This is an interesting aspect that this simulation has put in evidence. Unfortunately the formula of equation 4.7 creates a direct dependence of the noise figure on the injected power. This means that in general the chosen value for the noise figure could be far from a realistic value. In particular, low power demands for an excessive low noise figure and high power for an excessive high value. High

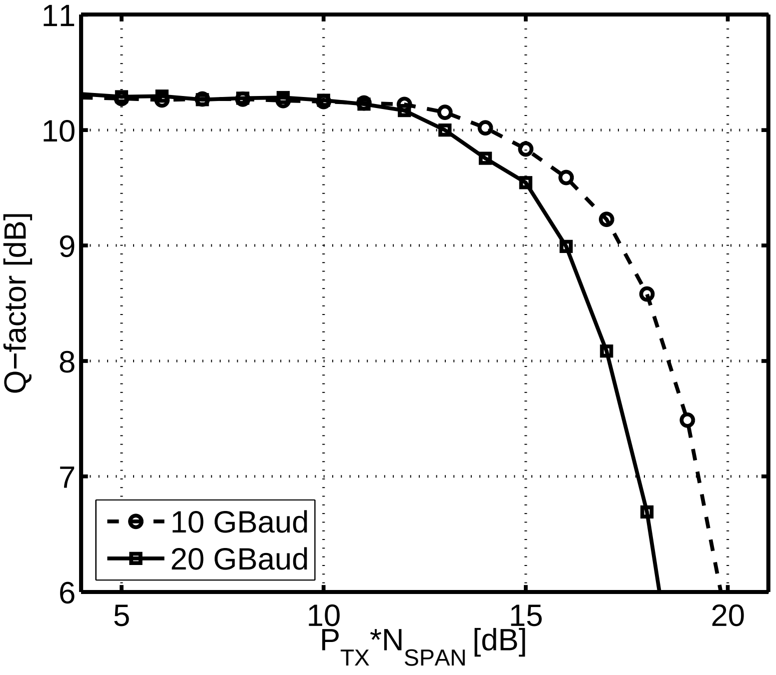

Figure 4.12: Results from single channel propagation without nonlinear phase noise simulation for 10 GBaud (dashed) and 20 GBaud (solid) systems.

power are overestimating the effect of nonlinear phase noise. From Fig. 4.10 it is possible to see that in the range of powers that has been used in the simulation of Fig. 4.11 the value of the noise figure is almost always below a realistic value. In fact if we consider that a dual stage EDFA has typically a noise figure of 6 dB, then only the last two values of the 10 GBaud curve have a higher noise figure. What happens is that the majority of the simulated cases consider amplifier with a better-than-ideal noise figure. In other words, the Q-factors shown in Fig. 4.11 will be hardly reached. It should be noted that with this method the 10 GBaud case interacts with twice the noise power with respect to the 20 GBaud case. For this reason this measure should not be considered a valid support for a comparison between the 10 GBaud and the 20 GBaud systems.

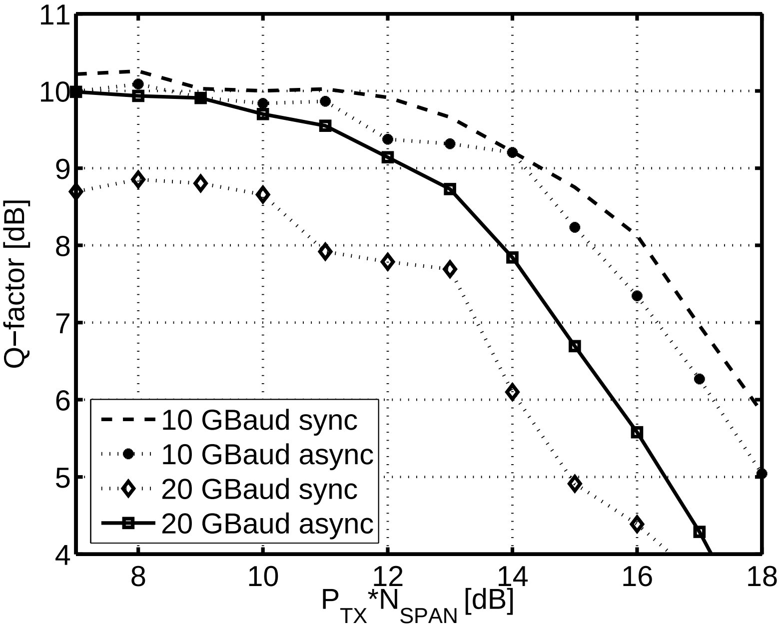

Figure 4.13: Results from 7 channels propagation without nonlinear phase noise simulation for 10 GBaud (dashed) and 20 GBaud (solid) systems.

4.3.3 WDM case: 7 channels

When there is more than one channel new possibilities arise. The bit pattern of each channel becomes an important parameter and is responsible for cross-channel effects. Moreover each laser source could have its own polarisation, initial phase and each bit pattern could be delayed with respect to the others. All these new aspects are translated into simulation random parameters. The results presented in this section are obtained considering that all the channels have the same polarisation, the laser sources have the same phase, while the bit patterns and the patterns delay are random parameters. It should be noted that the two most important cross-channel nonlinear effects are four-wave mixing (FWM) and cross-phase modulation (XPM). When the patterns are synchronous the first effect is increased and the second is decreased and viceversa when the patterns are asynchronous. It is interesting to see what happens by changing this synchronism between bits. In Fig. 4.13 there are

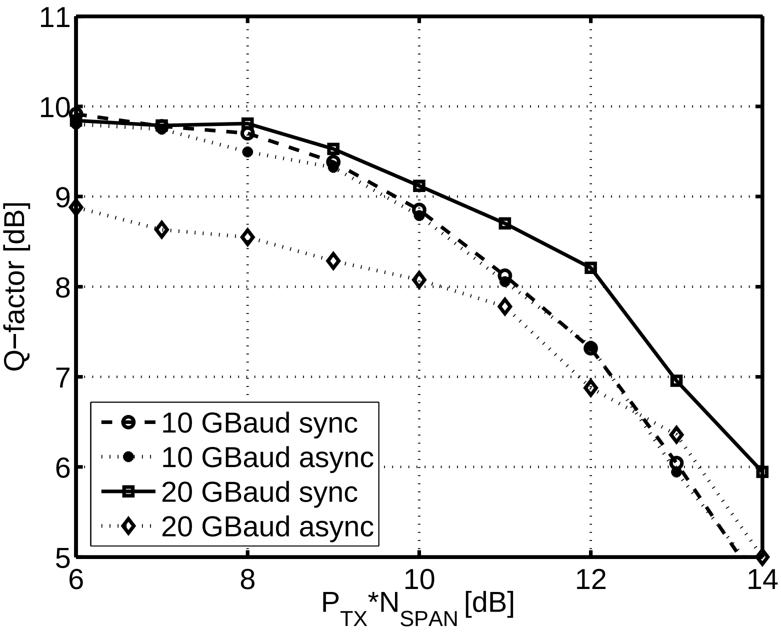

Figure 4.14: Results from 7 channels propagation with nonlinear phase noise simulation for 10 GBaud (dashed) and 20 GBaud (solid) systems.

four curves of Q-factor versus cumulated power: 10 GBaud system and 20 GBaud system both with synchronous and asynchronous patterns without NLPN. In the simulation at 10 GBaud without nonlinear phase noise (NLPN) the results show that the synchronous system works better and reaches a maximum gain over the asynchronous system of 0.5 dB of Q-factor. This is not a very big difference, especially if it is compared to the one of the 20 GBaud system. In that case the difference is around 1 dB. The 20 GBaud system is much more sensitive to the synchronicity so we can conclude that it is limited by XPM. In Fig. 4.14 the same system has been simulated, this time with NLPN. The results are not very different from the previous simulation. This time the 10 GBaud system is completely insensitive to pattern synchronism while the 20 GBaud system presents the same behaviour. From these results one can state that the XPM is an important impairment for this particular telecommunication system but the most impacting nonlinear effect is NLPN.

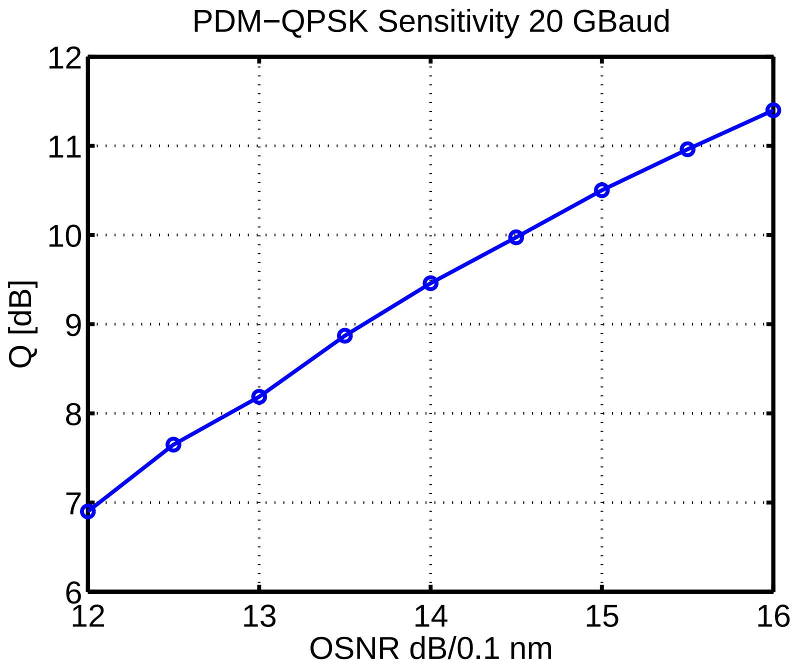

Figure 4.15: Results from sensitivity simulation for 20 GBaud (solid) systems with polarisation multiplexing.

4.3.4 Polarisation Division Multiplexing

Polarisation Division Multiplexing (PDM) requires a receiver capable of polarisation tracking. It can be impossible with a traditional receiver but it becomes easily exploitable when the employed detector is the coherent detector with digital signal processing. With the addition of the second polarisation the memory usage of the simulator doubles. This aspect could force the reduction of the number of samples or the number of bit when the simulator is already saturating the RAM memory of a PC. The transmitter does not changes, but it doubles. It is still an ideal one whit the two polarisation perfectly orthogonal. The propagation of a signal along a fibre becomes more complicated when polarisation effects are taken into account. This complication is not due to the PDM itself but it applies also in the single polarisation cases when polarisation mode dispersion (PMD) is taken into account. Obviously, with a PDM modulation format it is mandatory to consider both polarisation in the propagation equation. The transmission is calculated with cross-polarisation nonlinear effects. The receiver is now a polarisation diversity receiver so there are four photocurrents instead of two. The digital signal processing algorithm is the same except that it works in parallel on the two polarisation. The algorithm at the receiver should include a block that operates the polarisation demultiplexing stage: polarisation demultiplexing, polarisation tracking and PMD compensation. This particular block is based on a matrix of four adaptive filters. For this reason this is the most time consuming operation in the digital part of the receiver. This block could be skipped if the polarisation state of the signals is artificially set to the correct one when they reach the receiver.

In Fig. 4.15 there is the sensitivity curve calculated for the 20 GBaud PDM-QPSK (80 Gbit/s) system. This time the polarisation demultiplexing block was let turned on but, as already mentioned, the simulation time grows by a factor of 2 with respect to the case with ideal state of polarisation.

4.4 Conclusions

In this first investigation about the impact of fibre nonlinear effects on the coherent detection we verified that the impact of nonlinear phase noise on the performance is important. In particular, PDM-QPSK at 40 GBit/s present a pronounced sensitivity to nonlinear phase noise. This is an important aspect that should not be ignored when thinking about coherent detection as a possible upgrade for present 10 GBit/s OOK systems. Moreover, it should be noted that the examined case does not constitute at all a worst case. In fact, OOK channels present strong power variations that are missing in QPSK channels. For sure, the worst case can be a system full with 80 OOK channels (all the C band) where a single central channel is upgraded to PDM-QPSK with coherent detection. This example means only that the experimental work of this chapter does not claim to be a detailed investigation of nonlinear effects on the coherent detector. It should be seen as the beginning of a vast research subject that needs to be explored. The infinite capabilities of digital signal processing should suggest that there will not be impossible problems. But maybe we may face problems that may require unaffordable numerical computations.

Bibliography

[1] T. Durhuus, B. Mikkelsen, C. Joergensen, S. L. Danielsen, and K. E. Stubkjaer, “All-optical wavelength conversion by semiconductor optical amplifiers,” *IEEE J. Lightwave Technology*, vol. 14, pp. 942–954, 1996.

[2] D. Marcenac and A. Mecozzi, “Switches and frequency converters based on cross-gain modulation in semiconductor laser amplifiers,” *IEEE Photonics Technology Letters*, vol. 9, pp. 749–751, 1997.

[3] F. Öhman, S. Bishoff, B. Tromborg, and J. Mørk, “Noise and regeneration in semiconductor waveguides with saturable gain and absorption,” *IEEE J. Quantum Electron.*, vol. 40, pp. 245–255, 2004.

[4] M. Zhao, G. Morthier, and R. Baets, “Analysis and optimization of intensity noise reduction in spectrum-sliced WDM systems using a saturated semiconductor optical amplifier,” *IEEE Photonics Technology Letters*, vol. 14, pp. 390–392, 2002.

[5] M. Menif, W. Mathlouthi, P. Lemieux, L. A. Rusch, and M. Roy, “Error-free transmission for incoherent broadband optical communications systems using incoherent-to-coherent wavelength conversion,” *IEEE J. Lightwave Technology*, vol. 23, pp. 287–294, 2005.

[6] A. Uskov, J. Mørk, and J. Mark, “Theory of short-pulse gain saturation in semiconductor laser amplifiers,” *IEEE Photonics Technology Letters*, vol. 4, pp. 443–446, 1992.

[7] A. Mecozzi, S. Scotti, A. D’Ottavi, E. Iannone, and P. Spano, “Four-wave mixing in traveling-wave semiconductor amplifiers,” *IEEE J. Quantum Electron.*, vol. 31, pp. 689–699, 1995.

[8] D. Marcuse, “Computer model of an injection laser amplifier,” *IEEE J. Quantum Electron.*, vol. 19, pp. 63–73, 1983.

[9] M. J. Connelly, “Wideband semiconductor optical amplifier steady-state numerical model,” *IEEE J. Quantum Electron.*, vol. 37, pp. 439–447, 2001.

[10] K. Obermann, S. Kindt, D. Breuer, and K. Petermann, “Performance analysis of wavelength converters based on cross-gain modulation in semiconductor optical amplifiers,” *IEEE J. Lightwave Technology*, vol. 16, pp. 78–85, 1998.

[11] G. P. Agrawal and N. A. Olsson, “Self-phase modulation and spectral broadening of optical pulses in semiconductor laser amplifiers,” *IEEE J. Quantum Electron.*, vol. 25, no. 11, pp. 2297–2306, 1989.

[12] C. Tai and W. I. Way, “Dynamic range and switching speed limitations of an $n \times n$ optical packet switch based on low-gain semiconductor optical amplifiers,” *IEEE J. Lightwave Technology*, vol. 14, pp. 962–967, 1992.

[13] T. Liu, K. Obermann, K. Petermann, F. Girardin, and G. Guekos, “Effect of saturation caused by amplified spontaneous emission on semiconductor optical amplifier performance,” *Electron. Lett.*, vol. 33, pp. 2042–2043, 1997.

[14] G. Talli and M. J. Adams, “Gain dynamics of semiconductor optical amplifiers and three-wavelength devices,” *IEEE J. Quantum Electron.*, vol. 39, pp. 1305–1313, 2003.

[15] A. A. M. Saleh, “Nonlinear models of travelling wave optical amplifiers,” *IEE Electron. Lett.*, vol. 24, pp. 835–837, 1988.

[16] A. A. M. Saleh and I. M. I. Habbab, “Effects of semiconductor optical amplifier nonlinearity on the performance of high-speed intensity-modulation lightwave systems,” *IEEE Trans. Commun.*, vol. 38, pp. 839–846, 1990.

[17] M. M. Freire and H. J. A. Da Silva, “Performance implications of partial chirp compensation in a semiconductor optical booster amplifier for dispersion supported transmission at 10 Gb/s,” in *Proc. ICT ’98*, vol. 1, 1998, pp. 76–80.

[18] M. Settembre, F. Matera, V. Hägele, I. Gabitov, A. W. Mattheus, and S. K. Turitsyn, “Cascaded optical communication systems with in-line semiconductor optical amplifier,” *IEEE J. Lightwave Technology*, vol. 15, pp. 962–967, 1997.

[19] A. Bononi and L. A. Rush, “Doped-fiber amplifier dynamics: a system perspective,” *IEEE J. Lightwave Technology*, vol. 16, no. 5, Maggio 1998.

[20] Y. Sun, J. L. Zyskind, and A. K. Srivastava, “Average inversion level, modeling, and physics of erbium-doped fiber amplifiers,” *IEEE J. Sel Topics Quantum Electron.*, vol. 3, pp. 991–1007, 1997.

[21] S. Novak and A. Moesle, “Simulink model for EDFA dynamics applied to gain modulation,” *IEEE J. Lightwave Technology*, vol. 20, pp. 986–992, 2002.

[22] A. Bononi, M. Papararo, and M. Fuochi, “Transient gain dynamics in saturated Raman amplifiers,” *Optical Fiber Technol.*, vol. 10, pp. 91–123, 2004.

[23] T. Durhuus, B. Mikkelsen, and K. E. Stubkjaer, “Detailed dynamic model for semiconductor optical amplifiers and their crosstalk and intermodulation distortion,” *IEEE J. Lightwave Technology*, vol. 10, pp. 1056–1065, 1992.

[24] W. Mathlouthi, P. Lemieux, M. Salsi, A. Vannucci, A. Bononi, and L. A. Rusch, “Fast and efficient dynamic WDM semiconductor optical amplifier model,” *IEEE J. Lightwave Technology*, vol. 24, no. 11, pp. 4353–4365, 2006.

[25] G. P. Agrawal and I. M. I. Habbab, “Effect of four-wave mixing on multichannel amplification in semiconductor laser amplifiers,” *IEEE J. Quantum Electron.*, vol. 26, no. 3, pp. 501–505, 1990.

[26] D. J. Blumenthal and N. C. Kothari, “Coherent crosstalk in multichannel FSK/DD lightwave systems due to four-wave mixing in semiconductor optical amplifiers,” *IEEE Photonics Technology Letters*, vol. 8, no. 1, pp. 133–135, 1996.

[27] A. Uskov, J. Mørk, and J. Mark, “Wave mixing in semiconductor laser amplifiers due to carrier heating and spectral-hole burning,” *IEEE J. Quantum Electron.*, vol. 30, no. 8, pp. 1769–1781, 1994.

[28] J. Zhou, N. Park, J. W. Dawson, K. J. Vahala, M. A. Newkirk, and I. Miller, Barry, “Efficiency of broadband four-wave mixing wavelength conversion using semiconductor traveling-wave amplifiers,” *IEEE Photonics Technology Letters*, vol. 6, no. 1, pp. 50–52, 1994.

[29] G. Bellotti, “Interazione tra dispersione cromatica e nonlinearità di Kerr nelle trasmissioni ottiche WDM,” Ph.D. dissertation, Università degli studi di Parma, Nov. 2000.

[30] R. S. Luís and A. V. T. Cartaxo, “Analytical characterization of SPM impact on XPM-induced degradation in dispersion-compensated WDM systems,” *IEEE J. Lightwave Technology*, vol. 23, no. 3, pp. 1503–1513, March 2005.

[31] M. Zirngibl, “Gain control in erbium-doped fibre amplifiers by an all-optical feedback loop,” *Electronic Letters*, vol. 27, pp. 560–561, 1991.

[32] P. Doussiere, A. Jourdan, G. Soulage, P. Garabedian, C. Graver, T. Fillion, E. Derouin, and D. Leclerc, “Clamped gain travelling wave semiconductor optical amplifier for wavelength division multiplexing applications,” in *Semiconductor Laser Conference, 14th IEEE International*, 19-23 September 1994, pp. 185–186.

[33] D. Wolfson, S. L. Danielsen, C. Joergensen, B. Mikkelsen, and K. E. Stubkjaer, “Detailed theoretical investigation of the input power dynamic range for gain-clamped semiconductor optical amplifier gates at 10 Gb/s,” *IEEE Photonics Technology Letters*, vol. 10, no. 9, pp. 1241–1243, Settembre 1998.

[34] K. V. Shrikhande, I. M. White, D. Wonglumsom, S. M. Gemelos, M. S. Rogge, Y. Fukashiro, M. Avenarius, and L. G. Kazovsky, “HORNET: a packet-over-WDM multiple access metropolitan area ring network,” *IEEE Journal on Selected Areas in Comunications*, vol. 18, no. 10, pp. 2004–2016, Ottobre 2000.

[35] A. Bianciotto, V. de Feo, R. Gaudino, A. la Porta, F. Neri, and M. Petracca, “Experimentation of single-hop WDM rings for metro and distributed switching applications,” in *Photonics in Switching, PS ’06. International Conference on*, 16-18 October 2006, pp. 1–4.

[36] D. Francis, S. DiJaili, and J. Walker, “A single chip Linear Optical Amplifier,” in *Proceedings Optical Fiber Communication Conference (OFC)*, March 2001, paper PD13.

[37] E. Tangdiongga, J. J. J. Crijns, L. H. Spiekman, G. N. van den Hoven, and H. de Waardt, “Performance analysis of linear optical amplifiers,” *IEEE Photonics Technology Letters*, vol. 14, no. 8, 2002.

[38] J. J. J. Crijns, L. H. Spiekman, G. van den Hoven, E. Tangdiongga, and H. de Waardt, “Static and dynamic switching performance of a metro WDM ring using linear optical amplifiers,” *IEEE Photonics Technology Letters*, vol. 14, no. 10, 2002.

[39] J. Oksanen and J. Tulkki, “On crosstalk an noise in an optical amplifier with gain clamping by vertical laser field,” *IEEE J. Lightwave Technology*, vol. 21, no. 9, 2003.

[40] C.-Y. Jin, Y.-Z. Huang, L.-J. Yu, and S.-l. Deng, “Detailed model and investigation of gain saturation and carrier spatial hole burning for a semiconductor, optical amplifier with gain clamping by a vertical laser field,” *IEEE J. Quantum Electron.*, vol. 40, no. 5, 2004.

[41] “Linear Optical Amplifier (LOA) datasheet,” Finisar - www.finisar.com.

[42] L. Becouarn, G. Vareille, P. Pecci, and J. F. Marcerou, “3 Tbit/s transmission (301 DPSK channels at 10.709 Gb/s) over 10 × 270 km with a record efficiency of 0.65 bit/s/Hz,” in *Proc. ECOC 03*, Rimini, Italy, 2003, p. Postdeadline paper Th4.3.2.

[43] J.-X. Cai, D. G. Foursa, C. R. Davidson, Y. Cai, G. Domagala, H. Li, L. Liu, W. W. Patterson, A. N. Pilipetskii, M. Nissov, and N. S. Bergano, “A DWDM demonstration of 3.73 Tb/s over 11000 km using 373 RZ-DPSK channels at 10 Gb/s,” in *Proc. OFC 03*, Atlanta, GA, USA, 2003, p. Postdeadline paper PD22.

[44] A. H. Gnauck, G. Raybon, S. Chandrasekhar, J. Leuthold, C. Doerr, L. Stulz, A. Agarwal, S. Banerjee, D. Grosz, S. Hunsche, A. Kung, A. Marhelyuk, D. Maywar, M. Movassaghi, X. Liu, C. Xu, X. Wei, and D. M. Gill, “2.5 Tb/s (64×42.7 Gb/s) transmission over 40×100 km NZDSF using RZ-DPSK format and all-Raman-amplified spans,” in *Proc. OFC 02*, Anheim, CA, 2002, p. Postdeadline paper FC2.

[45] G. Charlet, S. Lanne, L. Pierre, C. Simonneau, P. Tran, H. Mardoyan, P. Brindel, M. Gorlier, J. C. Antona, M. Molina, P. Sillard, J. Godin, W. Idler, and S. Bigo, "Cost-optimized 6.3 Tb/s-capacity terrestrial link over 17 ×100 km using phase-shaped binary transmission in a conventional all-EDFA SMF-based systems," in *Proc. OFC 03*, Atlanta, GA, 2003, p. Postdeadline Paper PDP25.

[46] A. H. Gnauck, P. J. Winzer, S. Chandrasekhar, and C. Dorrer, "Spectrally efficient (0.8 b/s/Hz) 1-Tb/s (25×42.7 Gb/s) RZ-DQPSK transmission over 28×100-km SSMF spans with 7 optical add/drops," in *Proc. ECOC 04*, vol. 6, Stockholm, Sweden, 2004, pp. 40–41, paper Th4.4.1.

[47] G. Charlet, P. Tran, H. Mardoyan, M. Lefrancois, T. Fauconnier, F. Jorge, and S. Bigo, "151×43 Gb/s transmission over 4080 km based on return-to-zero differential quadrature phase-shift keying," in *Proc. ECOC 05*, vol. 6, Glasgow, Scotland, 2005, pp. 5–6.

[48] G. Raybon, S. Chandrasekhar, A. Agarwal, A. H. Gnauck, L. L. Buhl, J. Sinsky, and A. Adamiecki, "Limitations of optical add/drop filtering on 42.7-Gb/s transmission with 50-GHz channel spacing," in *Proc. ECOC 04*, vol. 1, Stockholm, Sweden, 2004, pp. 94–95.

[49] J. A. Lázaro, W. Idler, R. Dischler, and A. Kleinkamp, "Filtering and linear crosstalk penalties of ASK and DPSK 43 Gb/s DWDM systems with 50 GHz channel spacing," in *Proc. ECOC 04*, vol. 3, Stockholm, Sweden, 2004, pp. 416–417.

[50] S. J. Savory, A. D. Stewart, S. Wood, G. Gavioli, M. G. Taylor, R. I. Killey, and P. Bayvel, "Digital equalization of 40 Gbit/s perwavelength transmission over 2×480 km of standard fibre without optical dispersion compensation," in *Proc ECOC 06*, Cannes, France, 2006, p. Paper Th2.5.5.

[51] G. Charlet, J. Renaudier, M. Salsi, H. Mardoyan, P. Tran, and S. Bigo, "Efficient mitigation of fiber impairments in an ultra-long haul transmission of 40 Gbit/s polarization-multiplexed data by digital processing in a coherent receiver," in *Proc. OFC 07*, Anaheim, CA, 2007, p. Postdeadline Paper PDP17.

[52] C. R. S. Fludger, T. Duthel, D. van den Borne, C. Schulien, E.-D. Schmidt, T. Wuth, E. de Man, G. D. Khoe, and H. de Waardt, “10×111 Gb/s, 50 GHz spaced, polmux-RZ-DQPSK transmission over 2375km employing coherent equalization,” in *Proc. OFC 07*, Anaheim, CA, 2007, p. Postdeadline Paper PDP22.

[53] C. Laperle, B. Villeneuve, Z. Zhang, D. McGhan, H. Sun, and M. O’Sullivan, “Wavelength division multiplexing and polarization mode dispersion performance of a coherent 40 Gb/s dual-polarization quadrature phase shift keying transceiver,” in *Proc. OFC 07*, Anaheim, CA, 2007, p. Postdeadline Paper PDP16.

[54] L. E. Nelson, T. N. Nielsen, and H. Kogelnik, “Observation of PMDinduced coherent crosstalk in polarization-multiplexed transmission,” *IEEE Photonics Technology Letters*, vol. 13, no. 7, pp. 738–740, 2001.

[55] D.-S. Ly-Gagnon, S. Tsukamoto, K. Katoh, and K. Kikuchi, “Coherent detection of optical quadrature phase shift keying signals with carrier phase estimation,” *IEEE J. Lightwave Technology*, vol. 24, no. 1, pp. 12–21, 2006.

[56] C. R. S. Fludger, T. Duthel, T. Wuth, and C. Schulien, “Uncompensated transmission of 86 Gbit/s polarization multiplexed RZ-QPSK over 100km of NDSF employing coherent equalization,” in *Proc. ECOC 06*, Cannes, France, 2006, p. Paper Th4.3.3.

[57] S. Tsukamoto, K. Katoh, and K. Kikuchi, “Unrepeated 20 Gbit/s QPSK transmission over 200-km standard single mode fiber using homodyne detection and digital signal processing for dispersion compensation,” in *Proc. OFC 06*, Anaheim, CA, 2006, p. Paper OWB4.

[58] P. Serena, M. Bertolini, M. Salsi, and N. Rossi, *Optilux: a SSFM based optical simulator*, Dipartimento di Ingegneria dell’Informazione, Dec. 2007, internal Software.

[59] E. Forestieri, “Evaluating the error probability in lightwave systems withchromatic dispersion, arbitrary pulse shape and pre- and postdetection filtering,” *IEEE J. Lightwave Technology*, vol. 18, no. 11, pp. 1493–1503, 2000.

[60] D. N. Godard, “Self-recovering equalization and carrier tracking in two-dimensional data communication systems,” *IEEE Trans. Inf. Theory*, vol. COM-28, no. 11, pp. 1867–1875, 1980.

[61] K. Kikuchi, M. Fukase, and K. Sang-Yuep, “Electronic post-compensation for nonlinear phase noise in a 1000-km 20-Gbit/s optical QPSK transmission system using the homodyne receiver with digital signal processing,” in *Optical Fiber Communication and the National Fiber Optic Engineers Conference 2007. OFC/NFOEC 2007*, Anaheim, CA, 25-29 March 2007.

[62] A. Viterbi and A. J. Viterbi, “Nonlinear estimation of PSK-modulated carrier phase with application to burst digital transmission,” *IEEE Trans. Infor. Theory*, vol. 29, pp. 543–551, 1983.

[63] K. Roberts, “Electronic dispersion compensation beyond 10 Gb/s,” in *Proc. LEOS Summer Top. Meet. 2007*, 2007, p. Invited paper MA2.3.

[64] S. Tsukamoto, Y. Ishikawa, and K. Kikuchi, “Optical homodyne receiver comprising phase and polarization diversities with digital signal processing,” in *Proc. ECOC 06*, Cannes, France, 2006, p. Paper Mo 4.2.1.

[65] L. Yan, X. S. Yao, M. C. Hauer, and A. E. Willner, “Practical solutions to polarization-mode-dispersion emulation and compensation,” *IEEE J. Lightwave Technology*, vol. 24, no. 11, pp. 3992–4005, 2006.

[66] H. Kogelnik, R. M. Jopson, and L. E. Nelson, *Optical Fiber Telecommunications IVB*, I. P. Kaminow and T. Li, Eds. San Diego, CA: Academic Press, 2002.

[67] G. Charlet, N. Maaref, J. Renaudier, H. Mardoyan, P. Tran, and S. Bigo, “Transmission of 40 Gb/s QPSK with coherent detection over ultra-long-haul distance improved by non linear mitigation,” in *Proc. ECOC 06*, Cannes, France, 2006, p. Paper Th 4.3.4.

[68] A. Papoulis, *Probability, Random Variables, and Stochastic Processes*, third edition ed. McGraw-Hill, Inc., 1991.

[69] E. Ip and J. Kahn, “Feedforward carrier recovery for coherent optical communications,” *IEEE J. Lightwave Technology*, vol. 25, no. 9, pp. 2675–2692, September 2007.

Publications

This is the list of publications produced during this Ph.D. thesis.

M. Salsi, A. Vannucci, and A. Bononi, “Misure su amplificatori ottici lineari per la rete ottica metropolitana a pacchetto WONDER,” in *Fotonica 2005*, Trani, BA, Italy, 2005.

A. Vannucci, M. Salsi, A. Bononi, A. La Porta, A. Bianciotto, and R. Gaudino, “Theroetical and experimental investigation of low-cost optical amplification for packet-switched WDM metro networks,” in *Network and Optical Comunications Conference*, London, UK, 2005.

W. Mathlouthi, P. Lemieux, M. Salsi, A. Vannucci, A. Bononi, and L. A. Rusch, “Fast and efficient dynamic WDM semiconductor optical amplifier model,” *IEEE J. Lightwave Technology*, vol. 24, no. 11, pp. 4353–4365, 2006.

——, “A novel model for SOAs in WDM networks,” in *Lasers and Electro-Optics Society, IEEE*, Montreal, Quèbec, Oct. 2006, pp. 150–151.

M. Salsi, A. Vannucci, A. Bononi, W. Mathlouthi, P. Lemieux, and L. A. Rusch, “A reservoir dynamic model for linear optical amplifiers,” in *Lasers and Electro-Optics Society, IEEE*, Montreal, Quèbec, Oct. 2006, pp. 215–216.

M. Magnani, M. Salsi, M. Bertolini, and A. Bononi, “Misure comparative di prestazione di catene di amplificatori a semiconduttore con e senza stabilizzazione del guadagno,” in *Fotonica*, Mantova, Italy, 2007.

G. Charlet, J. Renaudier, M. Salsi, H. Mardoyan, P. Tran, and S. Bigo,

"Efficient mitigation of fiber impairments in an ultra-long haul transmission of 40Gbit/s polarization-multiplexed data, by digital processing in a coherent receiver," in *Optical Fiber Communication Conference and Exposition and The National Fiber Optic Engineers Conference.* Anaheim, CA: Optical Society of America, 2007, p. PDP17.

J. Renaudier, G. Charlet, P. Tran, M. Salsi, and S. Bigo, "A performance comparison of differential and coherent detections over ultra long haul transmission of 10Gb/s BPSK," in *Optical Fiber Communication Conference and Exposition and The National Fiber Optic Engineers Conference.* Anaheim, CA: Optical Society of America, 2007, p. OWM1.

M. Salsi, J. Renaudier, G. Charlet, O. Bertran Pardo, P. Tran, and S. Bigo, "Investigation of single channel nonlinear impairments on 40Gb/s coherent polarization division multiplexed QPSK in dispersion managed or digitally post compensated systems," in *ECOC Conference*, Berlin, Germany, Sept. 2007.

G. Charlet, J. Renaudier, M. Salsi, O. Bertran Pardo, H. Mardoyan, and S. Bigo, "Performance comparison of singly-polarized and polarisation-multiplexed coherent transmission at 10Gbauds under linear impairments," in *ECOC Conference*, Berlin, Germany, Sept. 2007.

G. Charlet, M. Salsi, J. Renaudier, O. Bertran Pardo, H. Mardoyan, and S. Bigo, "Performance comparison of singly-polarised and polarisation-multiplexed coherent transmission at 10Gbauds under linear impairments," *Electronics Letters*, vol. 43, no. 20, pp. 1109–1111, Sept. 2007.